CRITICALITY AND SAMPLING IN NEURAL NETWORKS

JOÃO PINHEIRO NETO

Göttingen Graduate School for Neurosciences, Biophysics, and Molecular Biosciences
Faculty of Physics
University of Göttingen

November 2020

THESIS COMMITTEE:
Dr. Viola Priesemann (Thesis supervisor)
Prof. Dr. Fred Wolf
Prof. Dr. Marion Silies
Prof. Dr. Reiner Kree

LOCATION:
Göttingen, Germany

Criticality and sampling in neural networks

Dissertation
for the award of the degree
“Doctor of Philosophy”
Division of Mathematics and Natural Sciences
of the Georg-August-Universität Göttingen

within the doctoral program
Göttingen Graduate Center for Neurosciences, Biophysics, and Molecular Biosciences
of the Georg-August University School of Science (GAUSS)

submitted by
João Pinheiro Neto

from Curitiba, Brazil
Göttingen, 2020

Thesis Committee

Dr. Viola Priesemann, Neural Systems Theory, Max Planck Institute for Dynamics and Self-Organization

Prof. Dr. Fred Wolf, Theorectical Neurophysics, Max Planck Institute for Dynamics und Self-Organization

Prof. Dr. Marion Silies, Institute of Developmental Biology and Neurobiology, Johannes Gutenberg University

Prof. Dr. Reiner Kree, Institute for Theoretical Physics, Georg August University Göttingen

Members of the Examination Board

Referee: Dr. Viola Priesemann, Neural Systems Theory, Max Planck Institute for Dynamics and Self-Organization

2nd Referee: Prof. Dr. Reiner Kree, Institute for Theoretical Physics, Georg August University Göttingen

Further members of the Examination Board

Prof. Dr. Fred Wolf, Theoretical Neurophysics, Max Planck Institute for Dynamics und Self-Organization

Prof. Dr. Marion Silies, Institute of Developmental Biology and Neurobiology, Johannes Gutenberg University

Prof. Dr. Peter Sollich, Institute for Theoretical Physics, Georg-August-Universität Göttingen

Prof. Dr. Theo Geisel, Dept. of Nonlinear Dynamics, Max Planck Institute for Dynamics and Self-Organization

Prof. Dr. Michael Wibral, Department of Data-driven Analysis of Biological Networks , Georg-August-Universität Göttingen

Date of oral examination: 14/01/2021

ABSTRACT

The brain is made of billions of functional units that interact and give raise to its collective properties. The criticality hypothesis states that many these properties emerge due to brain dynamics operating at the critical point of a phase transition. In models, the critical point maximizes potentially useful properties such as sensitivity, temporal integration, and correlation length. The hypothesis remains controversial, however, in part due to sampling effects: only a small fraction of the neurons in the brain can be recorded, leading to bias in the observed collective properties.

In this Thesis we analyze how sampling effects can bias the assessment of criticality in neural networks. We explore sampling effects both in models with critical dynamics and in experimental results, and find a number of mechanisms that can result in bias. Chiefly, we develop a model of neuronal avalanches where activity is sampled in different levels (spikes and coarse signals), and show that coarse signals cannot differentiate between close to critical and very subcritical states. This unifies contradictory results in the literature, and argue in favor of a subcritical, reverberating state for dynamics in vivo. We also show that sampling can alter the spectra of neuronal activity, and thus explain its variability. Applying this mechanism to data, we find that flatter spectra observed in in vitro recordings suggest poorer sampling in that condition. Lastly, we also perform a literature review on the evidence of criticality in the brain. The picture that emerges is that evidence is largely ambiguous, mostly due to sampling effects. Nevertheless, a few key results offer strong evidence that criticality can emerge in neural networks. Coupled with the prospect of considerably improved experimental techniques in the near future, we argue that critical phenomena may become increasingly useful in the understanding of brain activity.

PUBLICATIONS

Some ideas and figures have appeared previously in the following publications:

[1] F. P. Spitzner et al. “MR. Estimator, a toolbox to determine intrinsic timescales from subsampled spiking activity.” In: (July 2020). arXiv: `2007.03367`.

[2] Jonas Dehning et al. “Inferring change points in the spread of COVID-19 reveals the effectiveness of interventions.” In: *Science (80-.)*. 15 (May 2020), eabb9789. ISSN: 0036-8075. DOI: `10.1126/science.abb9789`. arXiv: `2004.01105`.

[3] Joao Pinheiro Neto et al. “A unified picture of neuronal avalanches arises from the understanding of sampling effects.” In: (Oct. 2019), pp. 33–35. DOI: `10.1101/759613`. arXiv: `1910.09984`.

[4] Jens Wilting et al. “Operating in a Reverberating Regime Enables Rapid Tuning of Network States to Task Requirements.” In: *Front. Syst. Neurosci.* 12.November (Nov. 2018). ISSN: 1662-5137. DOI: `10.3389/fnsys.2018.00055`.

[5] Joao Pinheiro Neto et al. “Inhibition as a determinant of activity and criticality in dynamical networks.” In: *arXiv* 2.2 (2017), pp. 1–10. arXiv: `1712.08816v1`.

ACKNOWLEDGMENTS

I thank Dr. Viola Priesemann for supervising my PhD. I'm very grateful for all she taught me about the art of doing science. The academic rigor she built into me is something I'll carry for the rest of my career.

I thank my colleagues and friends at the Max Planck Institute for Dynamics and Self-Organization (MPI-DS) for all those years of lively and interesting discussions on topics that ranged from brain dynamics to epidemiology and climate change. I thank the colleagues who I worked directly with, in particular Paul Spitzner, Hauke Bluhm, Jens Wilting and Dr. Johannes Zierenberg (who also helped with proofreading). I thank the secretaries at the MPI-DS, in particular Barbara Kutz, for helping so much in the administrative part. I also thank Dr. Theo Geisel for first accepting me into the MPI-DS. I thank my thesis committee members. I thank the Brazilian National Council for Scientific and Technological Development (under Grant No. 206891/2014-8) and the Max Planck Society for financial support.

I thank my friends and family from Brazil, now spread all over the world, for their help and friendship. I also thank all the friends I've made in my life in Germany. They all have made my life much richer.

Finally, I thank my parents, for everything.

CONTENTS

LIST OF FIGURES

LIST OF TABLES

1

INTRODUCTION

> *"The first principle is that you must not fool yourself — and you are the easiest person to fool."* - Richard Feynman

The brain is said to be the most complex machine in the known universe. It is an organ made of billions of functional units (the neurons), which controls all aspects of motor function. It is also capable of processing, recording, and learning from new information. The mammoth task of understanding how the brain works is the object of study of Neuroscience.

The study of the brain is interdisciplinary, done by different fields at different scales. At the lowest scales, Biochemistry works to unveil the mechanisms behind the molecular machinery that supports brain function. At the other end of the scale, Psychology and Medicine try to link neuronal activity of the brain as whole to cognition and behavior.

Somewhere in the middle, concepts from Physics have increasingly been applied to understand brain dynamics. One focus is on collective behavior at large ($> 10^3$ neurons) scales: how do neurons propagate information? How is this information integrated at the various scales of neuronal activity? Can simple models and a few key mechanisms be useful in understanding it?

For around two decades[1], it has been argued that brain activity operates in a critical state, poised between functionally different phases. This is called the **criticality hypothesis**, and states that by being at this particular dynamic state the brain can benefit from the maximization of many functional properties [1, 3–6]. The hypothesis is controversial, however, with some of its signature observables shown to be obtainable with non-critical (such as subcritical) models [7–9]. Nevertheless, criticality remains an important framework to understand how the brain can propagate and process information.

An issue that arises when trying to assess criticality in biological systems is **sampling**. In principle, experimentally studying collective phenomena (such as criticality) requires recording the entire system in question. Any less, and measurements can be subject to *sampling bias*, which can lead to an incorrect assessment of the dynamic state of the system. As the mammalian brain is made of millions to billions of neurons [10], such complete recordings are currently impossible.

Current electrophysiological techniques impose heavy restrictions on both (i) fraction of the system that is sampled, and (ii) sampling scheme used. While state-of-the-art methods can record activity of up to $\sim 10^4$ neurons under spe-

---

[1] Initial experimental evidence on criticality in neuronal systems dates from the early 2000's [1], while theoretical arguments have been made as early as 1994 [2].

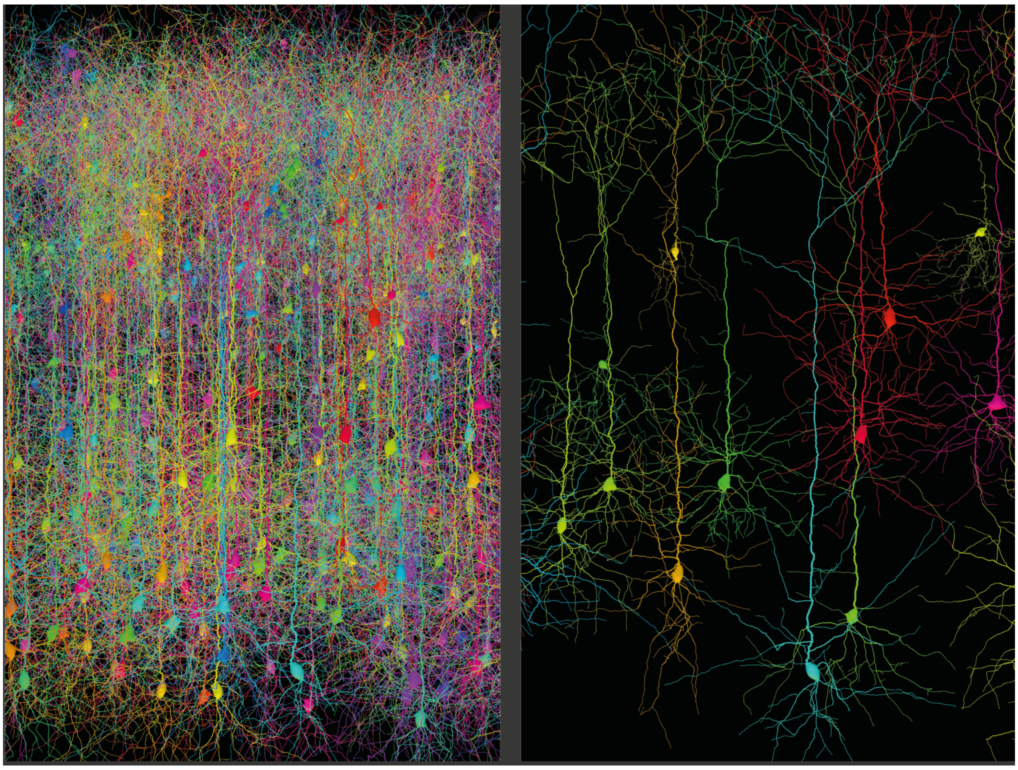

Figure 1.1: **Subsampling of neuronal activity.** While the brain is made of billions of neurons (left) we can only measure the activity of at most a few thousand neurons (right). This sampling effect constrain our understanding of collective behavior in the brain, and can bias the assessment of its dynamics. Visualization created with the TREES toolbox [11].

cific settings, it still represents an extremely small fraction ($< 0.01\%$) of the neurons in the mammalian brain. In Fig. 1.1 we show a representation of neuronal subsampling. Moreover, neuronal networks are extremely heterogeneous both in function and topology [185]. Thus, when analyzing neuronal activity, great care is necessary both regarding the accuracy of the measured properties, and how they generalize to different areas from the ones observed.

In this Thesis we explore how sampling effects can bias the assessment of the dynamic state of neuronal networks. We start by introducing important background information in Chapter 2, which includes extensive reviews of the experimental results on criticality (Sec. 2.5), and the fundamental model used to study it (Sec. 2.4). In Chapter 3 we explore sampling bias in different systems, showing how it can bias their observables. In particular, in Sec. 3.3 we demonstrate how sampling bias can explain the variability in neuronal spectra observed in different experiments. In Chapter 4 we develop a model where neural activity is sampled in two different ways, and show that this unifies contradictory results in the literature regarding criticality in the brain. Lastly, in Chapter 5 we offer a discussion and outlook on the importance of sampling for future research of criticality in Neuroscience.

2

CRITICALITY IN PHYSICS AND NEUROSCIENCE

In this chapter we introduce the fundamentals to understand the relationship between critical phenomena in Physics and Neuroscience. We first introduce in Sec.2.1 the concept of criticality, and in Sec. 2.2 which functional properties are associated with the critical state. We then summarize in Sec. 2.3 important concepts regarding criticality from the point of view of statistical physics. We describe in detail the branching process in Sec. 2.4, which is widely used to model criticality in Neuroscience. Lastly, in Sec. 2.5 we review the literature of criticality in the context of neuronal avalanches, summarizing key papers and ideas that formed our current understanding in the field.

2.1 WHAT IS CRITICALITY?

Many systems in nature have different phases, for instance the states of matter. As certain system parameters change (e.g. temperature), the system undergoes a *phase transition*, identified by changes in its properties. Criticality refers to the state of a system poised at this precise *critical point* that separates the two (or more) phases [12, 13].

Different systems may have phases of different nature. For instance, a dynamical system may have a phase with ordered dynamics and another with chaotic dynamics, with an ”edge of chaos” critical state separating them. In another system, the phase transition may be between an absorbing state (where dynamics dies out) and an active state (where it is self-sustaining).

Phase transitions can also be *continuous* or *abrupt*. In a continuous (also called “second order”) phase transition, the quantity measured (e.g. level of synchronization or activity) varies smoothly. In an abrupt (or “first order”) phase transition it changes in a discontinuous manner from one phase to the other.

As an experimental example of a continuous phase transition, let us consider ferromagnetic materials. Below a critical temperature T_c (called the Curie point) these materials have innate magnetism (ferromagnetism), which disappears for $T > T_c$ (paramagnetism). This transition is continuous, since the magnetization M of the magnet goes smoothly to zero as $T \to T_c$. It is also an example of a order-disorder[1] transition: for low temperatures, the magnetic spins in the material are aligned (order) and thus there is a net magnetization. For high temperatures the spins are not aligned and thus there is no resulting magnetization. See Fig. 2.1A for an example of materials with different T_C.

---

[1] This phase transition is related to, but different from the stable-chaotic transition mentioned earlier. Here the system is in an equilibrium state, while the earlier transition is about how the dynamics evolve over time.

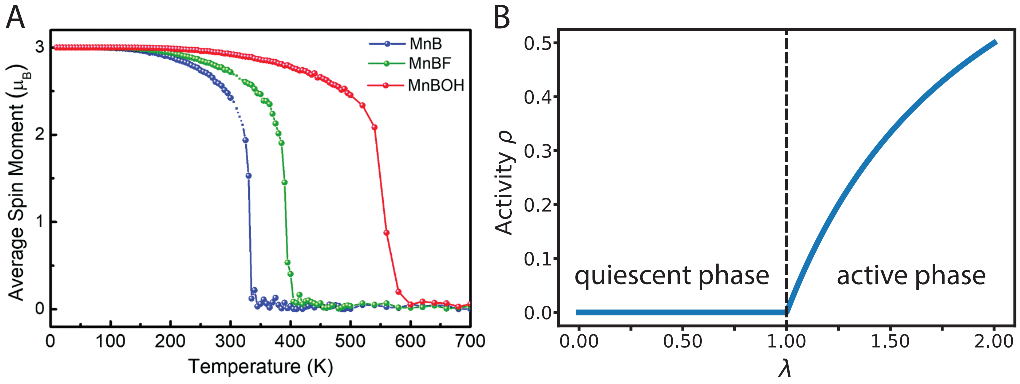

Figure 2.1: **Continuous phase transitions in experiments and models.** **A**. Ferromagnetic materials have different critical temperatures T_C at which magnetization vanishes. Adapted from [16]. **B**. Quiescent and active phases of a contact process, with a critical point $\lambda = 1$.

As a representative system, consider the contact process (CP) model [5, 14]. In this process, active units become quiescent at rate μ, and they can also activate quiescent ones at rate λ. Assuming homogeneous interaction between units (*well-mixed* dynamics) activity is created at a rate $\lambda\rho(1-\rho)$, and disappears at a rate $\mu\rho$. If we set $\mu = 1$ for simplicity, the evolution of the fraction of active nodes $\rho(t)$ is then given by:

$$\dot{\rho}(t) = \lambda\rho(t)\left[1-\rho(t)\right] - \rho(t) \tag{2.1}$$

Eq. 2.1 has a critical (bifurcation) point at $\lambda_c = 1$: since $\rho \in [0,1]$, if $\lambda < 1$ then $\dot{\rho} < 0$, and activity will always decay. If $\lambda > 1$ it becomes possible to have stable, non-zero activity. Solving Eq. 2.1 for $\dot{\rho} = 0$ we find that this stable fraction of active nodes is given by $\rho\,(t \to \infty) = 1 - 1/\lambda$. In Fig. 2.1B we show the resulting phase diagram for the CP model.

The CP model is useful in modeling initial epidemic spreading, where it is known as the susceptible-infected-susceptible (SIS) model. From Eq.2.1 we can derive how fast a disease spreads during an outbreak: for small ρ we have $\dot{\rho} \approx (\lambda - 1)\,\rho$ and thus $\rho(t) \sim e^{(\lambda-1)t}$. In other words, being supercritical ($\lambda > 1$) results in spreading that is initially exponential. This is observed in real-world epidemics, such as the recent COVID-19 pandemic [15].

Besides separating phases, the critical point is usually associated with many interesting properties. For instance, for the magnetic materials described above, T_C is the point of maximum magnetic susceptibility, i.e. how much the material responds to an external magnetic field. The same happens for the CP model: at $\lambda_c = 1$ the response to an external perturbation is maximal. In Sec. 2.2 we go in detail into the properties maximized at criticality.

The study of critical phenomena in Physics, especially of continuous transitions, is vast. Important models include the Ising model, used to explain the magnetization phase transition of Fig. 2.1A, and the directed percolation (DP) class of models (which include the CP model), used to describe activity spreading. Following pioneering work by Kadanoff and others in the 1960's [17, 18], many useful concepts where developed. These include universality, scaling, and the renormalization group (RG) transform, and extensions such as self-organized criticality (SOC). In Sec. 2.3 we explore these concepts and models in more detail.

2.2 FUNCTIONAL PROPERTIES OF CRITICALITY

2.2.1 *Correlation length*

Much of the interest in studying critical phenomena, in particular in the context of neuronal dynamics, comes from the *observables* associated with a critical state. These are quantities (such as the magnetization M in Fig. 2.1A) that are particularly important in describing the state of the system. In particular, critical phenomena is associated with long-range spatiotemporal interactions [12]. This manifests in the form of a diverging correlation length in the infinite-size limit, and maximal correlation for finite systems.

Correlation functions offer an alternative view into what is criticality. A diverging correlation function means that there is no particular scale to interactions: units are correlated over infinite time and/or space, even if they are directly connected to only a few other units. This happens because, while the strength of interactions between two units decay with distance, the multitude of paths connecting those units increases. The point where these two effects balance each other results in maximum correlation, and it is the critical point. Thus, an alternative way to look for criticality is to search for parameter values that maximize correlation functions.

Long spatiotemporal correlations are important in the context of neuronal activity, as they imply coordinated behavior between the neurons. Let us consider spatial and temporal correlations separately: Long spatial correlations are necessary to coordinate millions of neurons across large brain areas. They can be quantified by measuring for instance pairwise spike correlations between neurons [19]. Long temporal correlations, on the other hand, are necessary to maintain long-lasting memories in the spiking dynamics. They can be quantified by measuring the *autocorrelation function* (ACF) of neuronal populations.

The ACF of a *stationary process*[2] is the cross-correlation between the process and itself at different time lags. For a discrete timeseries $A(t)$ starting at $t = 1$, the ACF $C(t)$ can be estimated from

$$C(t) = \frac{1}{(n-t)\sigma^2} \sum_{t_0=1}^{n-t} (A(t_0) - \mu)(A(t_0 + t) - \mu) \tag{2.2}$$

where $\mu = n^{-1} \sum_t A(t)$ is the mean, $\sigma^2 = n^{-1} \sum_t (A(t) - \mu)^2$ is the variance and n is the length of the timeseries. It follows that $C(t) \in [-1, 1]$, and $C(0) = 1$. In some systems, such as the branching process with drive described in Sec. 2.4, the ACF has an exponential form:

$$C(t) \sim e^{-t/\tau} \tag{2.3}$$

in that case, the parameter τ is known as the **autocorrelation time**, or intrinsic timescale, of the dynamics.

2.2.2 *Avalanche dynamics*

In many systems with critical dynamics, activity propagates in well-defined bursts, inter-spaced by periods of silence. This property is known as *separation of timescales*, and the spatiotemporal clusters of activity are called *avalanches*. The analysis of avalanche dynamics is concerned mainly with two properties: **(i)** the **avalanche size** S, which is the number of system units activated, and **(ii)** the **avalanche duration** D, which is the total time duration of the avalanche. An important signature of criticality is that the probability distributions of S and D follow power-laws:

$$p(S) \sim S^{-\alpha} \tag{2.4}$$

$$p(D) \sim D^{-\beta} \tag{2.5}$$

where $\alpha, \beta > 0$ are known as the **critical exponents** of the dynamics. Another observable of avalanche dynamics is the **average avalanche size** $\langle S \rangle (D)$ for avalanches of a given duration D. At criticality, it also follows a power-law:

$$\langle S \rangle \sim D^{\gamma} \tag{2.6}$$

with $\gamma > 0$. The exponents α, β and γ are called critical exponents, and follow a scaling law:

$$\frac{\beta - 1}{\alpha - 1} = \gamma \tag{2.7}$$

---

[2] A stationary process is one where the probability distribution is time-independent. Stationarity is a requirements for most time-series analyses, and care must be taken when dealing with non-stationary processes.

They are signature of the *universality class* of the dynamics – the category of models it belongs to (see Sec. 2.3.1 for more details). Moreover, the average *temporal profile* at criticality follows a universal scaling function $\mathscr{F}$. For a given avalanche duration D, the average activity $s(t,T)$ at any time t within the avalanche is given by:

$$s(t,D) \sim D^{\gamma-1}\mathscr{F}(t/D) \tag{2.8}$$

Thus, rescaling $s(t,D) \to s(t,D)/D^{\gamma-1}$ and $t \to t/D$ results in a data collapse of avalanches of all durations.

The interest in the fact that $p(S)$ and $p(D)$ follow power-laws is that they are heavy-tailed probability distributions and are *scale-free*: there is no characteristic scale to the distribution (contrasting to e.g. Eq. 2.3), and rescaling the variable $x \to cx$ produces no change. The power-law is the only function with this property.

In the context of brain dynamics, heavy-tailed distributions (which also include e.g. lognormal distributions) are linked to a number of functional properties. For instance, response to sensory stimuli depend logarithmically on the amplitude of the signal [20]. More importantly, power-law avalanche distributions describe a particular mode of activity: most avalanches of activity are very small, but eventually very large avalanches can happen and dramatically affect the system.

It is important to note that power-laws are not unique and obligatory signatures of criticality. On one hand, it has been shown that apparent power-laws can emerge from non-critical dynamics. For instance, a sum of exponential distributions with properly-selected parameters can look like a power-law [3, 7, 21]. On the other hand, sampling bias can make power-law distributions from critical systems appear non-power-law [22]. This is explored in detail in Chapter 4.

The focus on the avalanche probability distributions leads to an important technical challenge: fitting power-law distributions to empirical data. Identification and fitting of power-law distributions depends crucially on the distribution's tail, which has orders of magnitude less samples than the beginning. Considerable efforts have been made in the development of methods to validate power-law fits of data [23–25]. In particular, it has been shown that applying log to $f(x) = x^{\alpha}$ and linearly-fitting $\log f(x) = \alpha \log x$ is unreliable [26]. The accepted standard for fitting power-laws is to use maximum-likelihood estimator (MLE) methods, and use Kolmogorov-Smirnov statistics for validation [23]. Furthermore, an often used rule of thumb is that distributions should span at least 2 orders of magnitude to be candidates for power-law fitting [27].

Despite the technical difficulties, the observation of power-laws remain an important indicative that the system in question has dynamics with long spatiotemporal correlations.

2.2.3 *Dynamic range and dynamical repertoire*

In many models, criticality also maximizes other properties besides correlation length, some of which are considered very useful for the transmission and processing of neuronal activity. It maximizes the *dynamic range*, which is the range of input magnitude to which a system responds with discernible response [28, 29]. Many functional regions of the brain need to respond to stimuli with a wide range of intensities, making a maximal dynamic range a desirable property[3].

Criticality also maximizes measures of the variability of spatiotemporal patterns in networks, also called the *dynamical repertoire*. These include maximizing the number of metastable states in branching networks [30], and the number of dynamical attractors in Boolean [31] and integrate-and-fire networks [32]. Experimentally, analysis of resting state networks found them to be poised at criticality, modeled with both with simple threshold-based [33] and complex integrate-and-fire dynamics [34].

2.2.4 *Complexity and computational properties*

Criticality has long been conjectured to be important in the context of computation [35, 36]. In particular, the critical point between ordered and chaotic dynamics (edge of chaos) has been shown to provide maximal computational power[4]. This was observed first in cellular automata models [36, 37], and subsequently in logistic maps [38] and recurrent neuronal networks [39–41].

Information-theoretic measures [42, 43] also point towards criticality offering maximal information transmission capabilities. Mutual information was observed to be maximized at criticality in Boolean networks [44], threshold networks [39], and branching networks [3]. The same was observed for transfer entropy in the Ising model [45], and recurrent [46] and Boolean [47] networks.

As we can see, the appeal of criticality comes not from a single model or property, but from the observation that it maximizes many properties in many different models. This has triggered a heated debate about the generality of the concept of criticality, particularly in the context of computation [38, 48, 49][5].

In the context of neuronal activity, the main question is whether these properties associated with critical dynamics are observed in recordings of neuronal activity. Before delving into it, we first explore in more detail the concept of criticality, and then define the branching process, widely used to study critical phenomena in neuroscience.

---

[3] These include the auditory, visual and olfactory systems.

[4] Like ”criticality”, ”computation” can be a loaded term. Here it means the act of transforming an input into an output, following some algorithm. Computational power refers to the number of such transformations a system can perform.

[5] This debate is maybe best-exemplified by Per Bak’s 1996 book about self-organized criticality, titled ”How Nature Works” [50].

2.3 CRITICALITY IN STATISTICAL MECHANICS

2.3.1 *Key concepts*

In the context of continuous phase transitions, the critical state is defined as the state where a system undergoes a *phase transition*, measured by a chosen *order parameter*, with respect to some *control parameter*. In other words, in order to rigorously define a critical state, we must specify: i) a system, ii) some quantity that encapsulates the collective behavior of the system (the order parameter) and iii) some variable x that can cause this behavior to abruptly change (the control parameter). The value $x = x_c$ at which this abrupt change occurs is called the **critical point**. Comprehensive texts on statistical mechanics with an emphasis on critical phenomena include [13, 51, 52].

Precise definition of criticality requires careful study of the system in question. In particular, there is no established method to find an appropriate order parameter of a critical system, and even for simple systems such definition can be tricky [13, 53]. Nevertheless, it was observed that many models share similarities, especially around the critical point. This resulted in one of the biggest appeals of critical phenomena: *universality*. This is the notion that, near the critical point, the collective behavior is largely independent of details, and all models within the same **universality class** have the same behavior. Intuitively, the concept is that as the system moves towards the critical point, most *degrees of freedom* associated with model details vanish, and only the ones that identify the universality class remain. Thus, it underlies a certain hierarchy of mechanisms, with some (the ones defining the universality class) being more important than others (the ones that only matter away from criticality).

Mathematically, the universality class is identified by the *critical exponents* of the model [17]. These are exponents of various quantities (*observables*) that scale as power-laws around the critical point. In other words, if χ is such an observable[6], and γ_χ is its respective critical exponent, then as the control parameter $x \to x_c$ we find that χ scales as

$$\chi \sim |x - x_c|^{-\gamma_\chi} \tag{2.9}$$

Moreover, the critical exponents respect a set of equalities — known as *scaling laws* — that tie them together (such as Eq. 2.7).

The last key concept in critical phenomena is that of the **renormalization group** (RG), also known as *coarse-graining* [12, 13, 51]. Numerically, it offers a recipe to obtain critical exponents. More importantly, renormalization deals with how the dynamics of a system is observed at different scales. It describes a number of techniques that maps a system to a version of itself with microscopic degrees of freedom removed, effectively shrinking it. For instance, the block spin renormalization [54, 55] aggregates units into "super units", remov-

---

[6] Such as mean cluster size in directed percolation, or magnetic susceptibility in the Ising model.

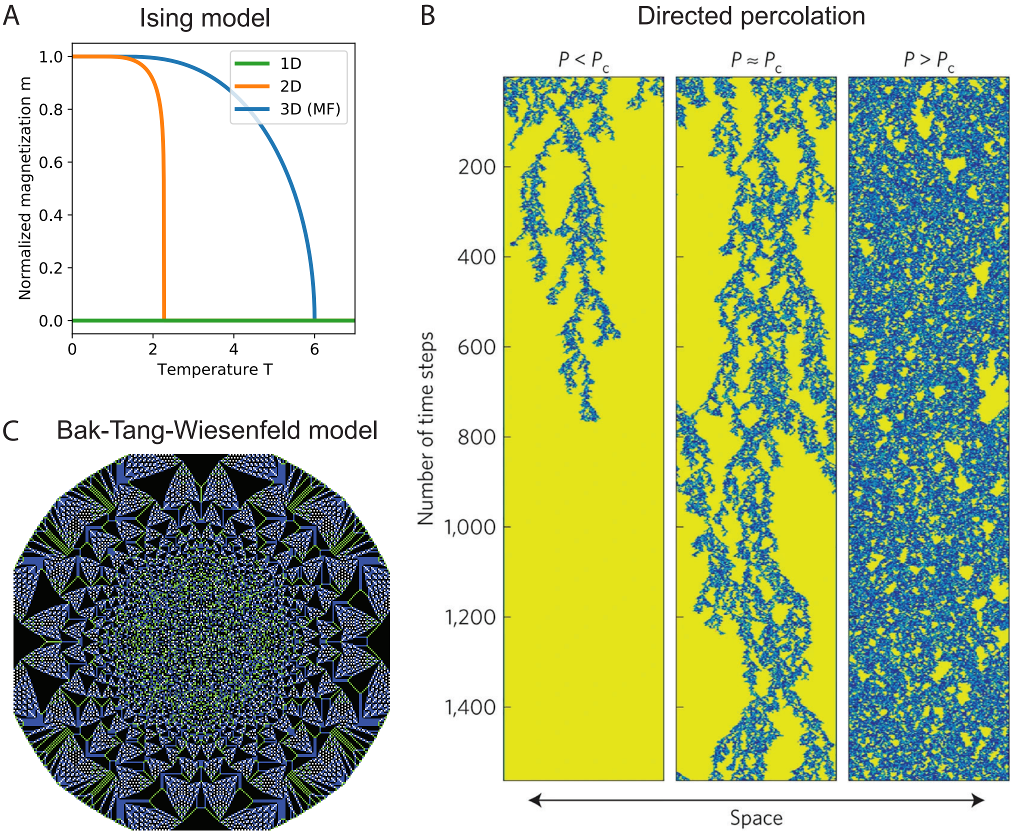

Figure 2.2: **Models with critical dynamics. A:** Spontaneous magnetization $m(T)$ of the Ising model with one to three dimensions (using $k_B = J = 1$) in the thermodynamic limit. The blue curve (3D) corresponds to the mean-field (MF) solution (Eq. 2.12). **B:** Time evolution of the 1D directed (bond) percolation, with probability P of a bond existing and critical point P_c. Reproduced with permission from [56]. **C:** Visualization of the Bak-Tang-Wiesenfeld model on a 256 × 256 grid after dropping 128M sand grains in the center. Colors correspond to number of grains: white is 0, green is 1, blue is 2 and black is 3. Figure generated with the Interpile toolbox [57].

ing the interactions between them and reducing system size. Through this procedure, observables of the system are changed. The exception is if the dynamics is self-similar, and the observables have the same structure in all scales (known as *scale-invariance*). This happens only at the critical point. Thus, only at criticality coarse-graining produces invariant observables.

In order to make those concepts more clear, models must be introduced. In Sec. 2.3.2 we describe a number of classic models of critical phenomena, and in Sec. 3.2 we explain the coarse-graining of the Ising model. There, we show the type of bias that can emerge if coarse-graining is done incorrectly.

2.3.2 *Models with critical dynamics*

The phenomena of criticality has been explored in a wide variety of models in Physics. Besides being divided into abrupt (first-order) and continuous (second-order) transitions, another important categorical distinction is between *equilibrium* and *non-equilibrium* dynamics [14, 58].

In an equilibrium phase transition the system is fully described by a time-independent ensemble statistics: probabilities of each configuration of states occurring are fixed, and the system may be critical depending on a tunable order parameter (such as temperature). Even so, a dynamic model (such as Glauber dynamics [59] for the Ising model) is sometimes used to generate the ensemble statistics.

In systems with non-equilibrium phase transitions, however, the ensemble of states evolves with time. More than that, time is treated as a degree of freedom, in equal footing with spatial dimensions[7]. Besides being more realistic for a wide number of applications, non-equilibrium systems can have more complex dynamics and different types of phase transitions, due to their extra degree of freedom.

One important type of non-equilibrium universality class is of systems with absorbing states. Once the system reaches this state (for instance, all units being quiescent) it cannot leave. Thus, it defines a phase transition between an active and a frozen state. The most prominent universality class with an absorbing transition is the Directed Percolation (DP) class, which incorporates both the directed percolation model and other models explored in this Thesis.

In the following we describe a number of classic equilibrium and non-equilibrium models. Each illustrates an important concept: the Ising model exemplifies the role of dimensionality in critical phenomena, and its coarse-graining is well understood. Directed percolation is the most established example of a non-equilibrium phase transition. Boolean networks exemplify the role of topology by having a phase transition defined by topological (network) properties. Finally, the Bak-Tang-Wiesenfeld model helps introduce the concept of self-organized criticality.

2.3.2.1 *Ising model*

The Ising model is one of the most classic models in Physics. It describes the collective behavior of interacting magnetic spins with two discrete orientations $s_i = \pm 1$, and has been applied to problems ranging from neuroscience to the stock market to disease spreading [60–62]. In its simplest form[8], it is given by the Hamiltonian $H(\vec{s}) = \sum_{\langle i,j \rangle} s_i s_j$, where $\langle i, j \rangle$ denotes all pairs of nearest neigh-

---

[7] A system with N spatial dimensions is then said to be a 'N+1' system.

[8] The full Hamiltonian of the Ising model includes a coupling constant J. For simplicity, here we set $J = 1$.

boring spins. The probability of observing the ensemble $\vec{s}$ is given by the Boltzmann distribution

$$P(\vec{s},T) = \frac{1}{Z_T} e^{-H(\vec{s})/k_B T} \tag{2.10}$$

where T is the temperature of the system, k_B is the Boltzmann constant (here, $k_\mathrm{B} = 1$) and Z_T is the partition function that normalizes the distribution. The mean normalized magnetization $m(T) = \frac{1}{N}|\sum_i s_i|$ describes the collective magnetization of the system: if $m(T) > 0$ then spins have a preferential orientation, and the system has innate (ferro)magnetism.

The behavior of the Ising model depends both on T and the topology of the system. The one-dimensional Ising model was first solved by Ernest Ising, who has shown that magnetism requires the application of an external magnetic field. In other words, the 1D Ising model has $m = 0$ and no phase transition.

The two-dimensional Ising model consists of spins arranged on a square lattice[9]. Its analytical solution is considerably more sophisticated, and was first shown (famously without proof) by Onsager [63]. As the temperature T reaches the critical temperature $T_c = 2/\ln(1+\sqrt{2})$, the system undergoes a continuous (second-order) phase transition between a disordered spin configuration ($T > T_c$) and an ordered state of aligned spin orientations ($T < T_c$). Many observables diverge at $T = T_c$ in the thermodynamic limit ($L \to \infty$), such as correlation length, specific heat and susceptibility [13, 55]. The magnetization of the 2D Ising model is given by:

$$m_{2D}(T) = \left(1 - \sinh^{-4}(2/T)\right)^{1/8} \tag{2.11}$$

For 3+ dimensions no analytical solution is known. Instead, understanding of the system comes from simulations and from the mean field solution of the model. The mean-field solution shows that the system has a phase transition at temperature $T_c = q$, where q is the number of neighbors of a spin (e.g. $q = 4$ for the 2D square lattice and known as the *coordination number*). While the mean-field solution is incorrect for the 1D case and off for the 2D case ($T_c = 1/\ln(1+\sqrt{2}) \approx 2.3$ instead of 4), it becomes increasingly accurate as the dimensionality increases. The mean-field spontaneous magnetization m_{MF} of the Ising model for $T < T_c$ is given implicitly by

$$T = \frac{2qm_{MF}}{\log\left(\frac{1+m_{MF}}{1-m_{MF}}\right)} \tag{2.12}$$

In Fig. 2.2A we compare the (analytic) magnetization of the Ising model in the 1D and 2D cases with the mean-field solution for the 3D case ($q = 6$). As we can see, behavior is considerably different: both critical temperature and shape

---

[9] The solutions for the 1D and 2D Ising model are taken in the thermodynamic (infinite size) limit. Finite systems are subject to finite-size effects and display different solutions.

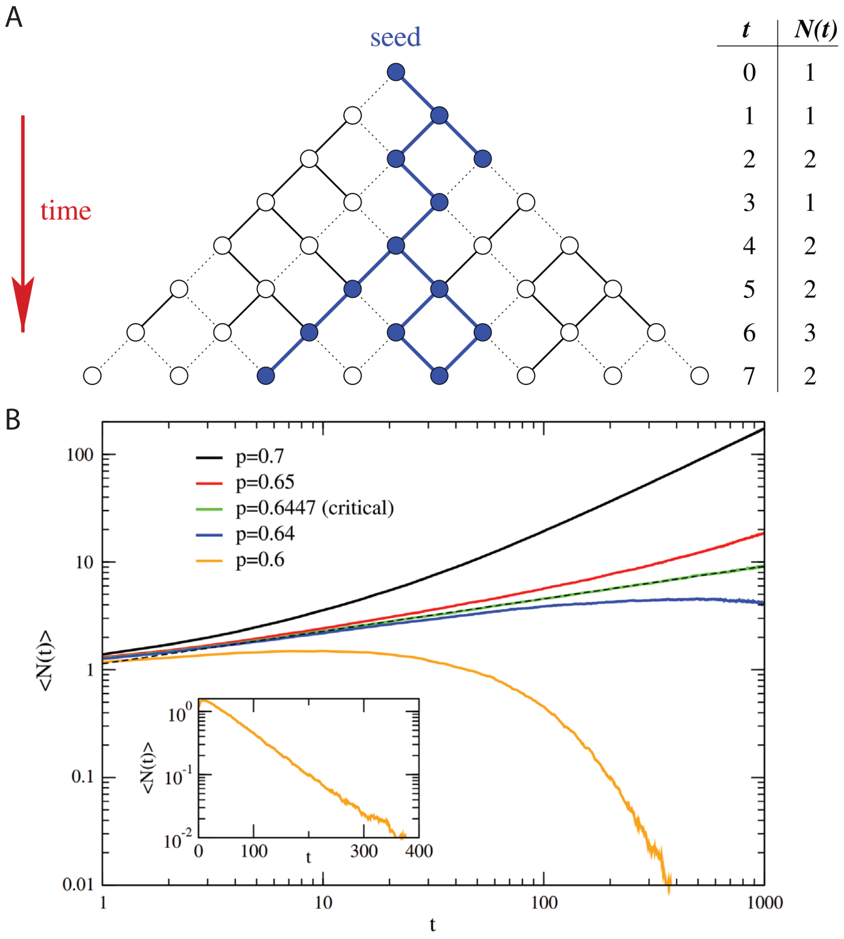

Figure 2.3: **Directed Percolation. A.** Representation of the directed bond percolation process on a 2D diagonal lattice, with time t and number of active sites $N(t)$. **B.** Average number of active sites $\langle N(t)\rangle$ as a function of the percolation probability P with activity started in a single site. For $P < P_c \approx 0.6447$ we find that $\langle N(t)\rangle$ decreases exponentially. For $P = P_c$ it increases as a power-law $\langle N(t)\rangle \sim t^{\theta}$ with $\theta \approx 0.308$ (sublinear, traced line). For $P > P_c$ it increases superlinearly. Reproduced with permission from [58].

of $m(T)$ depend on dimensionality. Thus, we conclude that changing the spatial embedding can result not only in numerical changes (since $T_c = q$ depends on the number of dimensions) but dramatic changes as well — such as creating a phase transition for 2+ dimensions.

2.3.2.2 *Directed percolation*

The Directed Percolation (DP) universality class encompasses many non-equilibrium models with absorbing phase transitions. In particular, both the contact process (CP) mentioned in Sec. 2.1 and the branching process (described in detail in Sec.

2.4) are members of this class. Fundamentally, the DP models how activity can spread — *percolate* — between units in a given topology [58]. As such, models of this class are widely used to describe spreading processes from disease spreading in populations to activity spreading in the brain[10].

In its simplest realization[11], directed percolation is made of sites placed on a 2D diagonal lattice of size $N \times L$ with directed links from top to bottom (see Fig. 2.3A for a graphic representation). Links between sites may exist independently with probability P. The question is: *how likely that a path exists from top to bottom, as a function of* P*?* This model can also be interpreted in a dynamical way as a 1D array of N sites that at each timestep (row of the lattice) may activate its 2 nearest neighbors independently with probability P. In this case, the question becomes: how likely that activity survives after L timesteps, as a function of P?

It turns out there is a phase transition involved. At a critical *percolation threshold* P_c the probability of the system reaching this absorbing state quickly changes from 0 to 1: if $P < P_c$, activity will very likely not percolate to the end, while $P > P_c$ almost guarantees that it does, for any finite L. See Fig. 2.2B for a visualization of the percolation process for long durations, and Fig. 2.3B for a plot of the evolution of the number of average active sites $\langle N(t) \rangle$. For $P < P_c$ we observe that $\langle N(t) \rangle$ decreases exponentially, while for $P > P_c$ it increases superlinearly. For $P = P_c$ we find that $\langle N(t) \rangle$ increases, but following a power-law $\langle N(t) \rangle \sim t^{\theta}$ with $\theta \approx 0.308$. Thus, activity increases slowly.

Interestingly, the numerical value of P_c is not universal, and depends on lattice structure and dimensionality. For the diagonal lattice exemplified it is given by $P_c \approx 0.6447$. A triangular lattice has the same dimensionality $(1+1)$, but one extra neighbor (coordination number $q = 3$ instead of $q = 2$). This results in a smaller percolation threshold $P_c \approx 0.4780$ [66]. A simple cubic lattice, on the other hand, has the number of neighbors $(q = 3)$ as the triangular lattice but higher dimensionality $(2 + 1)$. This results in a lower percolation threshold $P_c \approx 0.3822$ [67]. This is tied to the long-range correlations that emerge at criticality: due to them, higher-order features of the topology become important, and impact the phase transition.

2.3.2.3 *Boolean and Threshold Networks*

Boolean Networks are networks whose node's activity depends on a Boolean function of the input. For instance, a node may be active if the sum of its inputs is even, and inactive if it is odd. Nodes only transmit binary signals between each other, and the dynamics is deterministic.

---

[10] Interestingly, while directed percolation has been studied for many decades [64], experimental evidence for systems displaying precisely the directed percolation critical behavior is much more recent [65].

[11] DP models can be categorized into *bond* percolation and *site* percolation, depending whether the dynamics happens between the units (sites) or between their bonds. Here we focus on bond percolation.

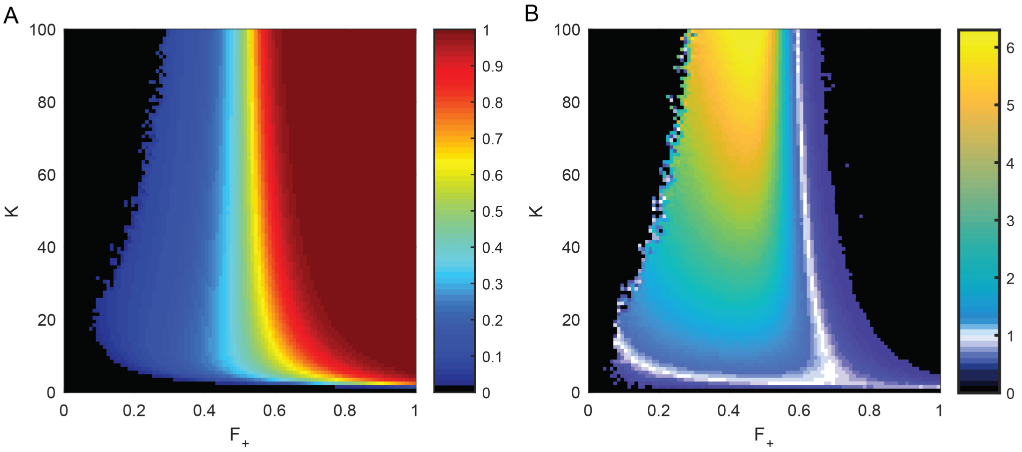

Figure 2.4: **Random Threshold Network with inhibition. A.** Parameter space for the normalized average activity A of RTNs with degree K and fraction of positive links F_+. **B.** Same for the sensitivity to perturbation, given by the Hamming distance H. The white lines corresponds to critical dynamics ($H = 1$). Reproduced from [77].

In a *Random Boolean Network* (RBN) the function is chosen at random from a set of Boolean functions, and connected on a network with some underlying topology. RBN's are used to model a wide variety of systems, in particular genetic regulatory networks [68–71].

Since the signal transmitted in a RBN is binary, the parameters that can be tuned are related to the topology of the network. In its simplest form, an RBN is made of nodes each connected to K neighbors, and thus assigned a random Boolean function that takes K inputs. In this case $K_c = 2$ defines a phase transition between stable and chaotic dynamics. This transition is defined by the average effect of perturbing (changing the state) a single node in the network — the number of nodes that changed the state they would have due to the perturbation. This is encoded by the *Hamming distance* H between the perturbed and unperturbed states. If $H > 1$, perturbations grow geometrically, and the system is chaotic. If $H < 1$ they vanish quickly, and the system is stable. At $H = 1$ we have criticality.

While Boolean functions make sense in the context of gene regulation, many systems with simpler units are unlikely to perform such vast array of computations [12]. In particular, many systems (such as neurons) have threshold-based dynamics. In a *Random Threshold Network* (RTN) all nodes have a threshold function, and are activated if the sum of inputs is above a threshold h [72–74]. The function can be either a step function (outputs 0,1) or a sign function (outputs ± 1). At criticality, RTNs have interesting properties that can differ from RBNs [72, 75, 76].

---

[12] The number of Boolean functions of K variables is 2^{2^K}, and thus grows very quickly with K.

A number of variants of the RTN dynamics have been developed. Probabilistic dynamics was shown to generate ceaseless dynamics [78], asynchronous update of the node states changes attractor structure [79], and self-regulation (when the input is exactly at the threshold) can add long-term temporal correlations [72, 74]. Changing the topology by adding a community structure also enriches the dynamics [79, 80].

Inspired by inhibition in the brain, we've shown [77] that a varying balance between inhibition and excitation creates vertical and horizontal critical lines ($H = 1$), allowing criticality for $K > 2$. By varying both K and the fraction F_+ of links that are positive, we show that it is possible to tune both the level of activity in the network and sensitivity to perturbation. See Fig. 2.4 for the phase diagram of this model.

2.3.2.4 *Bak–Tang–Wiesenfeld model*

The Bak-Tang-Wiesenfeld model (BTW, also known as the Abelian sandpile model) is another very famous model with critical dynamics [81]. It is best-known as the model that introduced the concept of self-organized criticality. Its dynamics is inspired by the toppling of sand grains in a sandpile: each point of the sandpile balances a number of sand grains, and topples if the pile gets too tall. In its simplest version, units in the model are spread in a $N \times M$ lattice and each site at position (x, y) is associated with an (initially random) integer value $z(x, y) \in [0, 3]$. If during the dynamics $z(x, y) \geq 4$, the site "topples", losing 4 units and sending one to each of its neighbors. Mathematically, the dynamics is updated synchronously with

$$\begin{aligned} z(x,y) &\to z(x,y) - 4 \\ z(x \pm 1, y) &\to z(x \pm 1, y) + 1 \\ z(x, y \pm 1) &\to z(x, y \pm 1) + 1 \end{aligned} \tag{2.13}$$

for every site $z(x, y) > 3$. Dynamics starts by adding one unit to a random site, and updating it following Eq. 2.13 (i.e. letting the avalanche run) until no site has more than 3 units.

This unit-adding dynamics drives the system towards a critical distribution of units, with a number of sites at the edge of toppling ($z(x, y) = 3$). In Fig. 2.2C we show the distribution of a 256×256 system after toppling 128M units in the center of the grid[13]. Note the apparent self-similarity of the state, with rich patterns at various scales.

In this critical state, adding a single unit can result in large avalanches toppling sites throughout the entire system. The avalanche dynamics results in the power-laws described in Sec. 2.2.2, with an avalanche size distribution $p(S) \sim S^{-\alpha}$ and an avalanche duration distribution $p(D) \sim D^{-\beta}$. In the case of the BTW model,

---

[13] The BTW model in Fig. 2.2C is *open*, in the sense that units sent to outside the system are removed and do not accumulate at the borders.

these exponents are $\alpha = 1.293$ and $\beta = 3/2$ [82]. Thus, large avalanches are more common in the BTW model than in the branching process studied in Sec. 2.4.

2.3.3 *Extensions of criticality*

While criticality refers to specific values of the control parameter of a system with a second-order phase transition, the term became associated with other phenomena which doesn't necessarily fit into this definition. In this section we briefly go over two of its most interesting extensions: self-organized criticality and Griffiths phases.

2.3.3.1 *Self-organized Criticality*

As seen in Sec. 2.2, many properties are maximized/diverge at the critical point. However, this effect is not linear. For instance, in the branching model of Sec. 2.4 the observable τ (the autocorrelation time) is related to the control parameter m (the branching parameter) by $\tau \sim -1/\log m$. Thus, a small change around $m \approx 1$ produces a large resulting change in τ. In other worlds, for a system to be critical it requires fine parameter tuning.

The concept of **Self-Organized Criticality** (SOC) solves this issue by adding some topological or dynamical mechanism that leads the system towards this critical point without the need to fine-tune parameters [81, 84–87]. This is exemplified in Fig. 2.5A for an energy transition, with a critical energy E_c: if the system is subcritical, the mechanism needs to drive the system towards E_c. If the system is supercritical, the same mechanism needs to dissipate energy in order to bring it to criticality.

As mentioned previously, the Bak-Tang-Wiesenfeld model is the best-known example[14] of a system displaying SOC: in it, criticality is encoded in the distribution of units (sand grains) in the lattice. The toppling dynamics drives the system towards the critical distribution, from any random initial conditions and with no extra fine-tuning.

A number of properties (or ingredients) are commonly found in SOC systems, and have been associated with the concept. First, the state at which the system arrives at must be critical, displaying the properties explored throughout this chapter (e.g. power-law observables). The rule that drives the system towards criticality needs to be non-linear, in many cases employing some form of thresholding. SOC systems also have *separation of timescales*, with fast dynamics being driven by slow processes. In the BTW model, those properties are clearly seen: the toppling rule thresholds dynamics, and it generates fast avalanches of activity from slow integration of sand grains being added. The avalanches reflect

---

[14] In terms of displaying properties associated with SOC, the Manna model is considered a better example, however [86, 88].

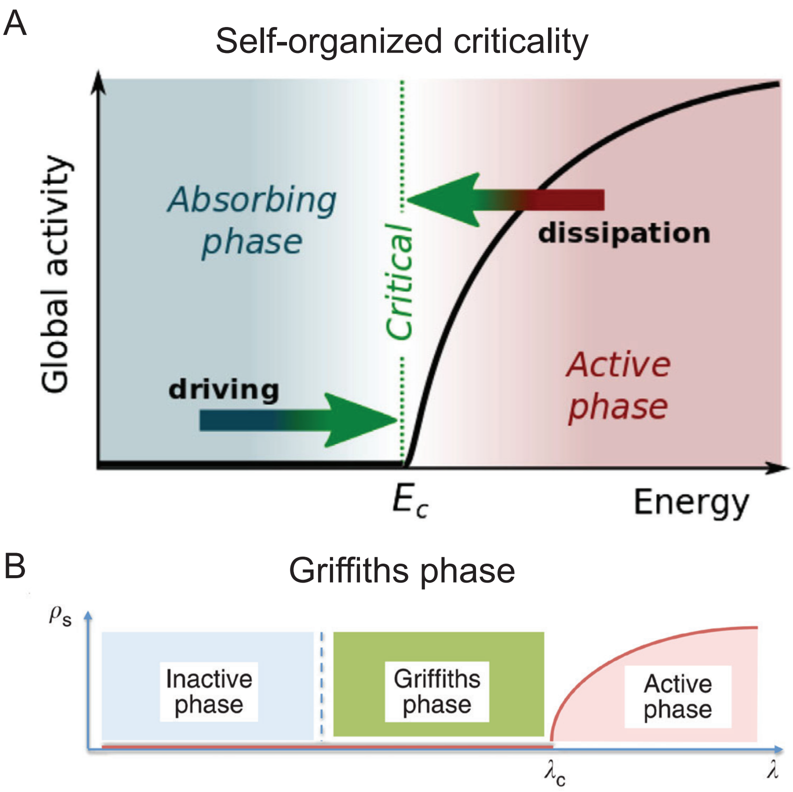

Figure 2.5: **Extensions of criticality. A.** Representation of self-organized criticality (SOC): a mechanism leads the system towards the critical energy E_c from both phases, either driving the subcritical system (adding energy) or dissipating energy of the supercritical one. Reproduced with permission from [5]. **B.** Representation of a Griffiths phase: an heterogeneous topology (quenched disorder) stretches the region with critical-like dynamics in the subcritical phase ($\lambda < \lambda_c$). Reproduced with permission from [83].

power-law spatiotemporal correlations and the critical exponents respect scaling laws — the final state is critical.

Many other models were adapted with mechanisms that appear to be SOC. In the context of percolation, coercing the number of active sites to be constant drives the system towards the percolation threshold [89]. Mechanisms have also been proposed that evolve the topologies of Random Boolean [90] and Random Threshold [91, 92] networks towards the critical degree K_c.

The concept of SOC is controversial in statistical mechanics [85, 86], in part due to the difficulty in rigorously defining what is and what is not SOC. Nevertheless, it found great appeal in many areas of science. In particular, earthquake size distribution is known to follow the Gutenberg-Richter law: the number of earthquakes N with size greater than $S = 10^m$ (where m is a given earthquake magnitude) in a region follows

$$N(s > S) \sim S^{-b} \tag{2.14}$$

with $b \approx 1$ for active regions [93]. At the same time, the Omori law states that, after an earthquake, the frequency of aftershocks decay with time T as

$$N(T) \sim T^{-\alpha} \tag{2.15}$$

with $\alpha \approx 1$. These are old, empirical relationships that are readily explained in a SOC framework: tectonic movement slowly adds energy to the plates (slow integration) that are released during an earthquake (fast release). Indeed, SOC is thought to be an important mechanism behind earthquake dynamics [85, 86]. The concept is also applied in financial systems, due to its nature of being composed of intelligent agents [62, 94].

In Neuroscience, it has frequently been argued that the brain presents SOC [95–98]. Synaptic plasticity (in its various forms) could drive the system towards a critical state or a point near to it, depending on task and brain region [96, 99–101]. In Sec. 2.5 we review the experimental evidence for criticality in the brain, and in Table 2.4 we summarize the evidence for SOC in developing cultures.

2.3.3.2 *Griffiths phase*

One pattern observed in the models of Sec. 2.3.2 is the influence of topology on the dynamics: the Ising phase transition depends on dimensionality, where the percolation threshold of directed percolation depends on the exact structure of the system. Another type of topological effect than can happen is the presence of microscopic, structural heterogeneities in the topology [15]. These can alter the nature of existing phase transition, and create new phase transitions in systems [102, 103].

A **Griffiths phase** is a phase that emerges from structural heterogeneities [104–107]. It stretches the region with critical properties from a point (the critical point) to a phase (the Griffiths phase, see Fig. 2.5B). Thus, instead of the system adapting its topology and parameters to become critical (as in SOC), dynamics with critical properties are built-in in the static topology of the network.

One type of structural heterogeneity is the addition of a modular structure in the network. It was shown that, by making the network hierarchically-modular (i.e. made of clusters inside clusters), DP class models exhibited their characteristic power-laws in a much larger region than if the network was random [107]. This result is particularly interesting in the context of neuronal networks, as the brain is known to have a modular structure [108, 109]. Thus, both SOC and Griffiths phase are possible mechanisms to explain criticality in the brain: SOC through activity-dependent adaptation, and Griffiths phase through special, heterogeneous topology.

---

[15] In statistical physics this is known as *quenched disorder*, due to it not being dependent on dynamics ("quenched").

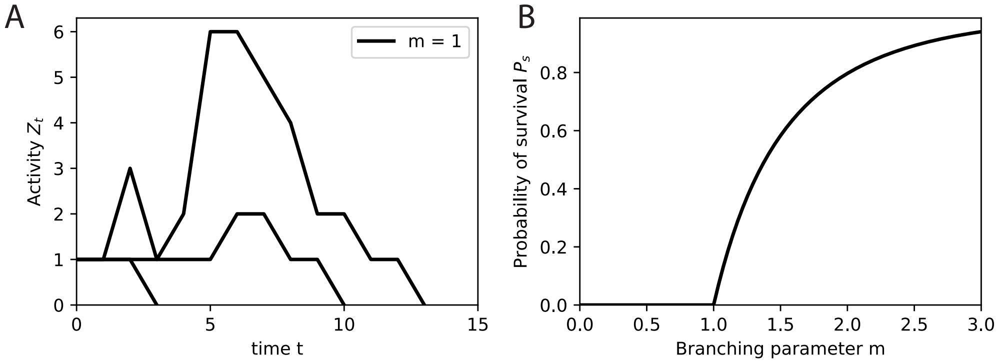

Figure 2.6: **The Galton-Watson branching process. A**. Example timeseries from a critical ($m = 1$) process, with activity dying out at different timesteps. **B**. The probability of survival P_s for $t \to \infty$, as a function of the branching parameter m. The system undergoes a continuous phase transition at $m = 1$, below which activity surely dies out.

2.4 THE BRANCHING PROCESS

2.4.1 *Definition*

A branching process (BP)is a stochastic model with discrete time where each individual unit at time t produces a random number of offspring at time $t + 1$. It was initially studied in the context of family names, and later found broad utility in fields such as genetics and nuclear physics [110].

The simplest version of the BP is known as the *Galton-Watson branching process*. It is defined as follows: let $\{X_{t,i} : t, i \in \mathbb{N}\}$ be independent and identically distributed (i.i.d.) random variables with non-negative integer values. Their probability distribution $P(X)$ must satisfy $P(X = 0) > 0$ and $P(X = 0) + P(X = 1) < 1$. Let Z_t denote the state of the process at time t. Then the evolution of Z_t obeys the following recursive relation

$$Z_{t+1} = \sum_{i=1}^{Z_t} X_{t,i} \tag{2.16}$$

We can interpret Z_{t+1} as the number of units at time $t + 1$, given by Eq. 2.16 as the sum of the random number of offspring of each unit at time t. Note that Z_{t+1} depends only on Z_t, and therefore it is an example of a Markov chain. The Galton-Watson process also makes the simplifying assumptions that the process starts with $Z_0 = 1$ (one unit) and that the process is stationary (offspring probability is time-independent). Note that the state $Z_t = 0$ is absorbing, as it results in $Z_{t'} = 0$ for $t' > t$. This is an example of the avalanche dynamics described in Sec. 2.2.2. In Fig. 2.6A we plot example timeseries of how the process looks like.

The dynamics of a BP is characterized by the expectation (mean) and variance of the probability distribution of X. In particular, the expectation

$$m = \langle X \rangle \tag{2.17}$$

is known as the **branching parameter** of the dynamics. In terms of phase transitions, m is the control parameter of the dynamics — the key properties of the process can be manipulated by changing m. Similarly to the contact process of Sec. 2.1, the critical point of a branching process is at $m = 1$.

This can be seen by taking the expectation from both sides of Eq. 2.16, which results in $\langle Z_{t+1} \rangle = m \langle Z_t \rangle$. From this we see that, on average, activity grows (geometrically) without bounds for $m > 1$ and decreases to zero for $m < 1$. At the critical point $m = 1$ activity is unstable: it ultimately goes to either 0 or ∞, but can take a long time to do so[16]. Note that, due to the dynamics being stochastic, even for $m > 1$ there is always a non-zero probability that activity dies out. However, if $m < 1$ activity will die out with certainty.

The probability of survival $P_S(t)$ at time t can be calculated recursively, for an arbitrary distribution $P(X)$, in the formalism of probability generating functions [110]. If $X \sim \text{Poisson}\,(m)$, then P_s is given by

$$P_s\,(t+1) = 1 - e^{-mP_s(t)} \tag{2.18}$$

Since $P_s\,(t+1) \leq P_s\,(t)$ (as activity must survive for t steps to survive for $t+1$ steps), it must converge at least asymptotically to some value for $t \to \infty$. Defining $P_s \equiv P_s\,(t+1) = P_s\,(t)$ we find

$$P_s = 1 + \frac{1}{m} W_0\left(-me^m\right) \tag{2.19}$$

where $W_0(k)$ is the principal branch of the Lambert W function[17]. In Fig. 2.6B we plot the result. It confirms our earlier statement: for $m \leq 1$ the activity surely dies out, but $m > 1$ doesn't guarantee survival. Notice also the similarity between Fig. 2.1B for the contact process and Fig. 2.6B for the branching process: while the functional shape in the active (supercritical) phase is different, both processes go through a continuous phase transition at $m = \lambda = 1$. As we shall discuss in Sec. 2.3.1, this is not a coincidence: both processes are members of the directed percolation (DP) universality class, meaning that at criticality they are the same.

Let us now consider an explicit example of a BP, inspired by neuronal activity. Consider a system where activity propagates from each active unit (e.g. spiking neuron) with probability p independently to each of its K neighbors. If the number of offspring from unit i at time t is given by $X_{t,i}$, then the probability of l offspring is

$$P\left(X_{t,i} = l\right) = \binom{K}{l} p^l \left(1-p\right)^{K-l} \tag{2.20}$$

---

[16] See [110] for a proof.

[17] Also known as the product logarithm function, it is defined as a solution of $W(z)e^{W(z)} = z$.

and the probability distribution is binomial: $X \sim \mathrm{Binom}\,(K, p)$. From Eq. 2.17, the branching parameter of this model is simply $m = \langle X \rangle = Kp$. Thus, in order to reach criticality ($m = 1$) the microscopic variable p must be set to $p_c = 1/K$.

We can interpret this simple model as activity spreading in a neuronal network in a probabilistic manner. Activity is not determined by firing rates, but by the actual spike trains. In that case, the microscopic variable p corresponds to the post-synaptic efficacy of each neuron. The model suggests that the global phase of the dynamics can be manipulated by changing the (microscopic) synaptic strength. It also predicts that, at criticality, the average efficacy of each synapse should scale as $\sim 1/K$ with number of synapses.

Since neurons are estimated to have on the order of $K \sim 10^4$ synapses, it can be shown that in this regime the binomial distribution can be approximated by a Poisson distribution: $X \sim \mathrm{Poisson}\,(\mathrm{m} = \mathrm{Kp})$. For practicality, we shall use this variant to simulate the Galton-Watson BP. It is worth noting that, while the number of activated units from a single unit is random (Poissonian), the number of units that try to activate others is given by the previous timestep, and thus the dynamics can still be highly correlated.

2.4.2 *Driven processes*

The Galton-Watson branching process lacks some important features that limit its usefulness in modeling neuronal activity. In particular, we have seen that it cannot sustain activity without necessarily blowing up.

We can solve this by adding a source of positive noise (or *drive*) to the dynamics of eq. 2.16. If we now denote the number of active units by A_t, a possible realization is as follows[18]:

$$A_{t+1} = \sum_{i=1}^{A_t} X_{t,i} + H_t \tag{2.21}$$

where H_t are non-negative, integer i.i.d random variables with $P(H > 0) > 0$. As before, $X_{t,i}$ are i.i.d non-negative integer random variables with mean $m = \langle X \rangle$. This is known as a *driven branching process*, or a *branching process with immigration* [111, 112].

The driven BP results in a non-zero probability that activity is spontaneously created, and thus the state $A_t = 0$ is no longer absorbing. In other words, there is no phase transition for non-zero drive, and the system cannot be actually critical. Nevertheless, for a relative small drive H_t it maintains many of its hallmark properties. Thus, as is commonly done in the literature, we adapt the nomenclature of the BP and call a driven system with e.g. $m < 1$ as "subcritical".

If the process has $m < 1$ ("subcritical") and H has finite mean $h = \langle H \rangle$, then Eq. 2.21 describes a stationary process with distribution A_∞. We can find its

---

[18] We switch notation here because while classic literature on BPs typically use Z_t, modern literature mentioning driven processes use A_t. Thus, in this thesis Z_t denotes a Galton-Watson BP, while A_t means a driven BP.

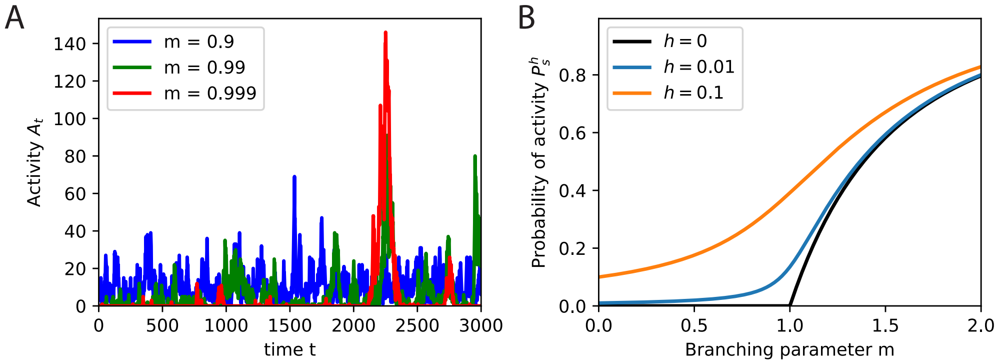

Figure 2.7: **The driven branching process. A**. Example timeseries from driven branching processes with branching parameter $m < 1$. The average activity of each timeseries is set at $\langle A_\infty \rangle = 10$, and the drive h is adjusted using Eq. 2.23. We see that, as m increases, so does the variance of the timeseries. **B**. Probability of activity P_s^h as a function of m and h, using Eq. 2.30. $h > 0$ smears out the phase transition of Fig. 2.6B, increasing the probability of activity.

stationary activity rate $\langle A_\infty \rangle \equiv \langle A_{t+1} \rangle = \langle A_t \rangle$ by taking the expectation of Eq. 2.21:

$$\langle A_{t+1} \rangle = \sum_{i=1}^{A_t} \langle x_{t,i} \rangle + \langle H_t \rangle = m \langle A_t \rangle + h \tag{2.22}$$

and thus

$$\langle A_\infty \rangle = \frac{h}{1-m} \tag{2.23}$$

From Eq. 2.23 we see that $\langle A_\infty \rangle$ depends on both the branching parameter m and the mean drive h. Thus, it is possible to have processes with the same rate at different distances to criticality $\epsilon = 1 - m$ by adjusting both m and h. In Fig. 2.7A we plot example timeseries $A_t(m)$ with the same average rate $\langle A_\infty \rangle = 10$.

While the timeseries A_t in Fig. 2.7A have the same average rate, they look very different. We can quantify that by calculating the variance $\mathrm{Var}\left[A(t+1)\right]$ of a driven BP. From the law of total variance, we have:

$$\mathrm{Var}\left[A_{t+1}\right] = \langle \mathrm{Var}\left[A_{t+1} | A_t\right] \rangle + \mathrm{Var}\left[\langle A_{t+1} | A_t \rangle\right] \tag{2.24}$$

where $\langle \cdot | \cdot \rangle$ and $\mathrm{Var}\left[\cdot|\cdot\right]$ denote respectively conditional expectation and variance. Denoting $\sigma^2 = \mathrm{Var}\left[X\right]$ and $\xi^2 = \mathrm{Var}\left[H\right]$, from Eq. 2.21 we have:

$$\mathrm{Var}\left[A_{t+1} | A_t\right] = \sum_{i=1}^{A_t} \mathrm{Var}\left[x_{t,i} | A_t\right] + \mathrm{Var}\left[H_t | A_t\right] = A_t \sigma^2 + \xi^2 \tag{2.25}$$

$$\mathrm{Var}\left[\langle A_{t+1} | A_t \rangle\right] = \mathrm{Var}\left[m A_t + h\right] = m^2 \mathrm{Var}\left[A_t\right] \tag{2.26}$$

Applying Eqs. 2.25 and 2.26 on Eq. 2.24 we find:

$$\mathrm{Var}\left[A_{t+1}\right] = \sigma^2\langle A_t\rangle + \xi^2 + m^2\mathrm{Var}\left[A_t\right] \tag{2.27}$$

The stationary variance can be calculated taking $\mathrm{Var}\left[A_\infty\right] \equiv \mathrm{Var}\left[A_{t+1}\right] = \mathrm{Var}\left[A_t\right]$ and using Eq. 2.23:

$$\mathrm{Var}\left[A_\infty\right] = \sigma^2\frac{h}{1-m} + \xi^2 + m^2\mathrm{Var}\left[A_\infty\right]$$

$$\mathrm{Var}\left[A_\infty\right] = \frac{1}{1-m^2}\left(\xi^2 + \sigma^2\frac{h}{1-m}\right) \tag{2.28}$$

From Eq. 2.28 we see that the variance $\mathrm{Var}\left[A_\infty\right]$ of the timeseries A_t depends heavily on m, and diverges as $m \to 1$. This explains the difference in "burstiness" in the timeseries of Fig. 2.7A. It is important to note that $\mathrm{Var}\left[A_\infty\right]$ depends on both mean (m, h) and variance (σ^2, ξ^2) of X and H. This contrasts to the mean rate $\langle A_\infty\rangle$ (Eq. 2.23), which only depends on the mean. In other words, details of how the drive is implemented in the BP (given by its variance) do not matter in order to calculate the mean rate, but do matter in terms of its spread.

As mentioned above, adding drive changes how we interpret the process. Since there is no quiescent phase (as $A_t = 0$ is not absorbing), formally the process does not undergo a phase transition anymore. We can shed light into this by calculating the probability $P_s^h(t)$ of observing activity at some time t. Starting from Eq. 2.18, we note that $e^{-mP_s(t)}$ can be interpreted as the probability that activity dies out after time t. Thus, $P_s^h(t)$ is given by one minus $e^{-mP_s(t)}$ times the probability that the drive does not restart activity:

$$P_s^h(t+1) = 1 - e^{-mP_s(t)}\left(1 - H_t\right) \tag{2.29}$$

Again solving it for $P_s^h \equiv P_s^h(t+1) = P_s^h(t)$ and $h = \langle H_t\rangle$ yields

$$P_s^h = 1 + \frac{1}{m}W_0\left(-me^m\left[1-h\right]\right) \tag{2.30}$$

which we remind is also valid for $m > 1$. In Fig. 2.7B we plot Eq. 2.30 for some values of h.

Comparing Fig. 2.6B and Fig. 2.7B we see that $h > 0$ smears the phase transition of the Galton-Watson BP, which is recovered for $h \to 0$. While we have stated that the main properties of the BP are maintained in the driven BP (such as correlation length), they are obviously different models. Exactly how the properties of the driven BP diverge from the Galton-Watson BP is still an open topic[19].

In particular, making the BP driven complicates the observation of its avalanche dynamics. For large drives, the system loses its separation of timescales (STS),

---

[19] In Physics, this is equivalent to e.g. the addition of an external magnetic field to the Ising model. Interestingly, the Ising model with non-zero field is considered to be analytically not solvable in all but the one-dimensional case [12].

and activity is continuous. Thus, avalanches are not defined to begin with. A popular way to circumvent this is to threshold the activity timeseries [78], though this was shown to produce bias [113–115]. Even in driven systems with STS, it was shown that large drives can change the power-law (critical) exponents of the avalanche dynamics [116]. Nevertheless, for small enough values of h the properties for $m \to 1$ are very similar to the true critical process.

From the point of view of neuronal activity, the drive can be interpreted as both spontaneous activity (which is observed during development [117]) or input from other brain regions that are not part of the system in question. Thus, the driven BP has two sources of activity: one correlated, composed of the self-generated recurrent dynamics, and one uncorrelated, composed of external factors.

2.4.3 *Branching networks*

A second issue with the Galton-Watson branching process is that it does not incorporate network effects from the neuronal substrate where activity takes place. This can be addressed by running the branching process dynamics on a network, usually called a *branching network*.

Embedding the dynamics on a network adds another dimension of complexity to the model, as the precise network topology can heavily influence the dynamics. For instance, while so far the phase transition considered depends on a dynamical parameter, it is also possible for it to be *topological*. Such a topological phase transition can then dramatically change the dynamics. In other words, by changing network properties (such as average degree or degree distribution) we can indirectly control the dynamics. The necessary conditions to control a system towards specific dynamical states through topology is the object of study of network control theory [118, 119].

As an example of a topological phase transition affecting dynamics, consider an Erdős–Rényi (ER) network[20] with average degree K. The giant component C corresponds to the largest fraction of the network that is causally connected (i.e. there is a path between any two nodes). The giant component is implicitly given by $C = 1 - e^{-KC}$ [120], which is the same functional form as Eq. 2.18. Thus, network connectivity undergoes a phase transition at $K = 1$, identical in form to the one shown in Fig. 2.6B. For $K < 1$ the size of the largest connected component does not scale with the size N of the network, and $C \to 0$ as $N \to \infty$. For $K > 1$ an extensive fraction of the network is connected, at any size. Thus, for any dynamics that may run on it, the subcritical regime $K < 1$ dramatically impacts network activity by simply prohibiting its spreading.

As an example of topological effects on the branching network, consider a driven BP on a regular network where each node has K neighbors. As each active

---

[20] In an Erdős–Rényi network each possible link between the N nodes exists with probability p. Thus, the degree distribution is binomial and $K = Np$.

node can independently activate each of its K neighbors, the distribution $P(X)$ of the branching dynamics is binomial: $X \sim \mathrm{Binom}(K, m/K)$. We then have

$$\sigma^2 = \mathrm{Var}\left[X\right] = m\left(1 - \frac{m}{K}\right) \tag{2.31}$$

and thus increasing K increases the variance σ^2. From Eq. 2.28, this increase in σ^2 results in a linear increase in the variance of the process $\mathrm{Var}\left[A_\infty\right]$. In other words, increasing the connectivity increases the burstiness of the dynamics, even if the average activity rate is kept constant.

When simulating branching networks, an important effect is *coalescence* [111]. Since the dynamics now spreads in a finite system, there is the possibility that two nodes try to activate the same node at the same time. This results in a loss of activity, decreasing the effective branching parameter of the dynamics. This is the mechanism that guarantees finite activity even if we set $m \geq 1$.

How much activity gets lost from coalescence depends on depends on both topology and dynamics. Regarding topology, the more local the spreading the higher the coalescence (such as the one in Chapter 4). From the dynamics, coalescence depends chiefly on amount of activity.

Coalescence effects also mean that the microscopic m we put into the system differs from the macroscopic $\hat{m}_{LR}$ we obtain from the global dynamics. Consider a BP with branching parameter m and drive h on a fully-connected network with N nodes. The branching parameter can be estimated from the global dynamics with

$$\langle A_{t+1} \rangle = \hat{m}_{LR} \langle A_t \rangle + h \tag{2.32}$$

In Fig. 2.8 we reproduce the resulting discrepancy $m - \hat{m}_{LR}$ for different N, adapted from [111]. In the non-driven branching network (Fig. 2.8A) coalescence results in $\hat{m}_{LR} < 0.999$ when setting $m = 1$, even for networks with up to $N = 10^6$. For the driven BP, on the other hand, the higher level of activity results in a much larger coalescence effect (Fig. 2.8B). For instance, setting $m = 1$ and $h = 10^{-3}$ results in $\hat{m}_{LR} \approx 0.95$.

While this may seem a small difference, recall that many properties are maximized at criticality. Thus, a difference of $1 - 2\%$ in m near the critical state can result in considerably different functional properties. Thus, while a branching network is an interesting extension of the BP with many applications, it comes with a number of caveats and technical challenges. Not accounting for them can result in errors, such as setting $m = 1$ in a branching network and naively claiming that the system is critical.

In the context of neuronal activity, both synaptic plasticity and the extreme structural heterogeneity of brain regions can be considered examples of topological effects. Indeed, the study of how to control neuronal activity using tools from network control theory is an increasingly active area of research [121–126]. As we have seen in Sec. 2.3, in critical phenomena network effects also play an important role.

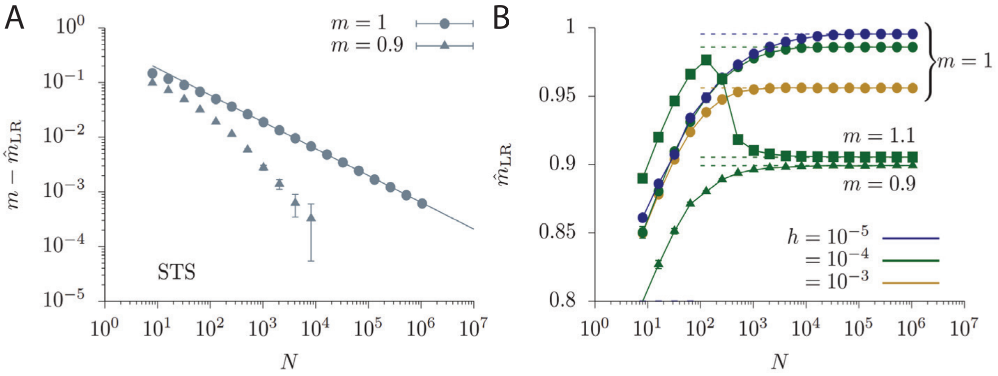

Figure 2.8: **Coalescence effects on branching networks. A**. Difference between the true branching parameter m and the parameter estimated from the macroscopic dynamics $\hat{m}_{LR}$ with no drive ($h = 0$) for fully-connected branching networks with size N. **B**. Same as A for driven branching networks with drive h. Adapted with permission from [111].

2.4.4 *Functional properties*

The branching process exhibits the properties described in Sec. 2.2. Two properties will be particularly relevant later: the autocorrelation function (Sec. 2.2.1) and the avalanche distributions (Sec. 2.2.2). The autocorrelation function $C(t)$ of a BP is exponential:

$$C(t) = e^{-t/\tau} \tag{2.33}$$

where

$$\tau = -\frac{1}{\log m} \tag{2.34}$$

is the autocorrelation time of the BP[21]. Here we see an example of a diverging property at criticality, as $m \to 1$ results in $\tau \to \infty$. Moreover, changing from e.g. $m = 0.9$ to $m = 0.99$ results in more than a 100-fold increase in τ.

To demonstrate that, recall that if a branching process is driven and subcritical, we have shown in Sec. 2.4.2 that it is stationary with average activity $\langle A_\infty \rangle = h/(1-m)$. In that case, the autocorrelation function $C(t)$ is just the correlation between activity at an arbitrary time k and some other time $k+t$:

$$\begin{aligned} C(t) &= \operatorname{corr}\left(A_{k+t}, A_k\right) \\ C(t) &= \frac{\langle A_{k+t} A_k \rangle - \langle A_k \rangle^2}{\langle A_k^2 \rangle - \langle A_k \rangle^2} = \frac{\langle \langle A_{k+t} | A_k \rangle A_k \rangle - \langle A_k \rangle^2}{\langle A_k^2 \rangle - \langle A_k \rangle^2} \end{aligned} \tag{2.35}$$

---

[21] The autocorrelation time here is in units of timesteps. When dealing with real systems it becomes $\tau = -\Delta t / \log m$, where Δt is the timestep duration (in seconds) of the dynamics

where the last equality uses the law of total expectation. The value $\langle A_{k+t} | A_k \rangle$ can be computed using Eq. 2.22 recursively:

$$\begin{aligned}
\langle A_{k+t} | A_k \rangle &= m \langle A_{k+t-1} | A_k \rangle + h \\
&= m \left(m \langle A_{k+t-2} | A_k \rangle + h \right) + h \\
&= m^t \langle A_k | A_k \rangle + h \sum_{i=1}^{t} m^{t-i} \\
&= m^t A_k + h \frac{1 - m^t}{1 - m}
\end{aligned} \tag{2.36}$$

where the last equality uses the fact that $\langle A_k | A_k \rangle = A_k$ and $\sum_{i=1}^{t} m^{t-i} = \left(m^t - 1 \right) / (m-1)$. Since $\langle A_k \rangle = \langle A_\infty \rangle$, we have

$$\langle A_{k+t} | A_k \rangle = m^t \left(A_k - \langle A_k \rangle \right) + \langle A_k \rangle \tag{2.37}$$

Applying Eq. 2.37 in Eq. 2.35 yields:

$$\begin{aligned}
C(t) &= \frac{\langle \left[m^t \left(A_k - \langle A_k \rangle \right) + \langle A_k \rangle \right] A_k \rangle - \langle A_k \rangle^2}{\langle A_k^2 \rangle - \langle A_k \rangle^2} \\
&= \frac{\langle m^t A_k^2 - m^t \langle A_k \rangle A_k + \langle A_k \rangle A_k \rangle - \langle A_k \rangle^2}{\langle A_k^2 \rangle - \langle A_k \rangle^2} \\
&= \frac{m^t \langle A_k^2 \rangle - m^t \langle A_k \rangle^2}{\langle A_k^2 \rangle - \langle A_k \rangle^2} = m^t
\end{aligned} \tag{2.38}$$

Since here t is the variable and m is a parameter, it makes sense to write it as

$$C(t) = e^{t \ln m} = e^{-t/\tau} \tag{2.39}$$

with $\tau = -1/\ln m$.

Meanwhile, at criticality the avalanche size distribution $p(S)$ and the avalanche duration distribution $p(D)$ are power-laws with critical exponents $\alpha = 3/2$ and $\beta = 2$, respectively [110]. The average avalanche size $\langle S \rangle (D)$ is a power-law with exponent $\gamma = 2$. Moreover, the average temporal profile follows Eq. 2.8 where $\mathscr{F}$ is a bell-shaped (parabolic) curve. In summary, we have:

$$\begin{aligned}
p(S) &\sim S^{-3/2} \\
p(D) &\sim D^{-2} \\
\langle S \rangle &\sim D^2 \\
s(t, D) &\sim D \mathscr{F}(t/D)
\end{aligned} \tag{2.40}$$

In Fig. 2.9 we plot the avalanche observables for simulations of a Galton-Watson BP with varying branching parameter m. Notice how the distance from criticality $\epsilon = 1 - m$ affects the observables: while the true critical state $m = 1$ results

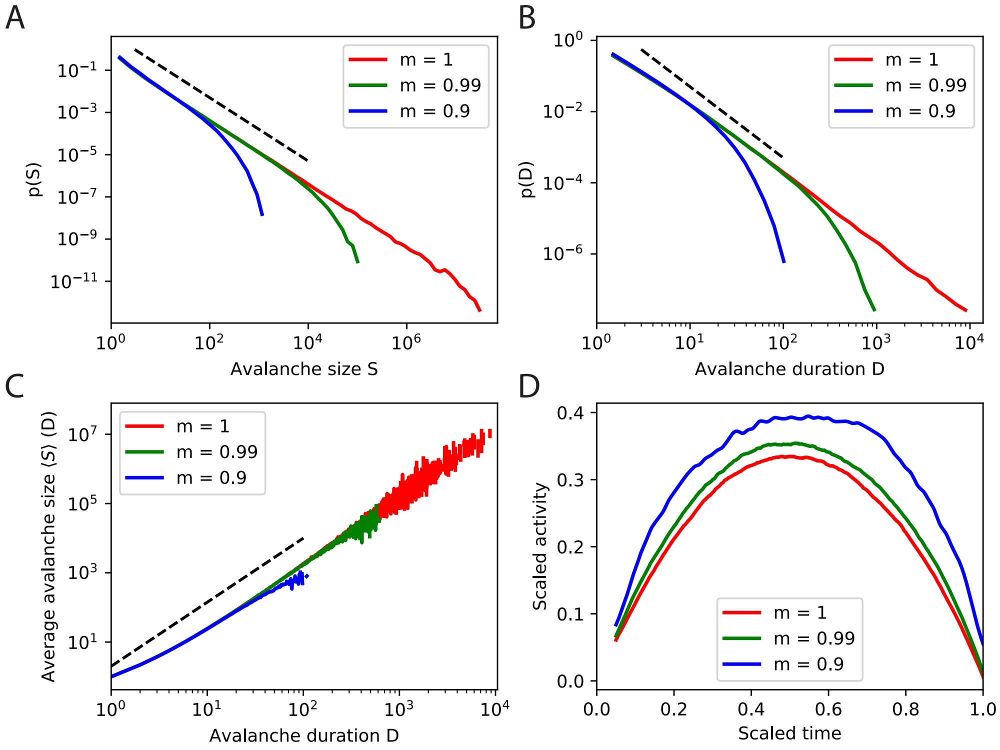

Figure 2.9: **Avalanche observables of a Galton-Watson branching process. A**. Avalanche size distribution $p(S)$ for BPs with $m = 1$ (red), $m = 0.99$ (green) and $m = 0.9$ (blue). Dashed line corresponds to $p(S) \sim S^{-3/2}$. **B**. Same as A for the avalanche duration distribution $p(D)$. Dashed line corresponds to $p(D) \sim D^{-2}$. **C**. Same as A for the average avalanche size $\langle S \rangle$ of a given duration D. Dashed line corresponds to $\langle S \rangle \sim D^2$. **D**. Scaled average avalanche shape $s(t, D)/D^{\gamma-1}$ as a function of the scaled time t/D. Simulations are from a Poissonian BP ($X \sim \text{Poisson}(m)$) with 10^6 avalanches for each m.

in $p(S)$ spanning 8 orders of magnitude[22] using $m = 0.99$ cuts it to 4 orders of magnitude (with the same number of avalanches), and $m = 0.9$ to 2 orders of magnitude. The results of $p(D)$ are even more extreme, as $m = 0.9$ cuts the power-law behavior to roughly 1 order of magnitude. Thus, even in the most simple and controllable example of a BP it is not possible to fit $p(D)$ of a process with $m = 0.9$ to data and reliably extract the exponent.

While the critical exponents $\alpha = 3/2$, $\beta = 2$ and $\gamma = 2$ are often mentioned in the context of branching processes, the precise form of the distributions are rarely shown. The reason behind this is that the exact shapes of the avalanche size distribution $p(S)$ and avalanche duration distribution $p(D)$ depend on the

---

[22] Due to it being a simulation, we limit the maximum duration in Fig. 2.9 to $D = 10^4$ steps, which limits the range of $p(D)$ and $\langle S \rangle(D)$. Since $\langle S \rangle \sim D^2$, this results in a maximum average size of $S \sim 10^8$, which limits the range of $p(S)$. In principle, however, the power-laws for $m = 1$ stretch forever.

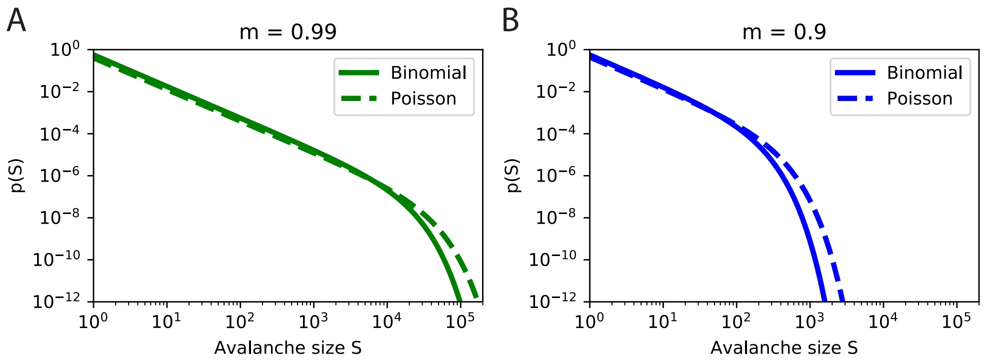

Figure 2.10: **Analytic solutions for $p(S)$ of Binomial and Poisson Galton-Watson BP.** **A**. $p(S)$ for $X \sim \text{Binom}(2, m/2)$ (full line, Eq. 2.41) and $X \sim \text{Poisson}(m)$ (traced line, Eq. 2.42), for $m = 0.99$. **B**. Same as A for $m = 0.9$.

details of the implementation (e.g. the probability distribution the number of offspring is drawn from). This means that how the distributions deviate from the pure power-laws in the subcritical case ($m < 1$) depends on the microscopic details of the process. Only as $m \to 1$ these details become unimportant and the asymptotic power-laws emerge.

As examples, consider Galton-Watson BPs with $X \sim \text{Binom}(2, m/2)$ and $X \sim \text{Poisson}(m)$. The first represents a binomial process with at most $K = 2$ offspring per active site, while the second represents the continuous $K \to \infty$ Poisson process. From combinatorial considerations [116], for the binomial case the full expression for $p(S)$ (minus normalization constants) is given by:

$$p(S) \sim [2m(1 - m/2)]^S S^{-3/2} \tag{2.41}$$

while the same expression [127] for the Poisson case is:

$$p(S) \sim e^{S(1-m)} m^{S-1} S^{-3/2} \tag{2.42}$$

We can see that only for $m \to 1$ both expressions reduce to $p(S) \sim S^{-3/2}$. In Fig. 2.10 we compare these expressions. We observe that, for the same m, the distributions for the Poisson BP extend further than for the Binomial BP.

While for the avalanche distributions having $m < 1$ results in shorter distributions, for the avalanche shape $s(t, D)$ it results in a deviation from the characteristic bell-shaped curve $\mathscr{F}(t/D)$ (see Fig. 2.9D). Moreover, as we see in Fig. 2.11, $m < 1$ also causes deviations of the exponent γ used to collapse all the shapes from the analytical result of $\gamma = 2$. Using a variance minimization algorithm [128], we obtain $\gamma = 1.95$ for our simulations of a critical ($m = 1$) BP, while subcritical ($m = 0.90$) dynamics results in $\gamma = 1.77$. It is worth nothing that the bell-shaped curve $\mathscr{F}$ is characteristic of processes with $\gamma = 2$ [129]. For processes with e.g. $\gamma = 3/2$ (such as the unbiased Random Walk) it is a semicircle instead [130].

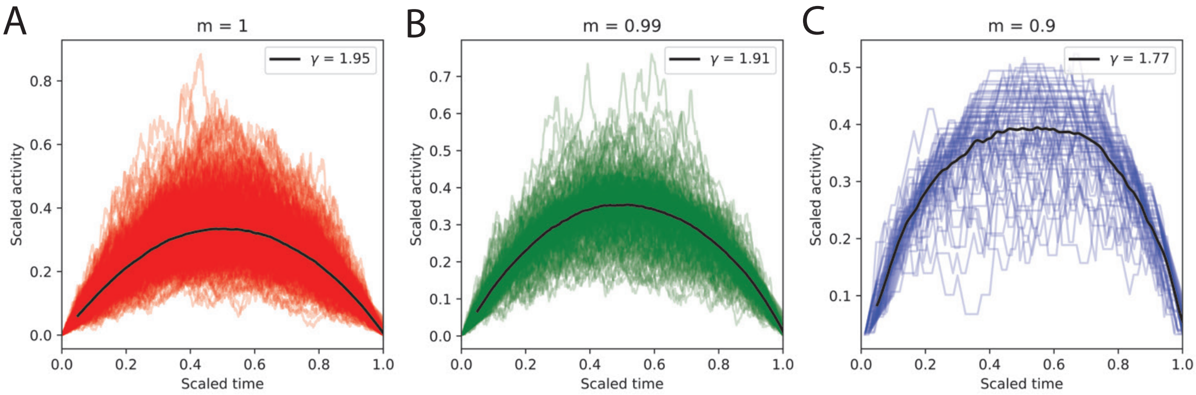

Figure 2.11: **Avalanche shape collapse of a Galton-Watson branching process. A**. Scaled average avalanche shape $s(t, D)/D^{\gamma-1}$ as a function of the scaled time t/D for $m = 1$. The black line corresponds to the average shape, while the semi-transparent lines correspond to the average shape of avalanches with the same duration D. **B**. Same as A for $m = 0.99$ **C**. Same as A for $m = 0.9$ Simulations are from a Poissonian BP $(X \sim \text{Poisson}(m))$ with 10^6 avalanches for each m.

A last property worth mentioning is the susceptibility $\chi = \partial\langle A_\infty\rangle/\partial h$ for $h \to 0$. It reflects the average system response to a small perturbation. From Eq. 2.23, it is:

$$\chi = \lim_{h\to 0} \frac{\partial\langle A_\infty\rangle}{\partial h} = \frac{1}{1-m} \tag{2.43}$$

and thus it also diverges at criticality. In other words, as $m \to 1$ the system becomes increasingly sensitive to changes in the drive (e.g. stimuli).

2.5 SIGNATURES OF CRITICALITY IN NEURONAL DYNAMICS

2.5.1 *Neuronal avalanches*

The first notable evidence[23] for criticality in neuronal dynamics came from the seminal paper by Beggs & Plenz in 2003 [1]. Using local field potential recordings of neuronal cultures and slices (i.e. in vitro), they've shown that neuronal networks can display the avalanches of activity (known as *neuronal avalanches*) described in Sec. 2.2. Moreover, the avalanche size distribution followed a power-law $p(S) \sim S^{\alpha}$ with exponent[24] $\alpha = 3/2$. Estimating the branching parameter also yielded $m \approx 1$. Both measures, $\alpha = 3/2$ and $m \approx 1$, suggest dynamics of

---

[23] Theoretical arguments for criticality in the brain predate experimental evidence by at least a decade [2].

[24] In that, and other experiments, the obtained exponent varied with bin size Δt. This is discussed in Chapter 3.

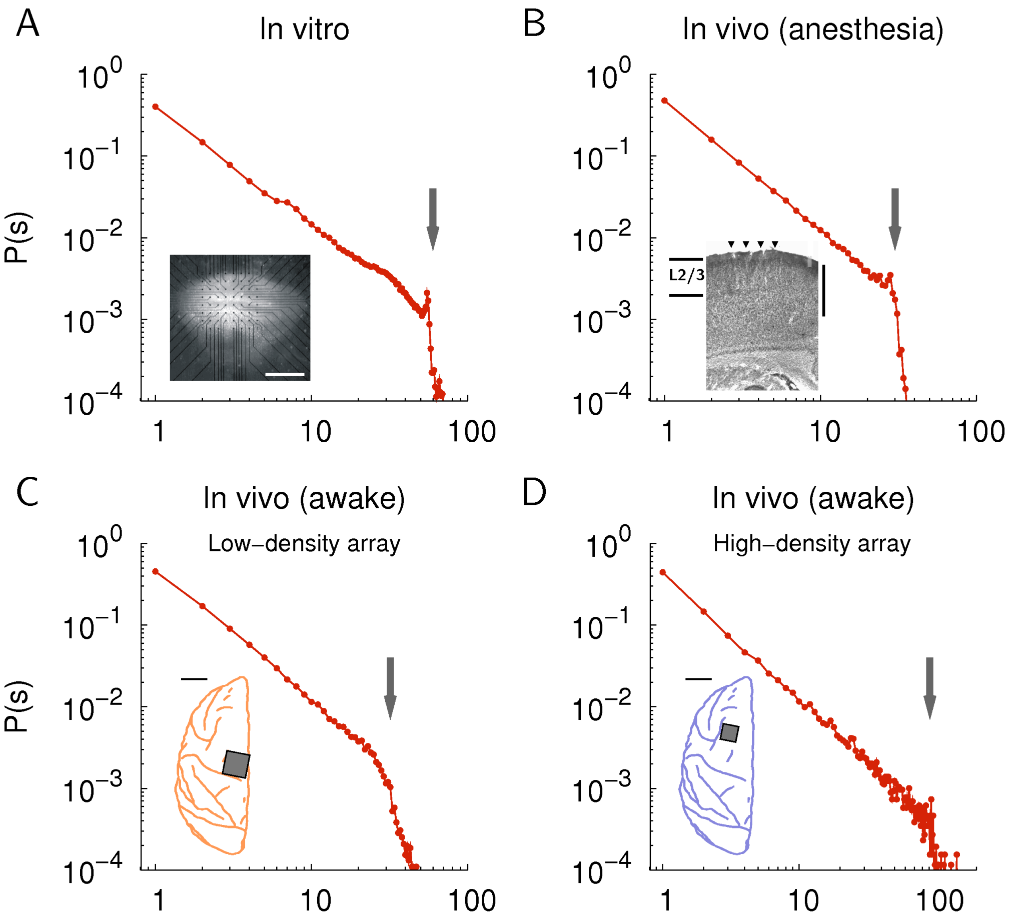

Figure 2.12: **Avalanche size distributions $p(S)$ from different studies using local field potentials. A:** $p(S)$ from *in vitro* cultures obtained in the original 2003 work by Beggs & Plenz [1]. **B:** $p(S)$ from anesthetized rats, from Gireesh *et al.* [131]. **C:** $p(S)$ from awake monkeys, from Petermann *et al.* [132]. **D:** $p(S)$ from awake monkeys with a high density (smaller) recording array, from Klaus *et al.* [133]. Figure adapted from [133]. doi:10.1371/journal.pone.0019779.g001

a critical branching process (see Sec. 2.4). This result sparked intense research on criticality in the brain. The avalanche size distribution obtained by Beggs & Plenz can be seen in Fig. 2.12A.

Following this pioneering work a wide body of research formed, claiming signatures of criticality in different experiments (see Fig. 2.12B-D). This suggested that criticality could be a universal, simple explanation for how the brain propagates activity. The neuronal networks studied ranged from cultures to awake animals of various species, with a wide variety of techniques.

Broadly, these techniques either aim to record the spiking activity of some individual neurons (spike detection), or to record some local average of the activ-

Table 2.1: Compilation of experimental findings of neuronal avalanches. For cultures, "region" corresponds to the brain region neurons were extracted from. Range of $p(S)$ was either given in the text, or estimated visually. Exponents with "$\approx$" are not explicitly fitted but instead visually compared.

authors	technique	region	system	exponent α	range of $p(S)$
Beggs *et al.*, 2003 [1]	LFP	cortex	culture	≈ 1.5	1-60
Gireesh *et al.*, 2008 [131]	LFP	cortex	culture	1.53 ± 0.02	1-32
Petermann *et al.*, 2009 [132]	LFP	cortex	monkey	≈ 1.5	1-32
Klaus *et al.*, 2011 [133]	LFP	cortex	monkey	≈ 1.5	1-96
Friedman *et al.*, 2012 [134]	spikes	cortex	culture	1.7	1-30
Meisel *et al.*, 2013 [135]	MEEG	whole head	human	≈ 1.5	1-27
Palva *et al.*, 2013 [136]	MEEG	whole head	human	1.31	1-66
Priesemann *et al.*, 2013 [137]	LFP	varied	human	1.58 ± 0.06	1-50
Shriki *et al.*, 2013 [138]	MEEG	whole head	human	≈ 1.5	1-100
Scott *et al.*, 2014 [139]	imaging	cortex	rat	≈ 1.5	1-1000
Arviv *et al.*, 2015 [140]	MEEG	whole head	human	1.50	1-100
Bellay *et al.*, 2015 [141]	imaging	cortex	rat	1.63 ± 0.13	0.01-10
Fagerholm *et al.*, 2015 [142]	imaging	cortex	rat	≈ 1.5	1-1000
Massobrio *et al.*, 2015 [143]	spikes	cortex	culture	1.48-1.52	1-500
Shew *et al.*, 2015 [144]	LFP	cortex (visual)	turtle	1.6-2.6	3-200
Clawson *et al.*, 2017 [145]	LFP	cortex (visual)	turtle	1.8 ± 0.3	2-500
Hahn *et al.*, 2017 [146]	spikes	cortex (visual)	monkey	1.58 ± 0.03	1-20
Levina *et al.*, 2017 [22]	spikes	cortex	culture	≈ 2	1-5900
Yaghoubi *et al.*, 2018 [147]	imaging	hippocampus	culture	1.65 ± 0.1	1-500
Ponce-Alvarez *et al.*, 2018 [148]	imaging	whole brain	zebrafish	2.01 ± 0.03	1-10000
Bocaccio *et al.*, 2019 [149]	imaging	whole head	human	≈ 2	1-1000
Kanders *et al.*, 2020 [150]	spikes	hippocampus	rat	2.18 ± 0.05	1-60

ity of many neurons, either directly or indirectly (using some activity correlate such as blood-level oxygenation). Thus, they not only record activity differently (directly vs indirectly), but also at different scales (single-neuron vs population). Techniques that record activity on a population scale include the aforementioned local field potential (LFP), and electroencephalography (EEG) and magnetoencephalography (MEG), with both collectively called MEEG [151]. Note, even between those, the difference in scale: while LFP recordings typically cover regions a few millimeters in size, an EEG cap covers the entire human head. More recently, studies also began using optical imaging techniques [141, 142,

Table 2.2: Scaling of experiments that measure the full set of power-laws.

Source	α	β	γ	$(\beta-1)\,/\,(\alpha-1)$
Branching process	3/2	2	2	2
Random walk	4/3	3/2	3/2	3/2
Friedman *et al.* [134]	1.7	1.9	1.3	1.3
Kanders *et al.* [150]	2.18	2.76	1.43	1.49
Ponce-Alvarez *et al.* [148]	2.01	3.01	1.85	1.99

147, 148]. Imaging techniques can in principle record up to single neuron activity [152–154]. While the temporal resolution at which they can record activity remains slower than the timescale of propagation, they hold great promise for future, fully-sampled studies of spiking activity.

In Table 2.1 we summarize the findings of a number of studies of neuronal avalanches. We see that indeed an impressive variety of experimental systems produced the same signature of criticality, namely that activity spreads in avalanches with $p(S) \sim S^{-\alpha}$. Measured exponents α also mostly agreed with the critical branching process value of $\alpha = 3/2$. Yet, it is important to notice some general aspects in those studies:

1. most of the analyzed regions are cortical.
2. range of power-law behavior is narrow, often below the standard of 2 orders of magnitude [27].
3. the majority of the evidence comes from non-spiking recordings (LFP, MEEG, imaging with coarse scales).

The first aspect is perhaps the most important: due to its functional role, the cortex is a natural region to study using critical phenomena. Yet, different regions of the brain can be very different from cortex both functionally and physiologically. The early visual system, for instance, makes use of very specific structures and neuronal types in order to process visual information — it is doubtful that critical phenomena could shed much light into its function. Thus, it is prudent to limit claims of criticality in vivo to the experiments with ample evidence: cortex, and large-scale whole-brain activity.

The second aspect is related to experimental constraints: number of recording sites, e.g. the number of electrodes in a multi-electrode array (MEA), limit the size of events that can be recorded. In particular, with non-spiking recordings (such as LFP and MEEG) the number of electrodes typically impose a hard cutoff on $p(S)$ [155].

The third aspect is related to spiking vs non-spiking recordings, and will be explored in detail in Chapter 4. Briefly, there we show that electrode-based non-

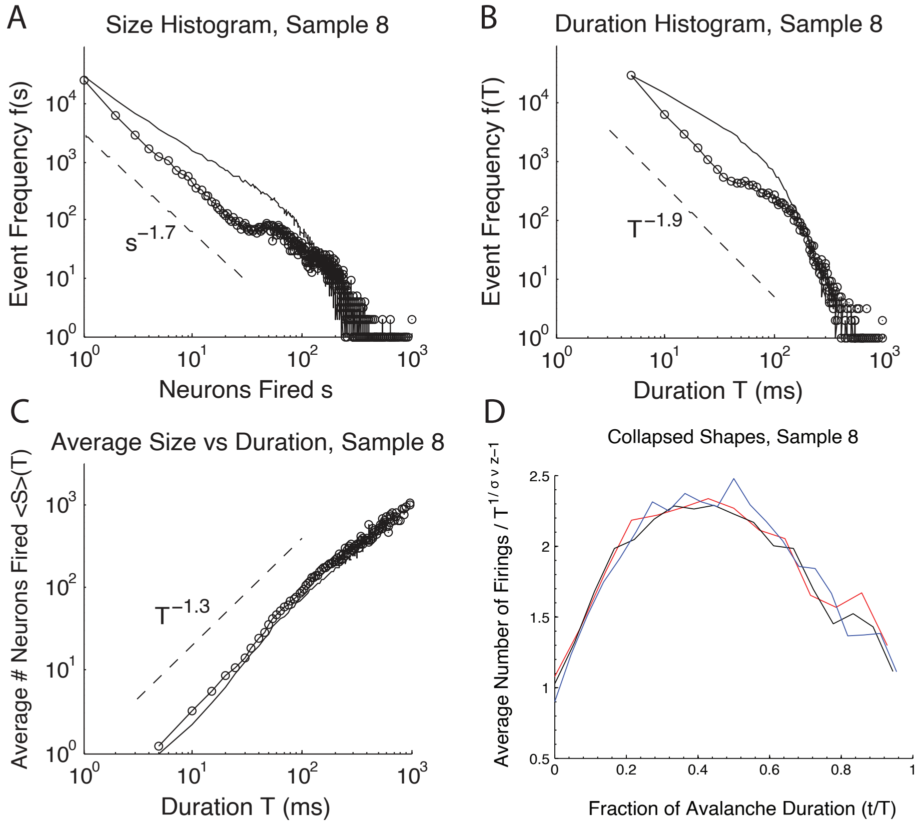

Figure 2.13: **Avalanche observables from Friedman *et al.* [134]. A.** Avalanche size distribution $p(S)$ from a sample culture, fitted to $p(S) \sim S^{-\alpha}$ with $\alpha = 1.7$. **B.** Same as A for the avalanche duration distribution $p(D)$, fitted to $p(D) \sim D^{-\beta}$ with $\beta = 1.9$. **C.** Same as A for the average avalanche size $\langle S \rangle(D)$, fitted to $\langle S \rangle \sim S^{\gamma}$ with $\gamma = 1.3$. **D.** Scaled average avalanche shape $s(t, D)/D^{\gamma-1}$ as a function of the scaled time t/D. Adapted from [134].

spiking recordings are less sensitive, and cannot distinguish critical from considerably subcritical dynamics.

Nevertheless, there is compelling evidence for criticality *in vitro*: in the work by Levina & Priesemann [22], for instance, the obtained $p(S)$ followed a power-law over a large range. Importantly, both in Friedman *et al.* [134] and Kanders *et al.* [150] the full set of scaling relationships from a critical system was obtained. See respectively Fig. 2.13 and Fig. 2.14 for the results, which are qualitatively comparable to the observables of the Galton-Watson BP (Fig. 2.9).

In vivo, on the other hand, to the best of our knowledge the only evidence for the full set of scaling relationships comes from Ponce-Alvarez *et al.* [148]. In this study, Light Sheet Fluorescence Microscopy is used to image the whole-brain dynamics of zebrafish larvae. The technique offers good spatial resolution, with $\sim 10^4$ regions of interest (ROI) composed of few or single neurons. However,

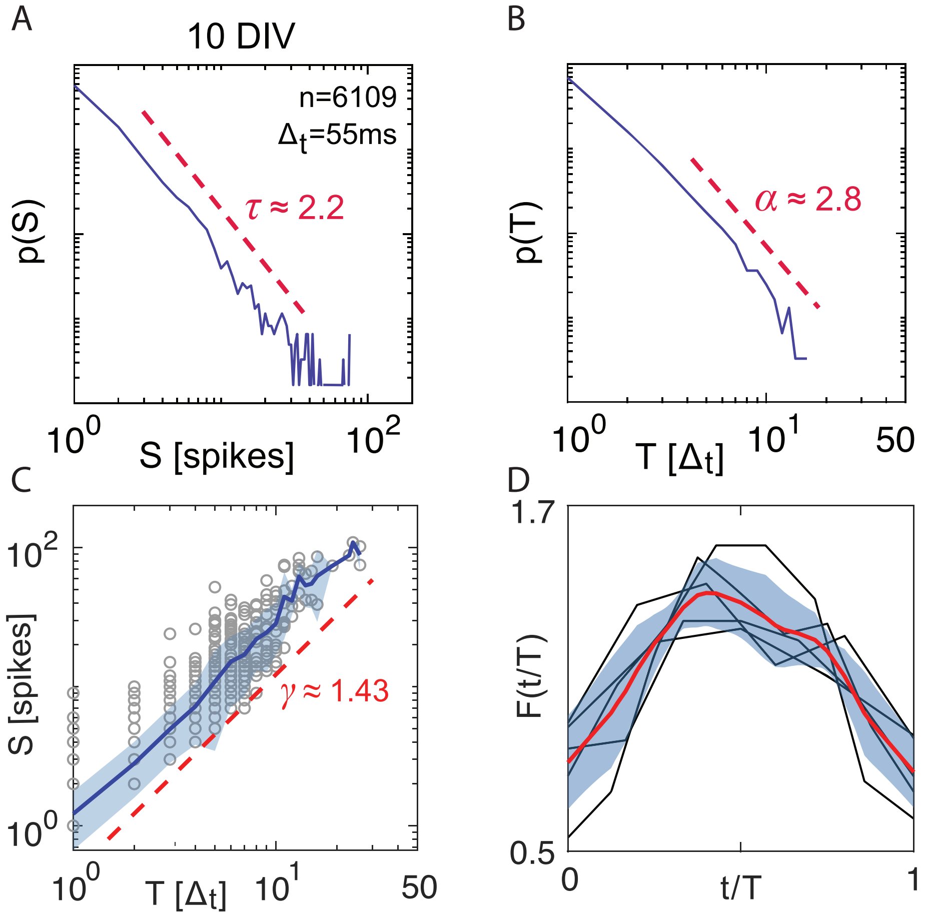

Figure 2.14: **Avalanche observables from Kanders *et al.* [150]. A.** Avalanche size distribution $p(S)$ from a sample culture, fitted to $p(S) \sim S^{-\alpha}$ with $\alpha = 2.18 \pm 0.05$. **B.** Same as A for the avalanche duration distribution $p(D)$, fitted to $p(D) \sim D^{-\beta}$ with $\beta = 2.76 \pm 0.16$. **C.** Same as A for the average avalanche size $\langle S \rangle (D)$, fitted to $\langle S \rangle \sim S^{\gamma}$ with $\gamma = 1.43 \pm 0.05$. **D.** Scaled average avalanche shape $s(t, D)/D^{\gamma - 1}$ as a function of the scaled time t/D. Adapted from [150].

the temporal resolution of 470 ms observes a far slower dynamics than spiking activity (< 10 ms). The results are shown in Fig. 2.15.

Interestingly, in all experiments the best-fit exponents deviate from the branching process dynamics of ($\alpha = 3/2, \beta = 2, \gamma = 2$): in Friedman *et al.* they are ($\alpha = 1.7, \beta = 1.9, \gamma = 1.3$), in Kanders *et al.* they are ($\alpha = 2.18, \beta = 2.76, \gamma = 1.43$) and in Ponce-Alvarez *et al.* they are ($\alpha = 2.01, \beta = 3.01, \gamma = 1.85$).

Nevertheless, they all follow the basic scaling law of $(\beta - 1) / (\alpha - 1) = \gamma$: in Friedman *et al.* it is $(\beta - 1) / (\alpha - 1) = 1.29$, while in Kanders *et al.* it is $(\beta - 1) / (\alpha - 1) = 1.49$ and finally $(\beta - 1) / (\alpha - 1) = 1.99$ for Ponce-Alvarez *et al.*. These are compatible with the independently measured values for γ, and appear to collapse the average avalanche shape well (Figs. 2.13D, 2.14D, 2.15D). In Table 2.2 we

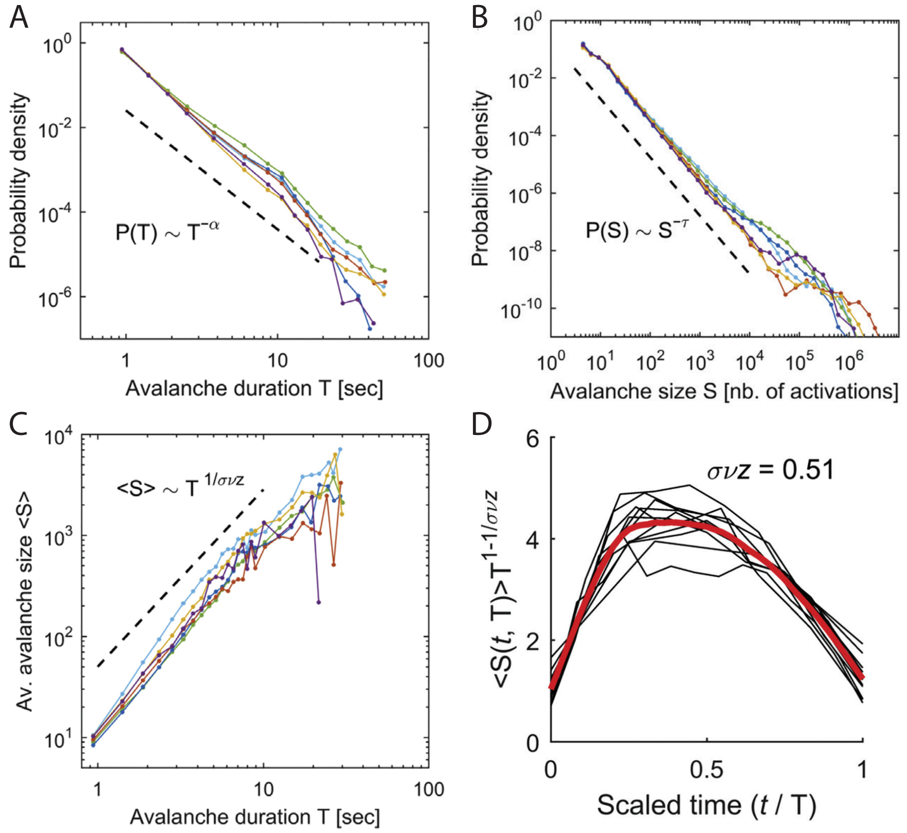

Figure 2.15: **Avalanche observables from Ponce-Alvarez *et al.* [148]. A.** Avalanche size distribution $p(S)$ from $N = 6$ zebrafish larvae, fitted to $p(S) \sim S^{-\alpha}$ with $\alpha = 2.01 \pm 0.03$. **B.** Same as A for the avalanche duration distribution $p(D)$, fitted to $p(D) \sim D^{-\beta}$ with $\beta = 3.01 \pm 0.11$. **C.** Same as A for the average avalanche size $\langle S \rangle (D)$, fitted to $\langle S \rangle \sim S^{\gamma}$ with $\gamma = 1.85 \pm 0.03$. **D.** Scaled average avalanche shape $s(t, D)/D^{\gamma - 1}$ as a function of the scaled time t/D. Adapted from [148].

summarize these exponents, and compare them to the ones from both the branching process and the (unbiased) random walk [116] process.

While a number of mechanisms can generate apparent power-laws [7, 9], the full set of scaling exponents respecting Eq. 2.40 is unlikely to be explained by dynamics without a phase transition. Thus, it constitutes strong evidence that critical-like dynamics can arise *in vitro*. While evidence that criticality can emerge in vivo begin to appear with imaging techniques [148], it still does not correspond to spreading spiking activity due to sampling rates much slower than spiking activity. Thus, to the best of our knowledge, neither long ranges of $p(S)$ nor the full set of scaling exponents have been reported for spiking activity *in vivo*.

Table 2.3: Compilation of experiments analyzing cognitive changes and how it relates to changes in the dynamical state.

authors	technique	main conclusion
Ribeiro *et al. al*, 2010 [156]	spikes	Near-critical dynamics in awake rats, anesthesia destroys temporal signatures of criticality.
Priesemann *et al.*, 2013 [137]	LFP	Subcritical dynamics in humans, increasingly close to critical in the following order: REM sleep, awakeness, slow-wave sleep.
Scott *et al.*, 2014 [139]	optical imaging	Critical dynamics in awake mice, supercritical dynamics in anesthesia.
Bellay *et al.*, 2015 [141]	two-photon imaging	Near-critical dynamics in awake rats, disrupted in anesthesia.
Fagerholm *et al.*, 2015 [142]	EEG/fMRI	Near-critical dynamics in resting state of humans, subcritical dynamics during task.
Tagliazuccchi *et al.*, 2016 [157]	fMRI	Near-critical dynamics in awake humans, subcritical dynamics during unconsciousness.
Bocaccio *et al.*, 2019 [149]	fMRI	Near-critical dynamics in awake humans, supercritical-like in deep sleep.
Ezaki *et al.*, 2020 [158]	fMRI	Higher cognitive performance in humans with brain dynamics closer to criticality.

2.5.2 *Deviations from criticality*

Regardless of the technical challenges, it is a common working hypothesis that baseline cortical dynamics is critical or near-critical. From that, many studies focused on how changes from this baseline can result in deviations from critical dynamics. Topics of research associated with possible deviations from criticality can be divided in three main groups: i) cognitive effects, ii) neurological disorders, and iii) development in vitro. In the following we discuss these three lines of research.

Most studies of cognition in vivo (in the context of criticality) are concerned with the effects of loss-of-consciousness (LOC) on brain function. In Table 2.3 we summarize a number of experiments on that. Generally speaking, it was shown that LOC results in deviations from baseline critical or near-critical dynamics. The nature of those deviations depends on the nature of the LOC: rapid eye movement (REM) sleep has been found to skew the dynamics towards a more subcritical state [137, 157], while deep sleep produced disruptions that can be interpreted as supercritical[25] [149]. Anesthesia also resulted in changes compatible with supercritical dynamics [139, 141, 156]. In terms of task performance, a smaller distance to criticality has been found to correlate with higher cognitive performance [158]. Interestingly, the distance to criticality has been observed to increase (i.e. more subcritical) during attention tasks [142].

It has been surmised that task-related changes from critical dynamics can be explained by the way which criticality maximizes variability and sensitivity (Sec. 2.4.4) [6]. While a highly variable, flexible dynamic state could be optimal in a pre-task context, it could be detrimental during focused attention. This effect has been long studied in the context of neuronal variability ("brain noise") during task and stimulus onset, in which neuronal variability is observed to decrease [159, 160].

The study of neurological disorders using the concept of criticality focus mostly on epilepsy [161–165]. As epileptic seizures are associated with synchronization issues [166], they are often modeled in terms of a transition between oscillatory and non-oscillatory activity [163–165]. This type of transition is known in dynamical systems as a *bifurcation point*.

Seizures have also been modeled in terms of the quiescent-active transition of the branching process. In that picture, seizures are associated with supercritical dynamics, as its activity-amplifying properties can be considered a source of instability. Despite its appeal, evidence that seizures are related to supercritical dynamics is conflicting. It has been shown that seizures are accompanied by an excess in larger avalanches of activity [161], and that anti-epileptic drugs induce subcritical dynamics [167]. However, no link between seizure onset and supercritical dynamics has been observed [168–170] (see Fig. 2.16B).

This lack of evidence that supercritical dynamics is implied in epilepsy may be due to the inherent variability of near-critical dynamics. We can see this in the Galton-Watson BP (Sec. 2.4.1), where only for a very supercritical $m \approx 1.4$ an avalanche is more likely than not ($P_s > 50\%$) to result in runaway activity[26]. Nevertheless, research continues into how criticality may be used in seizure prediction.

Changes to the large-scale dynamics of neuronal networks have been observed during development in vitro. In Table 2.4 we summarize some experiments exploring that. Generally, they point towards the network becoming closer to criticality as it develops [22, 101, 150, 171]. It is interesting to note that this change is sometimes not smooth — the network dynamics goes through subcritical and supercritical phases, as if the driving mechanism is correcting after undershooting/overshooting the critical point. Mechanistically, it is proposed that this happens due to plasticity rules in a form of self-organized criticality [172, 173].

---

[25] As we've seen in Sec. 2.4, a finite system cannot be simultaneously stationary and rigorously critical or supercritical. Thus, we employ "supercritical" as short-hand for a not strictly stationary process which is transiently supercritical.

[26] This is seen in Fig. 2.6B, and numerically shown by solving Eq. 2.18 for $P_s = 0.5$.

Table 2.4: Experiments analyzing development of neuronal cultures, at different days in vitro (DIV).

authors	reported dynamic state
Tetzlaff *et al.*, 2010 [101]	Subcritical ($\text{DIV} < 20$), supercritical ($\text{DIV} = 20$), subcritical ($\text{DIV} = 36$) and finally critical ($\text{DIV} = 58$).
Pu *et al.*, 2013 [171]	Subcritical, then critical/supercritical ($\hat{m} \approx 1.2$) during $30-80\%$ of culture lifetime (up to $\text{DIV} = 147$).
Levina *et al.*, 2017 [22]	Subcritical ($\text{DIV} < 21$) then critical ($\text{DIV} = 21$ and $\text{DIV} = 34$).
Kanders *et al.*, 2020 [150]	Subcritical ($\text{DIV} \leq 9$), then critical ($\text{DIV} = 10$ and $\text{DIV} = 11$) then supercritical ($\text{DIV} = 13$).

It is important to note that this evidence comes mostly from neuronal cultures. Interpreting and extrapolating results from cultures requires care, as i) cultures start dissociated, so activity is always uncorrelated in the beginning and ii) cultures die after at most a few months, so eventually the dynamics degrade due to that effect (it e.g. stops being critical). More importantly, it is unclear how much can be generalized from cultures to living brains, due to differences in structure and stimulation[27] It is also important to note that not all cultures develop towards a critical state. For instance, Pu *et al.* [171] report non-critical behavior in 6 out of 23 culture samples, while Pasquale *et al.* [174] and Friedman *et al.* [134] report different culture samples developing towards different points in the subcritical-supercritical range.

This variability can be due to a number of variables that are difficult to control in experiments, such as variability in network topology and spike rate. Changes in the topology may lead to different types of dynamics [147], while it was shown that spike rate homeostasis can drive branching networks towards varying levels of subcritical dynamics depending on the target rate [173]. Moreover, neurons die as the culture develops, and the neuronal density in mature cultures vary over a wide range of $10 - 10^3$ neurons/mm^2 [175, 176].

2.5.3 *Reverberating dynamics in vivo*

All in all, the studies mentioned in Sec. 2.5.1 and Sec. 2.5.2 suggest that i) near-critical dynamics is a good fit to baseline neuronal activity, and ii) changes from this baseline can be characterized within the framework of critical processes.

Nevertheless, we've shown that experimental evidence of criticality comes with a number of technical caveats, mostly derived from experimental constraints.

---

[27] Most cultures are not stimulated apart from being placed in a medium that induces spiking activity. Even in those that are, it is challenging to design a stimulation protocol generating input statistics resembling those of *in vivo*.

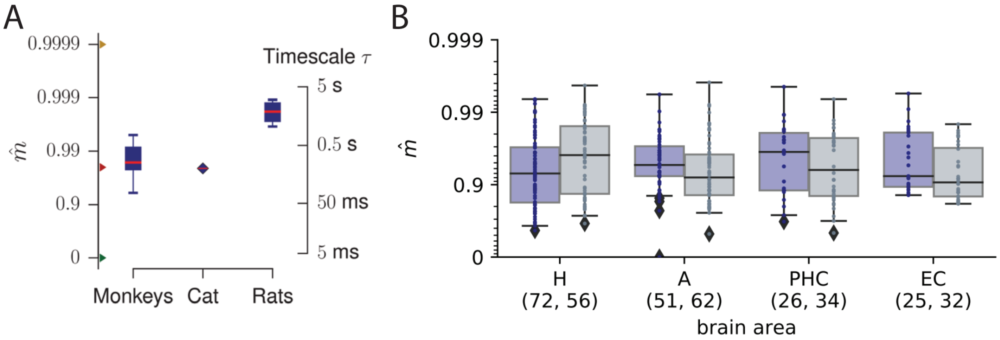

Figure 2.16: **Experimental evidence of reverberating dynamics. A.** Estimated branching parameter $\hat{m}$ of monkeys (prefrontal cortex), cats (visual cortex) and rats (hippocampus). Adapted from [177]. **B.** Estimated branching parameter $\hat{m}$ of human patients with epilepsy, for the epileptic region (purple) and non-epileptic hemisphere (gray). Brain areas are the hippocampus (H), amygdala (A), parahippocampal cortex (PHC) and entorhinal cortex (EC). Adapted from [170].

In many situations, these caveats inhibit a more precise classification of the dynamics beyond "near-critical". For example, the short power-laws usually obtained from analysis of neuronal avalanches make it difficult to distinguish sub-, super- and critical dynamics (see Fig. 2.9A-C). This is significant, as we've established that functional properties (such as sensitivity to input) vary dramatically near criticality.

Importantly, *subsampling* of spiking activity hinders precise classification of the dynamics at the neuronal level. By failing to fully observe the system not only activity is lost, but it gets less correlated both in space and time. As a result, measures such as the autocorrelation function $C(t)$ are biased towards lower values, and smaller avalanches are observed.

Recently, mathematical tools have been developed to correct for this subsampling bias. In terms of neuronal avalanches, Levina & Priesemann [22] demonstrated how to scale the subsampled avalanche size distribution and recover the true avalanche size distribution. Importantly, Wilting & Priesemann [178] developed a method to obtain the true branching parameter even under heavy subsampling. Using this method, they found that baseline in vivo spiking activity operates consistently in a slightly subcritical, driven regime. This result was consistent across species (monkey, rat, cat, human) and brain regions [170, 177, 178] (see Fig. 2.16). It supports (and quantifies) earlier results from neuronal avalanches of spikes [179]. Such regime is on average 2% off criticality ($\bar{m} \approx 0.98$), and is called **reverberating**.

We argue [100] that this reverberating regime is an ideal baseline from which activity can flexibly adapt to task requirements. It maintains a safe distance from critical instability while still drawing from interesting properties of the critical

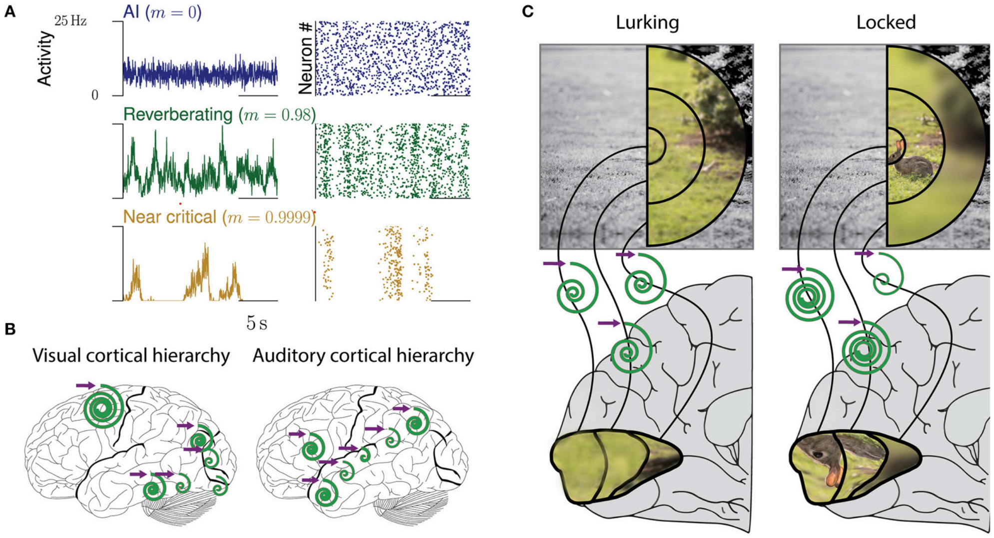

Figure 2.17: **Reverberating dynamics in vivo.** **A**. Example timeseries of activity with Poissonian ($m = 0$), Reverberating ($m = 0.98$) and near-critical ($m = 0.9999$) dynamics. **B**. Hierarchical representation of the visual and auditory systems. As input moves up the hierarchy, timescales increase. **C**. Representation of a tuning mechanism from a baseline reverberating dynamics: if a predator sees a prey, relevant areas are tuned in (increased timescales), while non-relevant areas are tuned out. Reproduced from [100].

state. For instance, it results in an autocorrelation time of $\tau = -\delta t/\ln(0.98) \approx 200$ ms, where we use $\delta t = 4$ ms as the timescale of spiking activity. In this regime, a 1% increase in m doubles τ, while a 1% decrease results in a 33% decrease in τ. In terms of sensitivity to input (Eq. 2.43), the 1% increase doubles the sensitivity, while the 1% decrease cuts it in half. As $m \to 1$ this change becomes more extreme, but it incurs into a higher risk of runaway activity, and of dynamics becoming dominated by fluctuations in e.g. synaptic strength [180].

Thus, being in the reverberating regime could offer a way for neuronal activity to quickly tune in or tune out external input, depending on requirements. We illustrate this in Fig. 2.17C, where such a mechanism could be used to dynamically amplify important input (e.g. visual input with prey), and suppress non-relevant ones.

3

SAMPLING BIAS

In this chapter we explore how sampling bias can affect dynamics on a number of different systems. All the results shown here can be considered new. We first introduce the concept, and demonstrate how sampling bias can affect the observables of the branching process. We then show how imperfect sampling can bias the coarse graining of the Ising model, introducing spurious correlations. Lastly, we demonstrate how sampling bias combined with frequency filtering can produce the variability in neuronal spectra observed in experiments. We find the signature of those mechanisms in a large number of datasets. This result suggest that sampling of neuronal activity using electrodes is better in vivo than in vitro.

3.1 WHAT IS SAMPLING BIAS?

In statistical inference, sampling refers to the process of estimating characteristics of a population (system) by selecting a subset of individuals (samples) [181]. Usually, statistical inference operates under the assumption that samples are independent and identically-distributed (i.i.d) random variables with finite variance. Under this assumption, the central limit theorem guarantees that the mean of the sampled characteristic converges to the true mean of the distribution and that the sampled distribution is Gaussian. Furthermore, the Berry-Essen theorem states that the convergence rate is $\sim n^{-1/2}$, with n being the number of samples.

When the assumption of i.i.d. random variables fails, it cannot be assumed that sampled characteristics converge monotonically (or quickly) to their true values[1]. It can result in erroneous values for the incompletely-sampled characteristics of the population, which we call **sampling bias**. Generally, sampling bias is an important issue in any field where sampling is incomplete. For instance, in population statistics one of the main goals is how to avoid bias in population surveys (e.g. election polls) [182]. Sampling also affects the perceived structure of networks. For instance, undersampled scale-free[2] networks are not scale-free [184].

When considering dynamical systems, in particular, samples are generally not i.i.d. Since a dynamical system evolves in time modeled by a set of (deterministic or probabilistic) equations, samples are usually correlated in time. Thus observ-

---

[1] It also means that standard statistical tests like the t-test and ANOVA do not apply anymore.

[2] A scale-free network is one where the degree distribution follows a power-law $p_k \sim k^{-\alpha}$. Scale-free properties have been observed in many real-world networks [183].

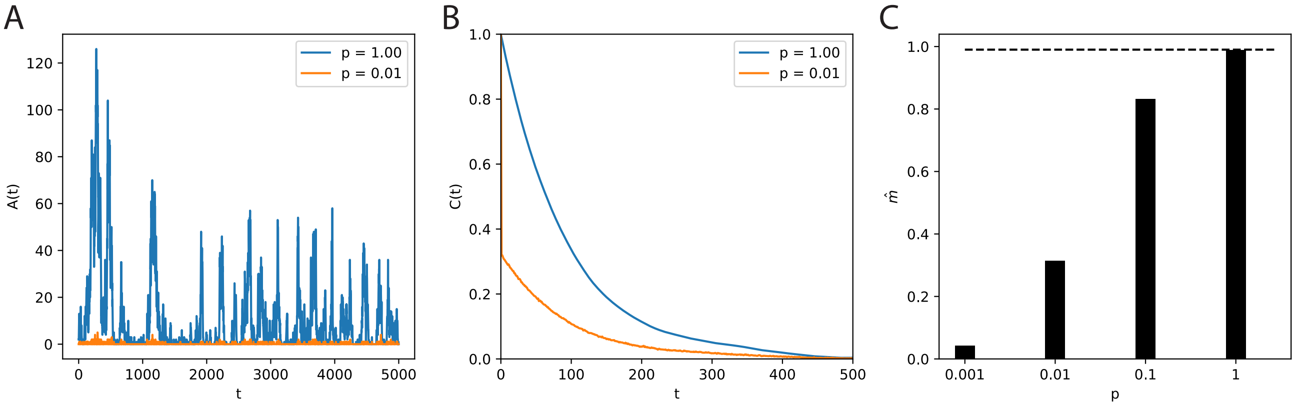

Figure 3.1: **Effects of subsampling on a branching process with $m = 0.99$. A.** Activity timeseries $A(t)$ of the BP with sampling probability $p = 1$ (blue) and $p = 0.01$ (orange). **B.** Autocorrelation function $C(t)$ of the timeseries of A. **C.** Estimation of the branching parameter $\hat{m}$ by fitting $A(t+1) = \hat{m}A(t) + h$, for varying levels of p.

ables of the system must be either i) invariant under sampling[3] or ii) explicitly corrected for it.

To exemplify the effects of sampling in a dynamical system, lets consider the branching process defined in Sec. 2.4. For a BP with branching parameter $m = 0.99$ (close to criticality), lets assume that each event is observed with probability p. As we can see in Fig. 3.1A, the activity timeseries $A(t)$ when sampling 1% of the events ($p = 0.01$) can look dramatically different from the fully-sampled one ($p = 1$). More importantly, failing to observe events decorrelates activity, which leads to sampling bias in observables of collective dynamics. We observe this in Fig. 3.1B, where sampling 1% of the events results in an offset in the autocorrelation function $C(t)$. In Fig. 3.1C we see the subsampled-induced bias in the estimation of the branching parameter $\hat{m}$, obtained by fitting $A(t+1) = \hat{m}A(t) + h$. While the fully-sampled dynamics ($p = 1$) recovers the correct value, sampling 1% of the events results in $\hat{m} \approx 0.3$. From Eq. 2.34, this means we underestimate the true autocorrelation time τ of the dynamics by a factor of 100.

In the case of (biological) neuronal dynamics, biasing τ by such an amount would make it indistinguishable from zero. Thus, the near-critical dynamics of the $m = 0.99$ branching process would be erroneously classified as uncorrelated. This ties into what has been called the "dark matter" problem of neuronal activity: neurons can spike very little or only under specific input, and thus not show in typical recordings [185]. Similar to the subsampling of the branching

---

[3] An example of an invariant observable is the one developed in [178] to obtain an unbiased estimate of the branching parameter m.

dynamics, the existence of these silent neurons could bias our understanding how activity propagates in the brain.

3.2 SAMPLING BIAS IN THE ISING MODEL

3.2.1 *Coarse graining*

The 2D Ising model (discussed in Sec. 2.3.2) is often used to exemplify how a system can be sampled while keeping its main properties. This is done through a renormalization group (Sec. 2.3.1) transform, also known as *coarse graining* of the Ising model [55]. In this framework, the system is rescaled by merging multiple spins into one. This new coarse-grained system, made of rescaled "superspins", offers a larger scale view on the dynamics[4].

The actual process of coarse graining the Ising model can be done in a number of ways. The most common one is known as the real-space[5] blockspin transform with a majority rule. In that, blocks of $b \times b$ spins are grouped into a single spin, with sign ($+1$ or -1) equal to the majority value within the group. We exemplify this in Fig. 3.2.

Importantly, the coarse-grained system *is not* identical to the underlying system — for one, it is subject to finite-size effects and thus its observables are numerically different. As mentioned in Sec. 2.3.1, only at criticality the observables of the Ising model are invariant under coarse-graining.

In order to study the coarse graining of the Ising model, we perform Monte Carlo simulations of the 2D Ising model using the massively parallel multicanonical method [186, 187][6]. The multicanonical method offers numerous advantages over conventional Monte Carlo approaches. For instance, instead of simulating at a single temperature, one simulation covers the whole energy space. High-precision canonical expectation values of observables are recovered for any desired temperature during a post-production step.

In Fig. 3.2B we observe the effects of coarse graining on the normalized absolute magnetization $m(T) = \frac{1}{N}|\sum_i s_i|$. Only at the critical point $T = T_C$ we find an invariant $m(T)$ — for $T < T_c$, m is increased, while for $T > T_c$, m is decreased.

An alternative rule for coarse graining the Ising model is known as the *decimation rule*. In that, instead of using the majority of spins within the block, a random spin is chosen to represent the block.

If instead of the majority rule the decimation rule is used, the blocking procedure does not alter the correlation between spins before and after the transformation (Fig. 3.2C). As a consequence, the magnetization remains unaltered in general. However, in the disordered phase, we still notice a systematic deviation from the unblocked system (with $L = 64$). This deviation can be fully attributed

---

[4] This is related to the concepts of *spatial sampling* and *cluster sampling* in statistics [181].

[5] For other systems, renormalization is often done in momentum space.

[6] Results in this section were produced in conjunction with F. P. Spitzner.

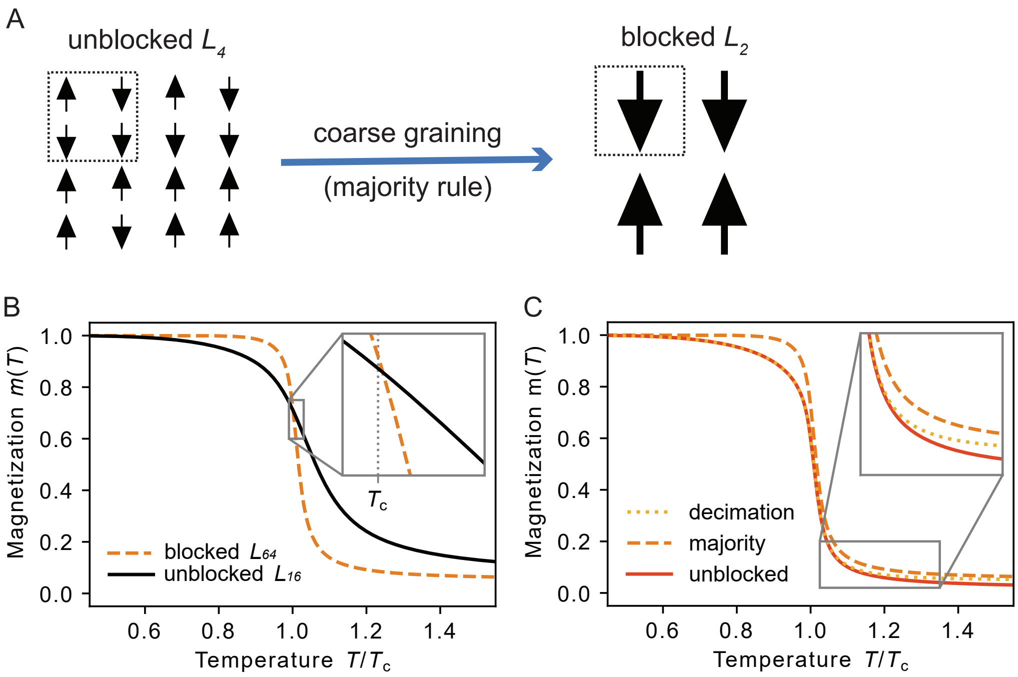

Figure 3.2: **Coarse graining the Ising model. A.** Representation of the coarse graining where a 4×4 (L_4) system gets rescaled to a 2×2 system with a majority rule and block size $b = 2$. **B.** Effect of coarse graining on the average magnetization $m(T)$ with block size $b = 4$. Since the system is rescaled by a factor of $1/b^2$, the blocked system with size L_{64} needs to be compared to an unblocked system with size L_{16}. Only for $T = T_C$ we find an invariant $m(T)$ under coarse graining. **C.** Comparison between the fully-sampled, unblocked system and blocked systems using the majority rule and the decimation rule for $b = 4$. All simulations and curves for $L = 64$. In the ordered, low-temperature phase, the sub curve matches the fully sampled system. Only for the high-temperature phase deviations occur due to finite-size effects (the magnetization for $T \to \infty$ approaches the value expected for the rescaled $L = 16$ system). The coarse curve is systematically biased towards more ordered states.

to finite-size effects: The distribution of realizable magnetizations in the disordered phase follows a Gaussian with mean zero and variance proportional to the (effective) number of spins. Due to the definition of the magnetization with absolute value, the expectation value of the magnetization for $T \to \infty$ is determined by the (effective) system size. Note that the impact of different block-transformation rules on $m(T)$ will not hold for all other canonical observables such as the energy $E(T)$ [55].

Here we used the coarse graining of the Ising model to demonstrate two important concepts: i) only at criticality the observables are preserved under rescaling and ii) the details of the rescaling procedure can impact how it biases the observables away from criticality.

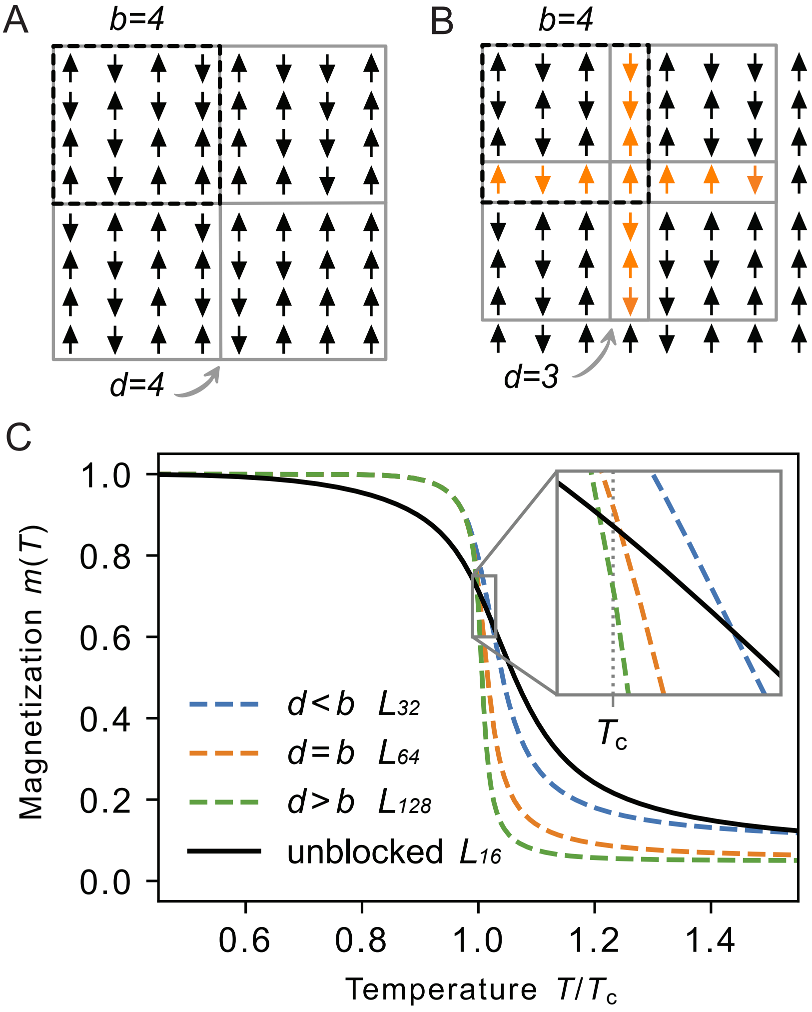

Figure 3.3: **Coarse graining the Ising model. A.** Representation of the standard coarse graining where block size matches the distance between blocks ($d = b = 4$). No overlap is created. **B.** Coarse graining with block size $b = 4$ and a distance between blocks of $d = 3$. Overlapping spins (orange) are shared by two or more blocks. **C.** With the majority rule, overlap impacts the spontaneous magnetization $m(T)$. Only the crossing between the unblocked ($L = 16$) and non-overlapping blocked system ($d = b$, $L = 64$) happens at $T = T_C$, as would be expected. Intriguingly, the overlap ($d < b$, $L = 32$) pushes the system towards higher magnetization where spins appear more aligned. On the other hand, the absence of overlap ($d > b$, $L = 128$) causes smaller magnetization where spins appear more random.

3.2.2 *Overlapping blocks induces bias*

To show how sampling bias can affect the measured observables, we now introduce an overlap between the blocks of the Ising model coarse graining (Fig. 3.3).

In the native block-spin transformation, blocks do not overlap. Then, in terms of spins, the linear distance d between two blocks matches the block size $b = d = 4$ (Fig. 3.3A). When the distance between blocks is smaller than the block size, $d < b$ (Fig. 3.3B), measurement overlap is created, while when $d > b$ parts of the system are not sampled.

Here we look at combinations of block size $b = 4$ with distance between blocks of $d = 2$, $d = 4$ and $d = 8$. In order to preserve the effective system size ($L = 16$), we thus perform simulations for $L = 32$, $L = 64$ and $L = 128$, respectively.

We find that, for increasing overlap ($d < b$), the crossing occurs at $T > T_c$ (Fig. 3.3C). This is because sharing spins increases the correlations between blocks (pairwise and higher-order), making it more likely that the rescaled spins point into the same direction. In other words, it biases the measurement of m towards order, increasing our estimated critical temperature.

For absent overlap ($d > b$), only every other block is measured. This decorrelates the spins near the borders of each block and, therefore, decreases the correlation between blocks. As a consequence, the spin orientation of the blocked system moves towards disorder, decreasing the measured magnetization m.

In conclusion, we find that overlapping blocks in the Ising model coarse graining can induce spurious correlations and bias the magnetization $m(T)$. This can lead a subcritical system ($T < T_C$) to be considered critical due to apparent invariance of $m(T)$. This overlapping will be a key mechanism in Chapter 4, where we show that it can heavily bias measurements of criticality in neuronal avalanches.

3.3 SAMPLING BIAS AND $1/f$ NOISE

3.3.1 *What is $1/f$ noise?*

The phenomena of $1/f$ noise is ubiquitous in nature [188–190]. It refers to the tendency of the **power spectral density** of various systems to scale with frequency f as a power-law

$$PSD(f) \sim 1/f^{\beta} \tag{3.1}$$

with an exponent[7] $\beta > 0$. It was first observed in electric circuits, and subsequently in many diverse phenomena ranging from earthquakes [191] to stock market fluctuations [192] to heartbeat rhythms [193] to gravitational waves [194].

Mathematically, the power spectral density (PSD) of a timeseries $A(t)$ is defined[8] as

$$PSD(f) = |\hat{A}(f)|^2 \tag{3.2}$$

---

[7] While the term "$1/f$ noise" sometimes refers to $PSD \sim 1/f^{\beta}$ with $\beta = 1$ (also known as pink noise), here we use it in the broader sense to describe any $\beta > 0$.

[8] For this definition to be valid, $A(t)$ must be both stationary and square-integrable.

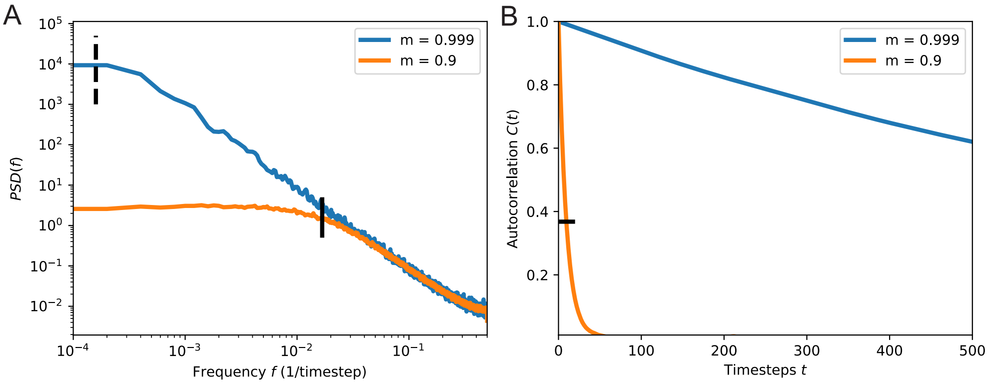

Figure 3.4: **Power spectral density (PSD) and autocorrelation of branching processes.** **A.** PSD of branching processes with $m \in [0.9, 0.999]$. The vertical lines correspond to the cut-off frequency $f_0 = -\log m/2\pi$ for both m (traced line for $m = 0.999$, solid line for $m = 0.9$). **B.** Autocorrelation function $C(t)$ for the same branching processes as A. Horizontal line corresponds to $C(t) = 1/e$. Simulation data from branching processes with drive with average activity $A_\infty = 50$ and 10^6 timesteps.

where $\hat{A}(f) = \int_{-\infty}^{\infty} e^{-2\pi i f t} A(t) dt$ is the Fourier transform of $A(t)$. For a sampled (discrete) timeseries A_n with sampling resolution δt , the PSD is given by

$$PSD(f) = \delta t^2 \left| \sum_{n=-\infty}^{\infty} e^{-2\pi i f n \delta t} A_n \right|^2 \tag{3.3}$$

Being discrete, $PSD(f)$ has a maximum frequency given by the Nyquist frequency $f_{max} = 1/2\delta t$.

The PSD is also linked to the autocorrelation function (see Sec. 2.2.1) by the Wiener–Khinchin theorem. It states that the autocorrelation function of a stationary process has a spectral decomposition given by the PSD of the process. For a discrete timeseries with an autocorrelation function $C(t)$ we have

$$PSD(f) = \left| \sum_{t=0}^{\infty} C(t) e^{-i(2\pi f)t} \right|^2 \tag{3.4}$$

Thus, in theory the PSD and the autocorrelation function represent the same information in real and frequency spaces. In practice, however, depending on the situation on or the other may be better-suited to study a system.

To show that, and for what follows afterwards, lets obtain the spectrum of the branching process (BP) with drive (Sec. 2.4.2). For a BP with branching parameter m, the autocorrelation function[9] is

$$C(t) = e^{-t\delta t/\tau} \tag{3.5}$$

---

[9] It differs from the $C(t)$ derived in Sec. 2.4.4 in that here we separate the (now unitless) number of steps from its temporal resolution, i.e. $t \to t\delta t$.

where $\tau = -1/\log m$ is the autocorrelation time of the process. If we approximate the sum by an integral (making $\delta t \to 0$), from Eq. 3.4 we have:

$$\begin{aligned} PSD(f) &= \left| \sum_{t=0}^{\infty} e^{-t\delta t/\tau} e^{-i(2\pi f)t} \right|^2 \approx \left| \int_0^{\infty} e^{-t/\tau} e^{-i(2\pi f)t} \mathrm{d}t \right|^2 \\ &\approx \left| \frac{1}{2\pi i f + 1/\tau} \right|^2 = \frac{1}{f^2 + 1/4\pi^2\tau^2} \end{aligned} \tag{3.6}$$

If we define the *cut-off frequency* $f_0 \equiv 1/2\pi\tau = -\log m/(2\pi)$ we then have:

$$PSD(f) \approx \frac{1}{f^2 + f_0^2} \tag{3.7}$$

Thus, the PSD of a driven BP is a Lorenzian function. As $m \to 1, f_0 \to 0$ and $PSD(f) \sim 1/f^2$. In the limit $m \to 0$ we find that f_0 dominates and the PSD is flat. We show the PSD for varying m in Fig. 3.4A, and the respective $C(t)$ in Fig. 3.4B.

Lets suppose we are interested in using these measures to obtain the autocorrelation time τ. With the PSD, we can obtain m by fitting Eq. 3.7 to the data, from which we obtain an estimate $\hat{\tau} = 1/2\pi\hat{f}_0$. However, if we propagate the fitting error Δf_0 of $\hat{f}_0$ to τ, we find that $\Delta\tau \sim \Delta f_0/\hat{f}_0^2$. Since $f_0 \to 0$ as $m \to 1$, using the PSD to obtain τ is increasingly worse as the system gets closer to criticality.

Estimating τ from the autocorrelation function $C(t)$, on the other hand, suffer from the reverse effect: due to limited data, there is a minimum value below which $C(t)$ is dominated by noise. This translates into a maximum number of timesteps that can be used in the fitting of $C(t)$. In Fig. 3.4B we see that $C(t)$ of the system close to critical ($m = 0.999$) can be reliably fitted on a range of thousands of timesteps, while for the subcritical one ($m = 0.9$) this range is much shorter. This can be quantified by noting that τ corresponds to the number of timesteps it takes for the signal to decay to $C = 1/e \approx 0.37$, which are $\sim 10^3$ timesteps for $m = 0.999$ and ~ 10 timesteps for $m = 0.9$. Thus, using $C(t)$ to obtain τ is increasingly worse as the system gets further to criticality.

In summary, both the PSD and autocorrelation function $C(t)$ can be used to estimate τ: the autocorrelation function $C(t)$ is more accurate closer to criticality, while the PSD is better for more subcritical systems.

3.3.2 *$1/f$ noise in neuronal recordings*

The study of neuronal activity using spectral analysis has been a big part of neuroscience since the invention of the electrocardiogram (EEG) around a century ago. For decades, most of the research focused on the study and characterization of neural oscillations, which are oscillatory patterns of neuronal activity.

Neural oscillations are divided in frequency bands, and have been linked to a large array of physiological and cognitive mechanisms. For instance, activity

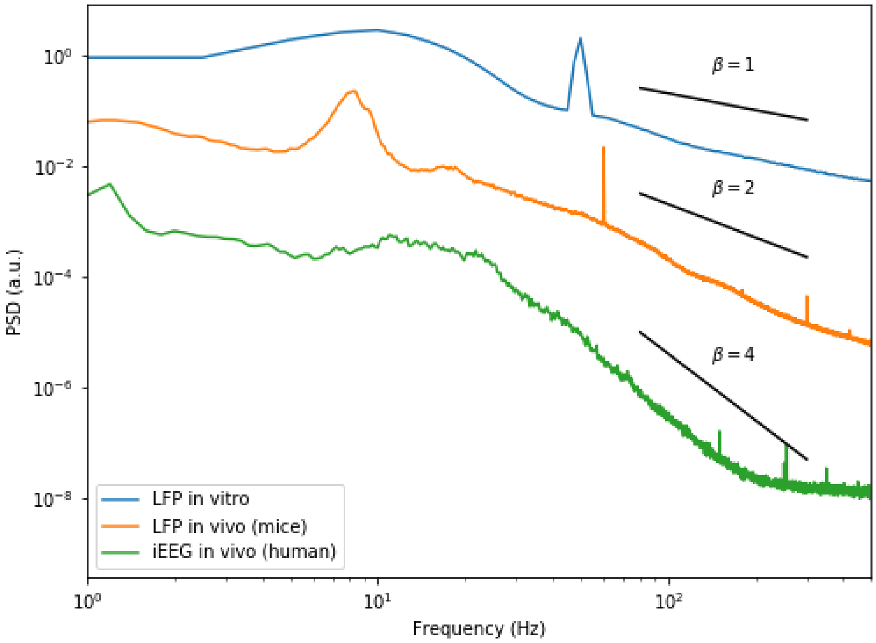

Figure 3.5: **Power spectral density from electrode measurements of neuronal activity.** PSD of Local Field Potential (LFP) measures in vitro from neuronal cultures (blue), LFP in vivo from mice (orange) and intra-cranial Electroencephalography (iEEG) in vivo from humans (green).

in the theta band $(6-10$ Hz) is linked to memory function in the hippocampus, while an excess of activity in the delta band $(0.5-2$ Hz) defines slow-wave (deep) sleep. These oscillations occur on top of an aperiodic, background "noise" signal whose amplitude decays with increasing frequency. This background signal is an example of $1/f$ noise, and recently its origin has become a major topic of study.

In neuroscience, $1/f$ noise has been observed in measurements of neuronal activity using a vast range of techniques, such as EEG, MEG, LFP, ECoG and fMRI. Crucially, the measured exponent β has been observed to vary in a large range $0 < \beta < 4$ (see Fig. 3.5). Many mechanisms have recently been proposed to explain this variability in β: changes in the firing rate [195], varying excitatory-inhibitory (E-I) balance [196–198], aging [199] and frequency filtering [8, 200–202].

The role each of those mechanisms play in various measurements of neuronal activity is still an open question. In particular, much has been debated whether measurements of neuronal activity are subject to a low-pass frequency filter. Local measurements such as the LFP and ECoG are believed to be affected by den-

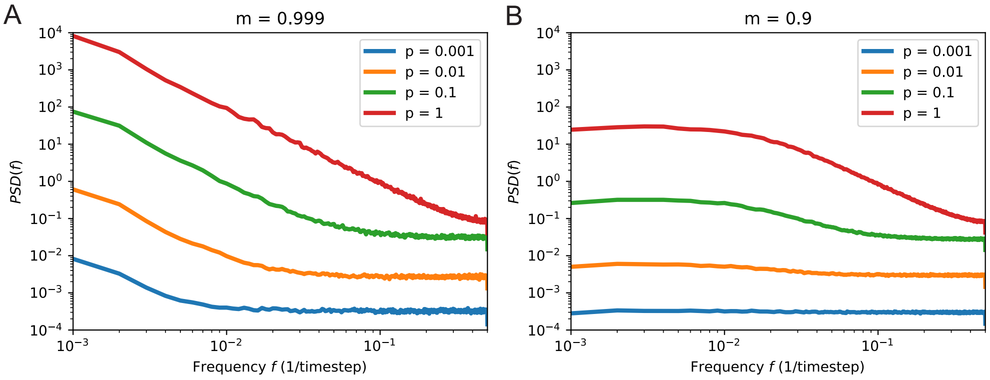

Figure 3.6: **Power spectral density of subsampled branching processes. A.** PSD of a BP with $m = 0.999$ (close to critical) where events are observed with probability $10^{-3} \leq p \leq 1$. **B.** Same as A for a BP with $m = 0.9$ (subcritical). Subsampling convolves the (Lorentzian) spectrum of the BP with the flat spectrum of an uncorrelated process.

dritic filtering, caused by the intrinsic neuronal morphology [151, 203, 204]. More controversially [205], filtering could also come from capacitive properties of the extracellular tissue [8, 201, 202, 206].

In the following we propose a new mechanism based on sampling bias, and show that it can explain shallow exponents $\beta < 2$. We demonstrate how, coupled with a filtering mechanism, it can explain the entire range $0 < \beta < 4$ of exponents observed experimentally.

3.3.3 *Varying exponents from sampling effects*

Lets now explore how sampling bias can affect the spectra of near-critical dynamics. We first look into the driven branching process. Like in Sec. 3.1, we consider that each event is observed (independently) with probability p. The resulting PSDs are shown in Fig. 3.6.

By decorrelating activity, subsampling mixes the spectra of the BP ($\sim 1/f^2$) with that of an uncorrelated process (flat). While for low frequencies it maintains the underlying activity spectra, for high frequencies we obtain flat spectra. The larger the subsampling (smaller p), the lower the frequency at which the spectra becomes flat. Since the spectra of a subcritical BP is flat for frequencies $f \ll f_0 = -\log m/2\pi$ (Eq. 3.7), for small p the spectra of a BP will be indistinguishable from that of an uncorrelated process. We see this in Fig. 3.6B, where the spectra is completely flat for $p < 0.01$. While subsampling can make the PSD of a BP look uncorrelated (like in in Fig. 3.1), it does not alter the exponent $\beta = 2$ of the power-law.

The electrophysiological techniques (LFP, EEG, etc) used to record neuronal spectra do not randomly subsample spikes, however. Rather, they directly or indirectly represent weighted averages of (hundreds to billions of) neurons spiking. Exactly how these techniques sample neuronal activity is a matter of active research. Many sophisticated models have been developed in order to explore how features such as neuronal morphology and firing rate influence the recorded electric potentials. [204, 207, 208].

As a baseline, these techniques record electric potentials from extracellular synaptic currents of firing neurons [151, 203, 209]. From classic eletromagnetism, the electric potential $V(\mathbf{r})$ generated by an arbitrary (static) charge distribution measured at a point $\mathbf{r}$ has a multipole expansion:

$$V(\mathbf{r}) = \frac{1}{4\pi\epsilon} \sum_{l=0}^{\infty} \frac{A_l(\mathbf{r})}{R^{l+1}} \tag{3.8}$$

where $A_l(\mathbf{r})$ incorporates the effects of the charge distribution, ϵ is the permittivity of the medium and $R = |\mathbf{r}|$ is the distance from the charge distribution. In the case of a single point charge Q we find that only the first term $l = 0$ is non-zero, resulting in a potential V_{mono} known as an electric monopole:

$$V_{\text{mono}} = \frac{1}{4\pi\epsilon} \frac{Q}{R} \tag{3.9}$$

In the case of two opposite charges $+Q$ and $-Q$ separated by a distance d, in the limit $R \gg d$ we have

$$V_{\text{dip}} = \frac{1}{4\pi\epsilon} \frac{Qd\cos\theta}{R^2} \tag{3.10}$$

where θ is the angle from the line formed by the two charges and the point where V_{dip} is measured. This potential V_{dip} is known as an electric dipole.

While synaptic currents can certainly generate electric potentials more complicated than monopoles and dipoles, these are considered the two most important contributors [151, 203]. In particular, the electric potential generated by single pyramidal neurons can be modeled as a dipole (see Fig. 3.7 for representations of a monopole, dipole and pyramidal neuron). As we can see in Eqs. 3.9 and 3.10, the main difference between monopoles and dipoles is that the potential of the monopole decays as $\sim 1/R$, while with the dipole it is $\sim 1/R^2$. This implies a sampling effect: the resulting electric potential from neuronal activity can be sampled by an electrode from much further away if it is more similar to a monopole than a dipole.

We decide to model this non-random local sampling with a virtual electrode that samples its surrounding. The surrounding is made of a 2D arrangement of $N = 10^4$ randomly-placed point neurons connected each to the $K = 10^3$ nearest neighbors. The dynamics is is given by a driven branching process, and spreads locally [10]. We parametrize the effective signal of a spiking neuron by considering

---

[10] More precisely, the probability of activation by a neighbor decreases with distance with a Gaussian distribution. This model is used in Chapter 4 to study neuronal avalanches. For an extensive description of its details please check Sec. 4.2.

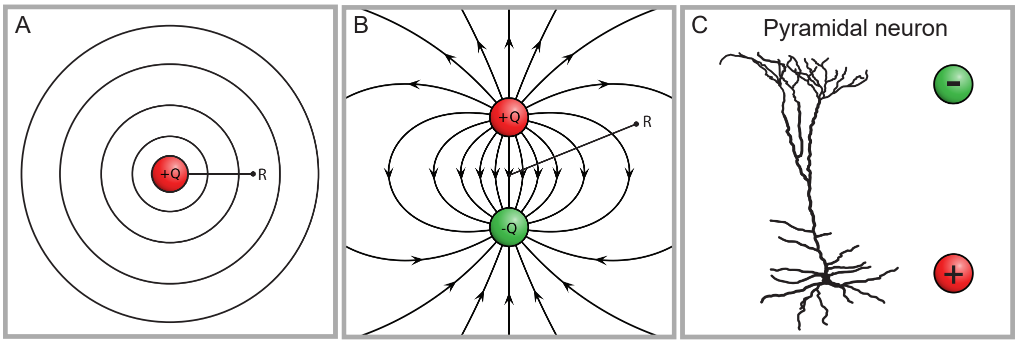

Figure 3.7: **Representation of electric potentials. A.** Representation of an electric monopole, caused by a single charge $+Q$. **B.** Representation of an electric dipole, caused by a positive charge $+Q$ (a source) and a negative charge $-Q$ (a sink). **C.** Illustration of the dendritic tree of a pyramidal neuron. The apical tree (top) is negatively charged, while the cell body (bottom) is positively charged. As a first approximation, it can be modeled as a dipole.

that it decays with distance R from the neuron as $\sim 1/R^\gamma$ with $\gamma > 0$. Thus, $\gamma = 1$ corresponds to a monopole, while $\gamma = 2$ is a dipole. Mathematically, the signal V_{elec} measured at our virtual electrode is given by

$$V_{\text{elec}}(t) = \sum_{i=0}^{N} \frac{A_i(t)}{R_i^\gamma} \tag{3.11}$$

where $A_i(t)$ is the activity state (0 or 1) of neuron i situated at a distance R_i from the electrode.

The resulting PSD from this sampling scheme is shown in Fig. 3.8. We find that, contrary to simple subsampling, this spatial (coarse) sampling decreases the exponent of $PSD \sim 1/f^\beta$ while maintaining the power-law shape[11]. The larger γ is, the more local the sampling and the flatter the spectra (smaller β). Thus, simple sampling effects could explain flatter exponents $\beta < 2$ in neuronal recordings. Importantly, it would imply that electrophysiological recordings with $\beta < 2$ (such as LFP in vitro of Fig. 3.5) are the result of poor sampling of the underlying activity.

In order to explain heavier exponents $\beta > 2$ we must introduce another mechanism. As mentioned in Sec. 3.3.1, extracellular techniques are subject to attenuating effects caused by brain tissue (in intra-cranial measurements) and bone (in EEG). These effects may block higher frequencies, generating a low-pass frequency filter that effectively introduces spurious correlations in the measured signal [8, 201, 202, 206]. We model this using a *power-law shot noise* frequency filter [200, 210]. With this filter, the signal generated from an activation at time

---

[11] The flat spectra observed as f approaches the highest frequency (0.5 in units of 1/timestep, which is the Nyquist frequency) is due to aliasing effects and can be considered an artifact of the PSD estimation.

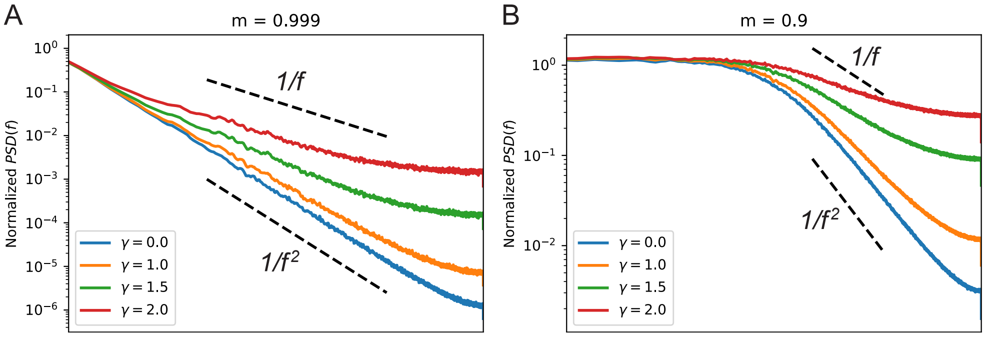

Figure 3.8: **Power spectral density of a virtual electrode with a $1/R^\gamma$ field of view. A.** PSD of a BP with $m = 0.999$ (close to critical) where events are observed a virtual electrode whose field of view decreases with distance R as $1/R^\gamma$. **B.** Same as A for a BP with $m = 0.9$ (subcritical). The underlying dynamics is made of of $N = 10^4$ units each connected to the nearest $K = 10^3$ neighbours in a 2D space with distance-dependent weights. The flat spectra for high frequencies f is the result of aliasing effects.

t_i does not decay instantly (a delta peak), but instead decays with a power-law. The activity at time $t > t_i$ from this single activation is given by

$$F(t, t_i) = (t - t_i)^{1-\gamma_f/2} \tag{3.12}$$

where $\gamma_f \in (0, 2)$ is the *shot noise exponent*. It can be shown [210] that if the activity is uncorrelated (i.e. t_i are drawn from a Poisson distribution) then the process defined by Eq. 3.12 results in $1/f$ noise with exponent γ_f: $PSD \sim 1/f^{\gamma_f}$. Note that in the limit $\gamma_f \to 2$ we have $F(t, t_i) \to 1$, and activity from the single spike never decays. Thus, this process can only generate exponents $\gamma_f < 2$.

By combining the power-law shot noise filter with the branching dynamics, we can generate heavier PSD exponents $2 \leq \beta < 4$. This is due to the convolution theorem: It states that, for two functions f and g, the Fourier transform $\mathscr{F}$ of the convolution $f \star g$ is given by the product of the Fourier transforms of f and g:

$$\mathscr{F}[f \star g] = \mathscr{F}[f]\mathscr{F}[g] \tag{3.13}$$

Since the PSD is the squared magnitude of the Fourier transform, it means that convolving the underlying branching process with the power-law shot noise process multiplies their PSDs: the subsampled activity can be interpreted as the convolution of a correlated process (the dynamics) with an uncorrelated one (the subsampling). From Eq. 3.7 we then have:

$$PSD^{filt}(f) \approx \frac{1}{f^{\gamma_f}} \frac{1}{f^2 + f_0^2} \tag{3.14}$$

which results in $PSD \sim 1/f^{\gamma_f}$ for $f < f_0$ (which depends on m) and $PSD \sim 1/f^{2+\gamma_f}$ for higher frequencies. In Fig. 3.9 we show the resulting PSDs from branching processes filtered with power-law shot noise.

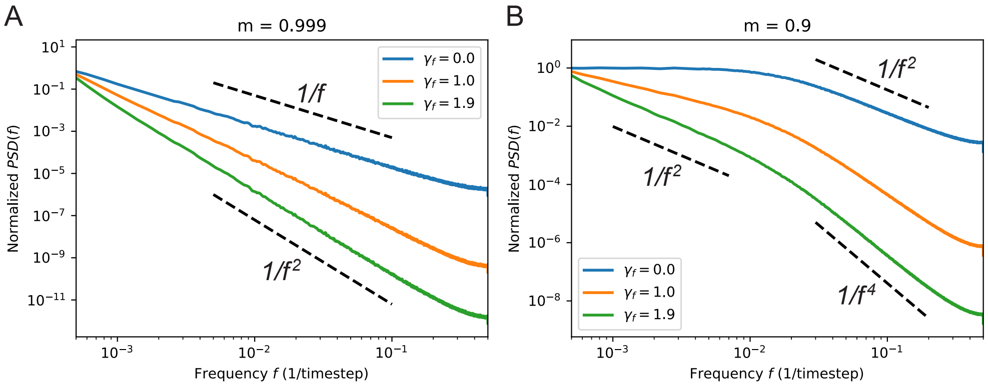

Figure 3.9: **Power spectral density filtered with power-law shot noise. A.** PSD of a BP with $m = 0.999$ (close to critical) subject to a power-law shot noise filter with exponent $\gamma_f < 2$. **B.** Same as A for a BP with $m = 0.9$ (subcritical). The underlying dynamics is made of of $N = 10^4$ units each connected to the nearest $K = 10^3$ neighbors in a 2D space with distance-dependent weights. The flat spectra for high frequencies f is the result of aliasing effects.

Naturally, we can combine the $1/R^\gamma$ spatial sampling with the $1/f_f^\gamma$ frequency filtering in order to generate the entire range of $1/f^\beta$ exponents $0 < \beta < 4$. This can in principle explain any PSD of the form

$$PSD(f) \sim \frac{1}{f^{\gamma_f+\beta'} + f_0^2 f^{\gamma_f}} \tag{3.15}$$

with the constraints $0 \leq \beta' \leq 2$ and $0 \leq \gamma_f < 2$. In Fig. 3.11 we show how the measured exponent $\beta = \gamma_f + \beta'$ varies with sampling (γ) and filtering (γ_f). As mentioned above, however, many mechanisms have been proposed to generate the variability in β observed in neuronal PSDs [196, 199, 203, 211, 212]. Thus, in order to identify if a mechanism is responsible for β it is important to find its unique signatures.

The multi-step regression estimator ("MR Estimator") [213–215] can be used to obtain a subsampling-invariant estimation m_{MR} of the branching parameter m. In Fig. 3.10A we show that it is also capable of recovering m under spatial (coarse) sampling. On the other hand, the single-step estimation[12] m_1 can be heavily biased under spatial sampling. Very close to criticality ($m = 0.999$) a limited field of view ($1/R^\gamma$ with large γ) can accurately sample the dynamics, and result in $m_1 \approx m$. For subcritical ($m = 0.9$) dynamics, however, as γ increases m_1 increasingly underestimates m, similarly to the effect of subsampling (see Sec. 4.1).

Since m_{MR} is essentially invariant under our spatial sampling and m_1 is not, we can define the *amount of bias* $\Delta m \equiv m_{MR} - m_1$ as a signature of the sampling

---

[12] Obtained here by fitting the autocorrelation $C(t)$ to Eq. 2.33.

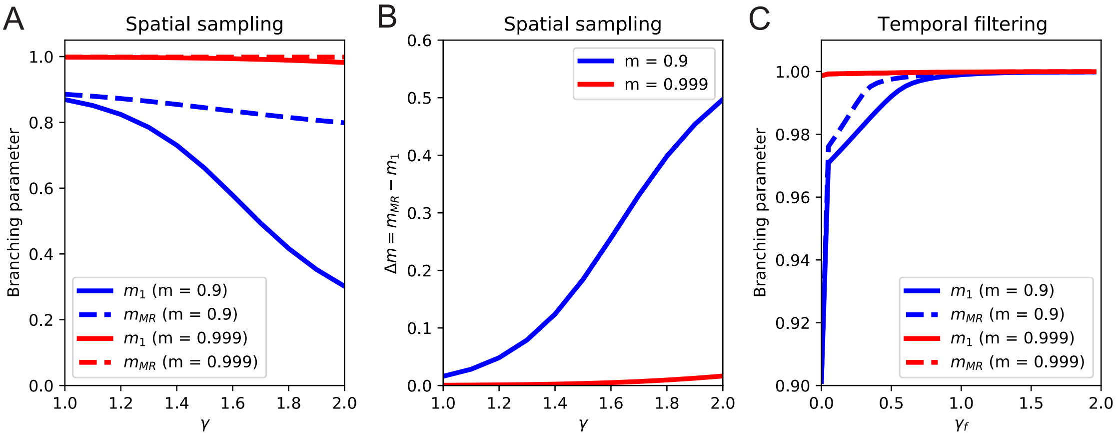

Figure 3.10: **Branching parameter under spatial (coarse) sampling and temporal filtering. A.** Single (m_1) and multi-step (m_{MR}) estimations of the branching parameter m of a branching process, sampled with a virtual electrode with a $1/R^\gamma$ field of view. **B.** Amount of bias $\Delta m = m_{MR} - m_1$ in the estimation of m caused by the spatial sampling. **C.** Effect of (power-law shot noise) frequency filtering on the estimation of m. The timeseries is convolved with a filter that produces a $1/f^{\gamma_f}$ PSD.

mechanism. As seen in Fig. 3.10B, we can have $0 < \Delta m < 0.5$ depending on m. On the other hand, the presence of a low-pass frequency filter adds spurious temporal correlations in the dynamics, and quickly drives both m_{MR} and m_1 to 1. We observe this in Fig. 3.10C, where the power-law shot noise filter (that generates $PSD \sim 1/f^{\gamma_f}$) results in $m_{MR}, m_1 \approx 1$ for $\gamma_f > 0.5$. Thus, in the model, essentially any filtering of this type results in $\Delta m \approx 0$.

In conclusion, Δm can be used as a signature of the spatial sampling + frequency filtering mechanism that explains $0 \leq \beta < 4$ in the PSD. It predicts that poorly-sampled dynamics results in both shallow exponents ($\beta < 2$) and $\Delta m > 0$, while dynamics subject to low-pass filtering have $\beta > 2$ and $\Delta m = 0$.

3.3.4 *Analysis of experimental data*

In the previous section we described a combination of two mechanisms (spatial sampling and frequency filtering) capable of generating the PSD exponents observed in various measures of neuronal activity, and shown that spatial undersampling has a signature $\Delta m > 0$. In this section we analyze experimental data of different sources, and test if this signature can be found.

As previously mentioned, not only $\beta = 4$ is the hard limit of exponents observed experimentally, but the functional form of PSDs with heavy exponents $2 < \beta < 4$ has been observed to nicely follow Eq. 3.14 [8, 216]. We exemplify that in Fig. 3.12, where PSDs obtained from different experiments in vivo all seem to

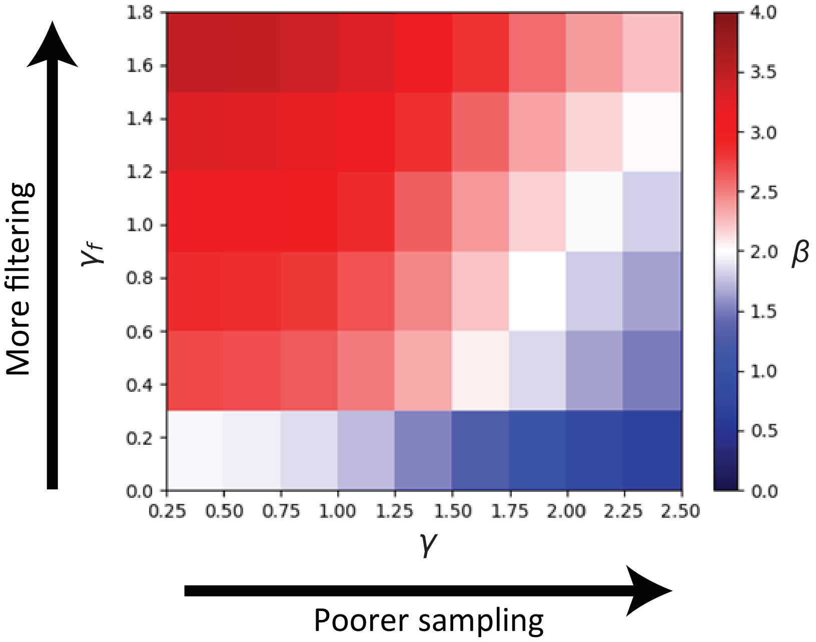

Figure 3.11: **PSD exponent β from a combination of filtering and sampling.** By combining the $1/R^{\gamma}$ electrode field of view (which decreases sampling with increasing γ) with the $1/f^{\gamma_f}$ frequency filter the entire range of exponents $0 \leq \beta < 4$ can be obtained.

follow a "$\gamma_f + 2$" scheme, with a varying γ_f exponent for low frequencies and $\gamma_f + 2$ for high frequencies.

This functional form is important, as it suggests activity described by a well-sampled correlated process convolved with a frequency filter[13]. Moreover, it suggests different dynamical states in different areas/behaviors. The functional form in Fig. 3.12A, for instance, indicates not only recordings subject to a $1/f$ filter, but that dynamics during slow-wave sleep were closer to a critical state than during awakeness[14]. Likewise, the PSD of Fig. 3.12B not only indicates a $1/f^{0.5}$ filter, but that dynamics in the CA3 region of the hippocampus is closer to criticality than in CA1. The anatomical structures of these regions differ, with CA3 being more recurrent and CA3 being more feedfoward. Thus, it supports the notion that more recurrent areas of the brain have longer timescales, and are thus closer to criticality.

In the case of in vitro cultures, on the other hand, it is unlikely that the extracelular medium (usually a saline solution) provides any type of frequency filtering. Thus, PSD exponents in vitro should be $\beta \leq 2$, and $\beta \ll 2$ should result

---

[13] Another functional form observed in experiments is $PSD \sim a/f^2 + b/\left(f_0^2 + f^2\right)$ with $a, b > 0$. Contrary to the one explored here, it suggests a combination of processes with different timescales [218, 219].

[14] This is compatible with other literature results on the relationship between behavior and dynamical states, see Sec. 2.5.2.

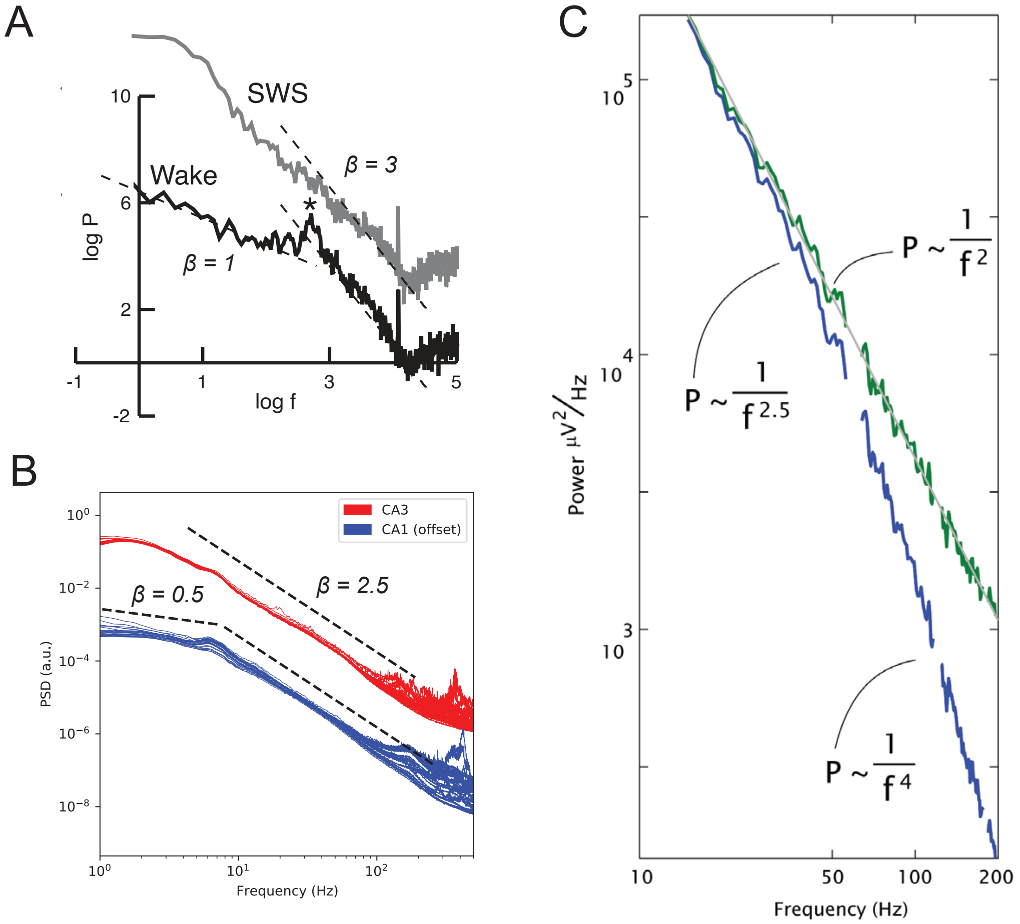

Figure 3.12: **PSDs observed in different experiments. A.** PSD of LFP recordings of the cat visual cortex during awakeness (black) and slow-wave sleep (SWS, gray). Dotted lines correspond to power-laws $1/f^{\beta}$. Adapted with permission from [8]. **B.** PSD of LFP recordings of the mouse hippocampus regions CA1 (red) and CA3 (blue, plotted with an offset) during sleep, from 32 channels each. Data from [217]. **C.** PSD of human ECoG recordings. The blue line corresponds to the original spectra, while the green line is the PSD multiplied by a form factor $1 + (f/f_0)^{4-\xi_L}$, with $\xi_L = 2$ and $f_0 = 75$Hz. Adapted from [216].

in $\Delta m > 0$. PSD exponents in vivo, on the other hand, should have $\beta > 2$ and $\Delta m \approx 0$.

In order to test these hypotheses we analyze electrophysiological data from both in vivo and in vitro experiments, which we briefly describe in the following. The in vitro LFP data comes from $n = 49$ recording sessions (with 60 electrodes) of cell cultures at varying stages of development (between DIV 7 and DIV 28), derived from the rat hippocampus. For the in vivo data, we use openly available data from rat, monkey and human sources. The rat data is described

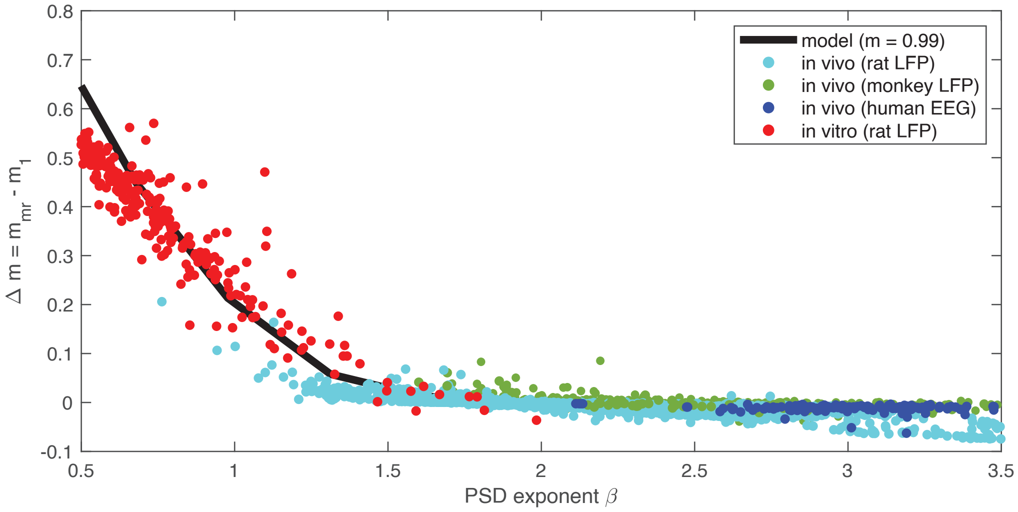

Figure 3.13: **Analysis of experimental data from various sources.** Red: in vitro LFP recordings from rat hippocampal cell cultures during development. Blue: LFP recordings of rat hippocampus during sleep, using data from [217]. Green: LFP recordings from monkey LFP (various regions), using data from [220]. Blue: intracranial EEG recordings from humans during task, using data from [221]. Black line: Simulation with $m = 0.99$, and a varying electrode field of view (varying γ) changing how well it samples the activity.

in [222], and consists of $n = 442$ recording sessions of the hippocampus of rats performing a variety of behaviors. It totals more than 200h of recordings from the CA1, CA3, DG and EC2-EC5 areas of the hippocampus. The monkey data comes from whole-hemisphere LFP recordings of a macaque encompassing various cortical regions (at various depths) and over a period of months. It is described in [220]. The human data is described in [221], and corresponds to intra-cranial EEG recordings of the frontal cortex of $n = 7$ epileptic patients performing a memory task.

We analyze the datasets by fitting the tail of the PSD with a $1/f^{\beta}$ function, and calculating the amount of bias Δm as described in Sec. 3.3.3. In order to limit possible bias due to effects not being modeled (such as oscillations) we apply a stringent censor on the data by discarding data points where the root mean square error (RMSE) of either the PSD or m fit is larger than 0.4. The results are shown in Fig. 3.13.

We find that, as predicted by the model, shallow exponents $\beta < 2$ are accompanied by a positive amount of bias Δm, mostly in the in vitro cultures. Thus it suggests that activity from the developing cultures is poorly sampled by LFP recordings. This could be due to either morphological differences resulting from the 2D embedding, or low density compared to in vivo, as cultures are a factor of 10-100 sparser [175, 176].

Results from the different in vivo systems, however, indicate spectra with a vast range of exponents β, all compatible with the dynamics being either well-sampled, or with filtering masking any undersampling effects ($\Delta m \approx 0$). The effects of poor sampling in Δm and β in data line-up well with what was found in the model, represented in Fig. 3.13 by a dynamics close to criticality ($m = 0.99$, black line) sampled with a $1/R^{\gamma}$ field of view and without filtering.

Our results show that Δm can be used to detect bias from poor sampling in electrophysiological measures of neuronal activity. They show that in vivo measures can be poorly-sampled, while in vivo measures can be subject to low-pass frequency filtering that introduces spurious temporal correlations in the dynamics. That said, care must be taken in order to properly interpret the results. On one hand, due to the stringent censoring, our results are only valid for dynamics that are well-described by auto-regressive dynamics. Datasets where oscillations dominate and make the estimations of m_{MR} and m_1 unreliable are removed, for instance.

More importantly, our results are compatible with the existing literature that claims various mechanisms to explain the variability in β [195–199, 223]: changes in firing rate, E-I balance and others could effectively result in a diminished capacity of the electrode to sample neuronal activity. Thus, our model presents an explanation of β in terms of dynamical effects which could be implemented by many different physiological mechanisms.

4

EFFECTS OF SAMPLING IN MEASURES OF NEURONAL AVALANCHES

This chapter contains the main result of this thesis [224]. Here, we show that neuronal avalanches (Sec. 2.2) obtained with coarse measures (such as EEG and LFP) are not indicatives of criticality, as considerably subcritical (but still correlated) dynamics can generate the same signatures. On the other hand, we show that subsampled activity (spikes) can differentiate critical from subcritical dynamics. This solves a contradiction in the literature: the characteristic power-laws of criticality are obtained *in vivo* under the most varied experimental settings under coarse measures, but never using spikes (see Sec. 2.5). In light of our results, we can reinterpret decades of results on criticality in neuronal avalanches as being actually evidence for a baseline subcritical dynamics.

Results shown here where obtained initially by me, under supervision of Dr. Viola Priesemann (V.P.). The model was later reimplemented in C++ by Franz Paul Spitzner (F.P.S.) for higher statistical significance, and the text and figures of this chapter were produced in conjunction with F.P.S. and V.P..

4.1 THE EXPERIMENTAL CONTRADICTION

For more than two decades, it has been argued that the cortex might operate at a critical point [1–6]. The criticality hypothesis states that by operating at a critical point, neuronal networks could benefit from optimal information-processing properties. Properties maximized at criticality include the correlation length [13], the autocorrelation time [4], the dynamic range [28, 29] and the richness of spatio-temporal patterns [30, 225].

Evidence for criticality in the brain often derives from measurements of **neuronal avalanches**. Neuronal avalanches are cascades of neuronal activity that spread in space and time. If a system is critical, the probability distribution of avalanche size $p(S)$ follows a power law $p(S) \sim S^{-\alpha}$ [13, 51]. Such power-law distributions have been observed repeatedly in experiments since they were first reported by Beggs & Plenz in 2003 [1].

However, not all experiments have produced power laws and the criticality hypothesis remains controversial. It turns out that results for cortical recordings *in vivo* differ systematically:

Studies that use what we here call **coarse-sampled** activity typically produce power-law distributions [1, 131, 132, 136, 138, 140, 145, 148, 156, 226, 227]. In contrast, studies that use **sub-sampled** activity typically do not [8, 100, 178, 179, 226, 228]. Coarse-sampled activity include LFP, M/EEG, fMRI and potentially calcium imaging, while sub-sampled activity is front-most spike recordings. We hypothesize that the apparent contradiction between coarse-sampled (LFP-like) data and sub-sampled (spike) data can be explained by the differences in the recording and analysis procedures.

In general, the analysis of neuronal avalanches is not straightforward. In order to obtain avalanches, one needs to define discrete events. While spikes are discrete events by nature, a coarse-sampled signal has to be converted into a binary form. This conversion hinges on thresholding the signal, which can be problematic [113–115, 211]. Furthermore, events have to be grouped into avalanches, and this grouping is typically not unique [179]. As a result, avalanche-size distributions depend on the choice of the threshold and temporal binning [1, 133].

Here, we show how thresholding and temporal binning interact with a (so far ignored) effect. Under coarse-sampling, neighboring electrodes may share the same field-of-view. This creates a distance-dependent *measurement overlap* so that the activity that is recorded at different electrodes may show *spurious correlations*, even if the underlying spiking activity is fully uncorrelated. We show that the inter-electrode distance may therefore impact avalanche-size distributions more severely than the underlying neuronal activity.

In the following, we explore the role of the recording and analysis procedures on a generic, locally-connected network of spiking neurons. We compare apparent signs of criticality under sub-sampling versus coarse-sampling. To that end, we vary the distance to criticality of the underlying system over a wide range, from uncorrelated (Poisson) to highly-correlated (critical) dynamics. We then derive signatures of criticality — as is done in experiments — and study how results depend on electrode distance and temporal binning.

4.2 MODEL DESCRIPTION

4.2.1 *Network model*

Our model is comprised of a two-level configuration, where a 2D network of $N_\mathrm{N} = 160000$ spiking neurons is sampled by a square array of $N_\mathrm{E} = 8 \times 8$ virtual electrodes. Neurons are distributed randomly in space (with periodic boundary conditions) and, on average, nearest neighbors are $d_\mathrm{N} = 50\,\mu\mathrm{m}$ apart. While the model is inherently unit-less, it is more intuitive to assign some length scale — in our case the inter-neuron distance d_N — to set that scale: all other size-dependent quantities can then be expressed in terms of the chosen d_N. For instance, the linear system size L can be derived by realizing that the random placement of neurons corresponds to an ideal gas. It follows that $L = 2\sqrt{N_\mathrm{N}}\, d_\mathrm{N} = 4\mathrm{c}m$ for uniformly distributed neurons. (For comparison, on a square lattice, the packing ratio would be higher and it is easy to see that the system size would be $\sqrt{N_\mathrm{N}}\, d_\mathrm{N}$.) Given the system size and neuron number, the overall neuronal density is $\rho = 100/\mathrm{m}m^2$. With our choice of parameters, the model matches typical experimental conditions in terms of inter-neuron distance, system size and neu-

Table 4.1: Values and descriptions of the model parameters.

Symbol	Value	Description
Δt	$2-16\,\mathrm{ms}$	Time-bin size (duration) for temporal binning
Θ_k	3	Activity threshold, in units of standard deviations of the time series of electrode k
δt	$2\,\mathrm{ms}$	Simulation time step
r	$1\,\mathrm{Hz}$	Average spike rate
N_N	1.6×10^5	Number of neurons
d_N	$50\,\mu\mathrm{m}$	Inter-neuron distance (measured between nearest neighbors)
L	$4\,\mathrm{cm}$	Linear system size
ρ	$100/\mathrm{mm}^2$	Neuronal density
K	1000	Average network degree (outgoing connections per neuron)
d_{max}	$1.78\,\mathrm{mm}$	Connection length; all neurons within d_{max} are connected
σ	$300\,\mu\mathrm{m}$	Effective length of synaptic connections, sets the distance-dependence of the probabilities of recurrent activations
N_E	8×8	Number of electrodes
d_E	$50-500\,\mu\mathrm{m}$	Inter-electrode distance
d_E^*	$10\,\mu\mathrm{m}$	Dead-zone around each electrode (no neurons present)

ron density (see Table 4.1 for details). The implementation of the model in C++, and the python code used to analyze the data and generate the figures, are available online at https://github.com/Priesemann-Group/criticalavalanches.

4.2.2 *Topology*

We consider a topology that enforces *local* spreading dynamics. Every neuron is connected to all of its neighbors within a threshold distance d_{max}. The threshold is chosen so that on average $K = 10^3$ outgoing connections are established per neuron. We thus seek the radius d_{max} of a disk whose area contains K neurons. Using the already known neuron density, we find $d_{max} = \sqrt{K/\pi\rho} \approx 1.78\,\mathrm{mm}$. For every established connection, the probability of a recurrent activation decreases with increasing neuron distance. Depending on the particular distance d_{ij} between the two neurons i and j, the connection has a normalized weight $w_{ij} = e^{-d_{ij}^2/2\sigma^2} / \Omega_i$ (with normalization constant $\Omega_i = \sum_{j'} e^{-d_{ij'}^2/2\sigma^2}$). Our weight definition approximates the distance dependence of average synaptic strength. The parameter σ sets the *effective* distance over which connections can form ($d_{\max}$ is an upper limit for σ and mainly speeds up computation.) In the limit $\sigma \to \infty$, the network is all-to-all connected. In the limit $\sigma \to 0$, the network is completely disconnected. Therefore, the effective connection length σ enables us to fine tune *how local* the dynamic spreading of activity is. In our simulations, we choose $\sigma = 6d_{\mathrm{N}} = 300\,\mu\mathrm{m}$. Thus, the overall reach is much shorter than $d_{\mathrm{m}ax}$ ($\sigma \approx 0.06\, d_{\mathrm{m}ax}$).

4.2.3 *Dynamics*

To model the dynamic spreading of activity, time is discretized to a chosen simulation time step, here $\delta t = 2\,\mathrm{ms}$, which is comparable to experimental evidence on synaptic transmission [229]. Our simulations run for 10^6 time steps on an ensemble of 50 networks for each configuration (combination of parameters and dynamic state). This corresponds to ~ 277 hours of recordings for each dynamic state.

The activity spreading is modeled using the dynamics of a branching process with external drive [110, 178]. At every time step t, each neuron i has a state $s_i(t) = 1$ (spiking) or 0 (quiescent). If a neuron is spiking, it tries to activate its connected neighbors — so that they will spike in the next time step. All of these recurrent activations depend on the *branching parameter* m: Every attempted activation has a probability $p_{ij} = m\ w_{ij}$ to succeed. (Note that the distance-dependent weights are normalized to 1 but the activation probabilities are normalized to m.) In addition to the possibility of being activated by its neighbors, each neuron has a probability h to spike spontaneously in the next time step. After spiking, a neuron is reset to quiescence in the next time step if it is not activated again.

Our model gives us full control over the dynamic state of the system — and its distance to criticality. The dynamic state is described by the *intrinsic timescale* τ. We can analytically calculate the intrinsic timescale $\tau = -\delta t / \ln{(m)}$, where δt is the duration of each simulated time step. Note that m — the control parameter that *tunes the system* — is set on the neuron level while τ is a (collective) network property (that in turn allows us to deduce an *effective* m). As the system is pushed more towards criticality (by setting $m \to 1$), the intrinsic timescale diverges $\tau \to \infty$.

For consistency, we measure the intrinsic timescale during simulations. To that end, the (fully sampled) population activity at each time step is given by the number of active neurons $A(t) = \sum_i s_i(t)$. A linear least-squares fit of the autoregressive relation $A(t+1) = e^{-\delta t/\tau} A(t) + N_{\mathrm{N}} h$ over the full simulated time series yields an estimate $\hat{\tau}$ that describes each particular realization.

By adjusting the branching parameter m (setting the dynamic state) *and* the probability for spontaneous activations h (setting the drive), we control the distance to criticality *and* the average stationary activity. The activity is given by the *average spike rate* $r = h/(\delta t(1-m))$ of the network. For all simulations, we fix the rate to $r = 1\mathrm{Hz}$ in order to avoid rate effects when comparing different states (see Table 4.3 for the list of parameter combinations). Note that, due to the non-zero drive h and the desired stationary activity, the model cannot be perfectly critical ($\hat{\tau} \to \infty$, see Table 4.3).

4.2.4 *Coalescence Compensation*

With our probability-based update rules, it may happen that target neurons are simultaneously activated by multiple sources. This results in so-called *coalescence effects* that are particularly strong in our model due to the local activity spreading [111]. For instance, naively setting $m = 1$ (with $\sigma = 300\,\mu\mathrm{m}$) would result in an effective (measured) $\hat{m} \approx 0.98$, which has considerably different properties. Compared to e.g. $m = 0.999$ this would result in a 20-fold decrease in τ.

In order to compensate these coalescence effects, we apply a simple but effective fix: If an activation attempt is successful but the target neuron is already marked to spike in the next time step, another (quiescent) target is chosen. Because our implementation stores all the connected target neurons as a list sorted by their distance to the source, it is easy to activate the next neuron in that list. Thereby, the equivalent probability of the performed activation is as close to the originally attempted one as possible.

4.2.5 *Virtual Electrode Recordings*

Our simulations are designed to mimic sampling effects of electrodes in experimental approaches. To simulate sampling, we use the readout of $N_\mathrm{E} = 64$ virtual electrodes that are placed in an 8×8 grid. Electrodes are separated by an inter-electrode distance that we specify in multiples of inter-neuron distance d_N. It is kept constant for each simulation and we study the impact of the inter-electrode distance by repeated simulations spanning electrode distances between $1d_\mathrm{N} = 50\,\mu\mathrm{m}$ and $10d_\mathrm{N} = 500\,\mu\mathrm{m}$. The electrodes are modeled to be point-like objects in space that have a small dead-zone of $d_\mathrm{E}^* = d_\mathrm{N}/5 = 10\,\mu\mathrm{m}$ around their origin. Within the dead-zone, no signal can be recorded (in fact, we implement this by placing the electrodes first and the neurons second — and forbid neuron placements too close to electrodes.)

Using this setup, we can apply sampling that emulates either the detection of spike times or LFP-like recordings. To model the detection of spike times, each electrode only observes the single neuron that is closest to it. Whenever this particular neurons spikes, the timestamp of the spike is recorded. All other neurons are neglected — and the dominant sampling effect is *sub-sampling*. On the other hand, to model LFP-like recordings, each electrode integrates the spiking of all neurons in the system. The contribution of a spike, e.g. from neuron i to electrode k, decays as $1/d_{ik}$ with the neuron-to-electrode distance. (Changing the dependence to d_{ik}^{-2} has no qualitative impact on the results.) The total signal of the electrode at time t is then $V_k(t) = \sum_i^{N_\mathrm{N}} s_i(t)/d_{ik}$. (Diverging electrode signals are prevented by the forbidden zone around the electrodes.) For such coarse-sampled activity, all neurons contribute to the signal and the contribution is weighted by their distance.

4.2.6 *Avalanches*

Taking into account all 64 electrodes, a new avalanche starts (by definition [1]) when there is at least one event (spike) in a time bin — given there was no event in the previous time bin (see Fig. 4.2). An avalanche ends whenever an empty bin is observed (no event over the duration of the time bin). Hence, an avalanche persists for as long as every consecutive time bin contains at least one event — which is called the *avalanche duration* D. From here, it is easy to count the total number of events that were recorded across all electrodes and included time bins — which is called the *avalanche size* S. The number of occurrences of each avalanche size (or duration) are sorted into a histogram that describes the avalanche distribution.

4.2.7 *Analysis of Avalanches under Coarse and Sub-sampling*

We analyze avalanche size distributions in a way that is as close to experimental practice as possible (see Fig. 4.2). From the simulations described above, we obtain two outputs from each electrode: a) a list containing spike times of the single closest neuron and b) a time series of the integrated signal to which all neurons contributed.

In case of the (sub-sampled) spike times a), the spiking events are already present in binary form. Thus, to define a neural avalanche, the only required parameter is the size of the time bin Δt (for instance, we may choose $\Delta t = 4\,\mathrm{ms}$).

In case of the (coarse-sampled) time series b), binary events need to be extracted from the continuous electrode signal. The extraction of spike times from the continuous signal relies on a criterion to differentiate if the set of observed neurons is spiking or not — which is commonly realized by applying a threshold. (Note that now thresholding takes place on the electrode level, whereas previously, an event belonged to a single neuron.) Here, we obtain avalanches by thresholding as follows: First, all time series are frequency filtered to $0.1\,\mathrm{Hz} < f < 200\,\mathrm{Hz}$. This demeans and smoothes the signal (and reflects common hardware-implemented filters of LFP recordings). Second, the mean and standard deviation of the full time series are computed for each electrode. The mean is virtually zero due to the high-pass filtering. Each electrode's threshold is set to three standard deviations above the mean. Third, for every positive excursion of the time series (i.e. $V_k(t) > 0$), we recorded the timestamp $t = t_{\mathrm{m}ax}$ of the maximum value of the excursion. An event was defined when $V_k(t_{\mathrm{m}ax})$ was larger than the threshold Θ_k of three standard deviations of the (electrode-specific) time series. (Whenever the signal passes the threshold, the timestamps of all local maxima become candidates for the event; however, only the one largest maximum *between two crossings of the mean* assigns the final event-time.) Once the continuous signal of each electrode has been mapped to binary events with timestamps, the remaining analysis steps were the same for coarse-sampled and sub-sampled data.

Table 4.2: Fitted exponents of $\alpha \sim \Delta t^{-\beta}$.

Dynamic state	β	
	$d_E = 200\,\mu\text{m}$	$d_E = 400\,\mu\text{m}$
in vitro (LFP) [1]	0.16 ± 0.01	
Critical (coarse)	0.113 ± 0.001	0.141 ± 0.001
Reverberating (coarse)	0.127 ± 0.003	0.156 ± 0.002
Subcritical (coarse)	0.159 ± 0.004	0.231 ± 0.016
Critical (spikes)	0.143 ± 0.010	0.123 ± 0.005

4.2.8 *Power-law fitting and shape collapse*

Avalanche size and duration distributions are fitted to power-laws using the powerlaw package [230]. The shape collapse of Eq. 4.6 is done following the algorithm described in [128]. Briefly, the avalanche profiles $s(t, D)$ of all avalanches with the same duration D are averaged, and the resulting curve is scaled to t/D and interpolated on 1000 points in the $[0, 1]$ range. Avalanches with $D < 4$, or with less than 20 realizations are removed. The chosen collapse exponent γ is the one that minimizes the error function:

$$E = \frac{\langle \mathrm{Var}(X_D/D^{\gamma-1}) \rangle}{\Delta X^2} \tag{4.1}$$

where $X_D(t/D)$ is the interpolated average shape of avalanches with size D, and $\Delta X = \max_{t,D}(X_D/D^{\gamma-1}) - \min_{t,D}(X_D/D^{\gamma-1})$. The variance $\mathrm{Var}(.)$ is calculated over all valid D, and the mean $\langle . \rangle$ is taken over the scaled duration t/D. For interpolation and minimization we use the scipy [231] functions InterpolatedUnivariateSpline and minimize, respectively.

4.3 RESULTS

The aim of this study is to understand **how the sampling of neural activity** affects the inference of the underlying collective dynamics. It is not about introducing a novel model that might generate critical dynamics. Therefore, we use an established phenomenological model, where the distance to criticality can be precisely tuned. To study sampling effects, we use a two-level setup inspired by [155]: An underlying network model, on which activity is then *sampled* with a grid of 8×8 virtual electrodes. All parameters of the model, the sampling and the analysis are closely matched to those known from experiments (see Methods).

In order to evaluate sampling effects, we want to *precisely* set the underlying dynamics. Therefore, we employ the established branching model, which is well understood analytically [30, 110, 111, 155, 178]. Inspired by biological neuronal networks, we simulate the branching dynamics on a dense 2D topology with $N_{\mathrm{N}} = 160\,000$ neurons where each neuron is connected to $K \approx 1000$ local neighbors. To emphasize the locality, the synaptic strength of connections decays with the distance d_{N} between neurons. For a detailed comparison with different topologies, see the Supplemental Information (Fig. 4.8).

4.3.1 *The branching parameter m sets the distance to criticality*

In order to compare apparent signatures of criticality with the true, underlying dynamics, we first give some intuition about the branching model. The **branching parameter** m quantifies the probability of *postsynaptic activations*, or in other words, how many subsequent spikes are caused (on average) by a single spike. With increasing $m \to 1$, a single spike triggers increasingly long cascades of activity. These cascades determine the timescale over which fluctuations occur in the population activity — this **intrinsic timescale** τ describes the dynamic state of the system and its distance to criticality.

The intrinsic timescale can be analytically related to the branching parameter by $\tau \sim -1/\ln(m)$. As $m \to 1$, $\tau \to \infty$ and the population activity becomes "bursty". We illustrate this in Fig. 4.1B and Table 4.3: For Poisson-like dynamics ($m \approx 0$), the intrinsic timescale is zero ($\hat{\tau}_{psn} \approx 0\,\mathrm{ms}$) and the activity between neurons is uncorrelated. As the distance to criticality becomes smaller ($m \to 1$), the intrinsic timescale becomes larger ($\hat{\tau}_{sub} \approx 19\,\mathrm{ms}$, $\hat{\tau}_{rev} \approx 98\,\mathrm{ms}$, $\hat{\tau}_{crit} \approx 1.6\,\mathrm{s}$), fluctuations become stronger, and the spiking activity becomes more and more correlated in space and time.

Table 4.3: Parameters and intrinsic timescales of dynamic states. All combinations of branching parameter m and per-neuron drive h result in a stationary activity of 1 Hz per neuron. Due to the recurrent topology, it is more appropriate to consider the measured autocorrelation time $\hat{\tau}$ rather than the analytic timescale τ.

State name	m	$\hat{\tau}$ (measured)	$\tau = \frac{-2\,\mathrm{ms}}{\ln m}$	h
Poisson	0.0	$0.1 \pm 0.1\,\mathrm{ms}$	$0.0\,\mathrm{ms}$	2×10^{-3}
Subcritical	0.9	$18.96 \pm 0.09\,\mathrm{ms}$	$18.9\,\mathrm{ms}$	2×10^{-4}
Reverberating	0.98	$98.3 \pm 1.0\,\mathrm{ms}$	$98.9\,\mathrm{ms}$	4×10^{-5}
Critical	0.999	$1.58 \pm 0.12\,\mathrm{s}$	$1.99\,\mathrm{s}$	2×10^{-6}

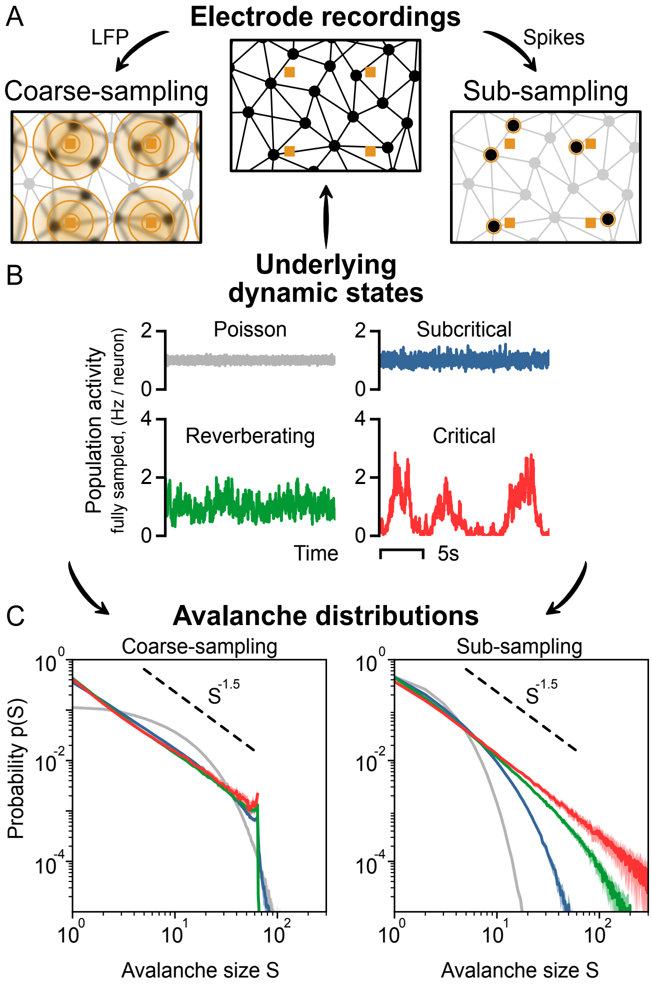

Figure 4.1: **Sampling affects the assessment of dynamic states from neuronal avalanches. A:** Representation of the sampling process of neurons (black circles) using electrodes (orange squares). Under coarse-sampling (e.g. LFP), activity is measured as a weighted average in the electrode's vicinity. Under sub-sampling (spikes), activity is measured from few individual neurons. **B:** Fully sampled population activity of the neuronal network, for states with varying intrinsic timescales τ: Poisson ($\hat{\tau}_{psn} \approx 0\,\mathrm{ms}$), subcritical ($\hat{\tau}_{sub} \approx 19\,\mathrm{ms}$), reverberating ($\hat{\tau}_{rev} \approx 98\,\mathrm{ms}$) and critical ($\hat{\tau}_{crit} \approx 1.6\,\mathrm{s}$). **C:** Avalanche-size distribution $p(S)$ for coarse-sampled (left) and sub-sampled (right) activity. Sub-sampling allows for separating the different states, while coarse-sampling leads to $p(S) \sim S^{-\alpha}$ for all states except Poisson. **Parameters:** Inter-electrode distance $d_{\mathrm{E}} = 400\,\mu\mathrm{m}$ and time-bin size $\Delta t = 8\,\mathrm{ms}$.

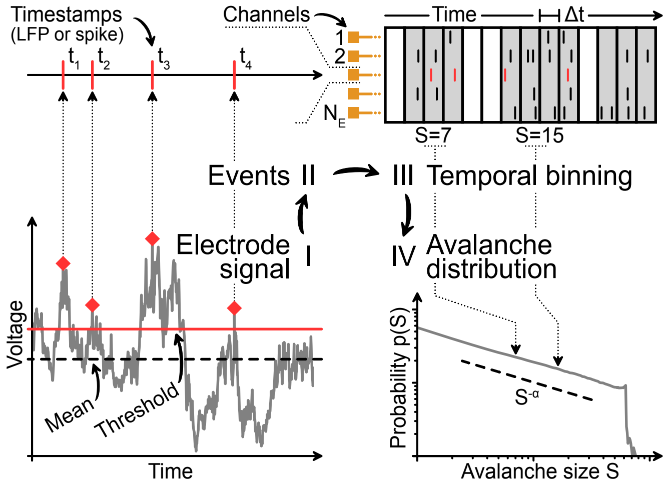

Figure 4.2: **Analysis pipeline for avalanches from sampled data. I:** Under coarse-sampling (LFP-like), the recording is demeaned and thresholded. **II:** The timestamps of events are extracted. Under sub-sampling (spikes), timestamps are obtained directly. **III:** Events from all channels are binned with time-bin size Δt and summed. The size S of each neuronal avalanche is calculated. **IV:** The probability of an avalanche size is given by the (normalized) count of its occurrences throughout the recording.

4.3.2 *Avalanches are extracted differently under coarse-sampling and sub-sampling*

At each electrode, we sample both the spiking activity of the closest neuron (sub-sampling) and a spatially averaged signal that emulates LFP-like coarse-sampling.

Both **sub-sampling** and **coarse-sampling** are sketched in Fig. 4.1A: For coarse-sampling (left), the signal from each electrode channel is composed of varying contributions (orange circles) of all surrounding neurons. The contribution of a particular spike from neuron i to electrode k decays as $1/d_{ik}$ with the neuron-to-electrode distance d_{ik} (see Supplemental Information for an extended discussion on the impact of the distance dependence). In contrast, if spike detection is applied (Fig. 4.1A, right), each electrode signal captures the spiking activity of few individual neurons (highlighted circles).

To test both recording types for criticality, we apply the standard analysis that provides a probability distribution $p(S)$ of the *avalanche size* S: In theory, an avalanche describes a cascade of activity where individual units — here neurons — are consecutively and causally activated. Each activation is called an event. The avalanche size is then the total number of events in the time between the first and the last activation. A power law in the size distribution of these avalanches is a hallmark of criticality [4]. In practice, the actual size of an avalanche is hard to determine because individual avalanches are not clearly separated in time; the coarse-sampled signal is continuous-valued and describes the local population.

In order to extract binary events for the avalanche analysis (Fig. 4.2), the signal has to be thresholded — which is not necessary for spike recordings, where binary events are inherently present as timestamps.

4.3.3 *Coarse-sampling makes dynamic states indistinguishable*

Irrespective of the applied sampling, the inferred avalanche distribution *should* represent the true dynamic state of the system.

However, under coarse-sampling (Fig. 4.1C, left), the avalanche-size distributions of the subcritical, reverberating and critical state are virtually indistinguishable. Intriguingly, all three show a power law. The observed exponent $\alpha = 1.5$ is associated with a critical branching process. Only the uncorrelated (Poisson-like) dynamics produce a non-power-law decay of the avalanche-size distribution.

Under sub-sampling (Fig. 4.1C, right), each dynamic state produces a unique avalanche-size distribution. Only the critical state, with the longest intrinsic timescale, produces the characteristic power law. Even the close-to-critical, reverberating regime is clearly distinguishable and features a "subcritical decay" of $p(S)$.

4.3.4 *Measurement overlap causes spurious correlations*

Why are the avalanche-size distributions of different dynamic states hard to distinguish under coarse-sampling? The answer is hidden within the cascade of steps involved in the recording and analysis procedure. Here, we separate the impact of the involved processing steps. Most importantly, we discuss the consequences of *measurement overlap* — which we identify as a key explanation for the ambiguity of the distributions under coarse-sampling.

In order to obtain discrete events from the continuous time series for the avalanche analysis, each electrode signal is filtered and thresholded, binned with a chosen time-bin size Δt and, subsequently, the events from all channels are stacked. This procedure is problematic because **(i)** electrode proximity adds spatial correlations, **(ii)** temporal binning adds temporal correlations, and **(iii)** thresholding adds various types of bias [113–115].

As a result of the involved analysis of coarse-sampled data, spurious correlations are introduced that are not present in sub-sampled data. We showcase this effect in Fig. 4.3, where the Pearson correlation coefficient between two virtual electrodes is compared for both the (thresholded and binned) coarse-sampled and sub-sampled activity. For the same parameters and dynamic state, coarse-sampling leads to larger correlations than sub-sampling.

Depending on the distance between electrodes, multiple electrodes might record activity from the same neuron. This **measurement overlap** (or volume conduction effect) increases the spatial correlations between electrodes — and because

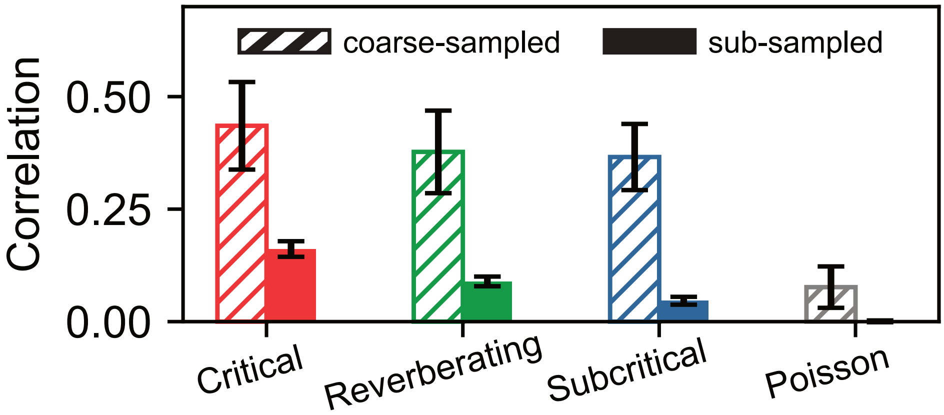

Figure 4.3: **Coarse-sampling leads to greater correlations than sub-sampling.** Pearson correlation coefficient between the signals of two adjacent electrodes for the different dynamic states. Even for independent (uncorrelated) Poisson activity, measured correlations under coarse-sampling are non-zero. **Parameters:** Inter-electrode distance $d_\mathrm{E} = 400\,\mu\mathrm{m}$ and time-bin size $\Delta t = 8\,\mathrm{ms}$.

from the signals from multiple electrode channels are combined in the analysis, correlations can originate from measurement overlap alone.

4.3.5 *Inter-electrode distance shapes criticality*

Due to the measurement overlap, avalanche-size distributions under coarse-sampling depend on the inter-electrode distance d_E (Fig. 4.4A). For small inter-electrode distances, the overlap is strong. Thus, the spatial correlations are strong. Strong correlations manifest themselves in *larger* avalanches. However, under coarse-sampling the maximal observed size S of an avalanche is limited by the number of electrodes N_E [155]. This limit due to N_E manifests as a sharp cut-off and — in combination with spurious measurement correlations due to d_E — can shape the probability distribution. In the following, we show that these factors can be more dominant than the actual underlying dynamics.

In theory, supercritical dynamics are characterized by a *sharp peak* in the avalanche distribution at $S = N_\mathrm{E}$. Independent of the underlying dynamics, such a peak can originate from small electrode distances (Fig. 4.4A, $d_\mathrm{E} = 100\,\mu\mathrm{m}$): Avalanches are likely to span the small area covered by the electrode array. Furthermore, due to strong measurement overlap, individual events of the avalanche may contribute strongly to multiple electrodes.

Subcritical dynamics are characterized by a *pronounced decay* already for $S < N_\mathrm{E}$. Independent of the underlying dynamics, such a decay can originate from large electrode distances (Fig. 4.4A, $d_\mathrm{E} = 500\,\mu\mathrm{m}$): Locally propagating avalanches are unlikely to span the large area covered by the electrode array. Furthermore,

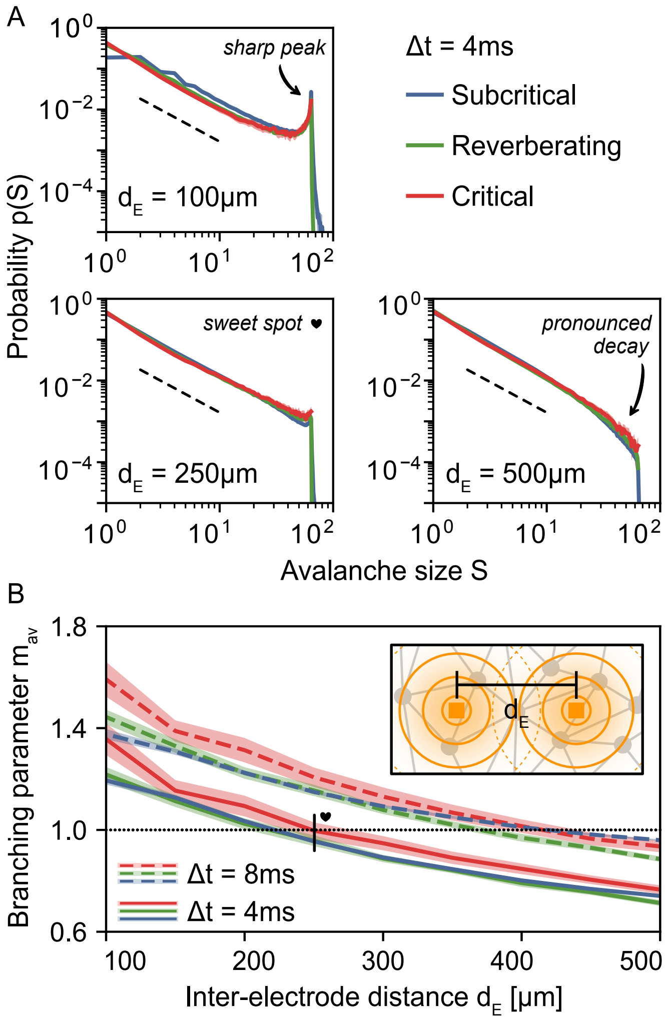

Figure 4.4: **Under coarse-sampling, apparent dynamics depend on the inter-electrode distance d_E. A:** For small distances ($d_E = 100\,\mu m$), the avalanche-size distribution $p(S)$ indicates (apparent) supercritical dynamics: $p(S) \sim S^{-\alpha}$ with a *sharp peak* near the electrode number $N_E = 64$. For large distances ($d_E = 500\,\mu m$), $p(S)$ indicates subcritical dynamics: $p(S) \sim S^{-\alpha}$ with a *pronounced decay* already for $S < N_E$. There exists a *sweet-spot* value ($d_E = 250\,\mu m$) for which $p(S)$ indicates critical dynamics: $p(S) \sim S^{-\alpha}$ until the the cut-off is reached at $S = N_E$. The particular sweet-spot value of d_E depends on time-bin size (here, $\Delta t = 4\,ms$). As a guide to the eye, dashed lines indicate $S^{-1.5}$. **B:** The branching parameter m_{av} is also biased by d_E when estimated from neuronal avalanches. Apparent criticality ($m_{av} \approx 1$, dotted line) is obtained with $d_E = 250\,\mu m$ and $\Delta t = 4\,ms$ but also with $d_E = 400\,\mu m$ and $\Delta t = 8\,ms$. **B, Inset:** representation of the measurement overlap between neighboring electrodes; when electrodes are placed close to each other, spurious correlations are introduced.

due to the weaker measurement overlap, individual events of the avalanche may contribute strongly to one electrode (or to multiple electrodes but only weakly).

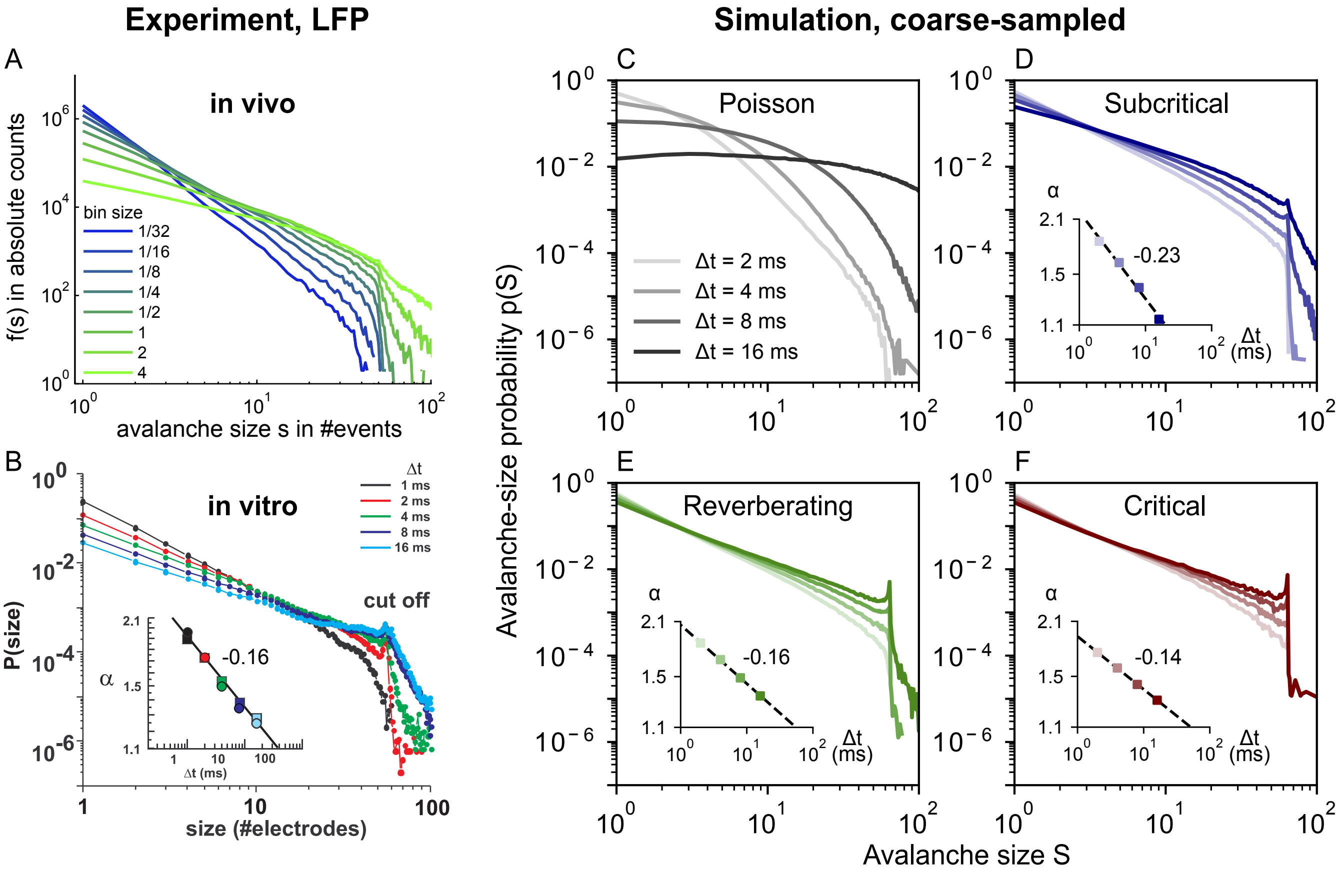

Figure 4.5: **In vivo and in vitro avalanche-size distributions $p(S)$ from LFP depend on time-bin size Δt.** Experimental LFP results are reproduced by many dynamics states of coarse-sampled simulations. **A:** Experimental *in vivo* results (LFP, human) from an array of 60 electrodes, adapted from [137]. **B:** Experimental *in vitro* results (LFP, culture) from an array with 60 electrodes, adapted from [1]. **C–F:** Simulation results from an array of 64 virtual electrodes and varying dynamic states, with time-bin sizes between $2\,\text{ms} \leq \Delta t \leq 16\,\text{ms}$ and $d_\text{E} = 400\,\mu\text{m}$. Subcritical, reverberating and critical dynamics produce power-law distributions with bin-size-dependent exponents α. **Insets:** Distributions are fitted to $p(S) \sim S^{-\alpha}$. The magnitude of α decreases as $\Delta t^{-\beta}$ with $-\beta$ indicated next to the insets.

Consequently, there exists a *sweet-spot* value of the inter-electrode distance d_E for which $p(S)$ appears convincingly critical (Fig. 4.4A, $d_\text{E} = 250\,\mu\text{m}$): a power law $p(S) \sim S^{-\alpha}$ spans all sizes up to the cut-off at $S = N_\text{E}$. However, the dependence on the underlying dynamic state is minimal.

Independently of the apparent dynamics, we observe the discussed cut-off at $S = N_\text{E}$, which is also often seen in experiments (Fig. 4.5). Note, however, that this cut-off only occurs under coarse-sampling (see again Fig. 4.1C). When spikes are used instead (Fig. 4.6), the same avalanche can reach an electrode

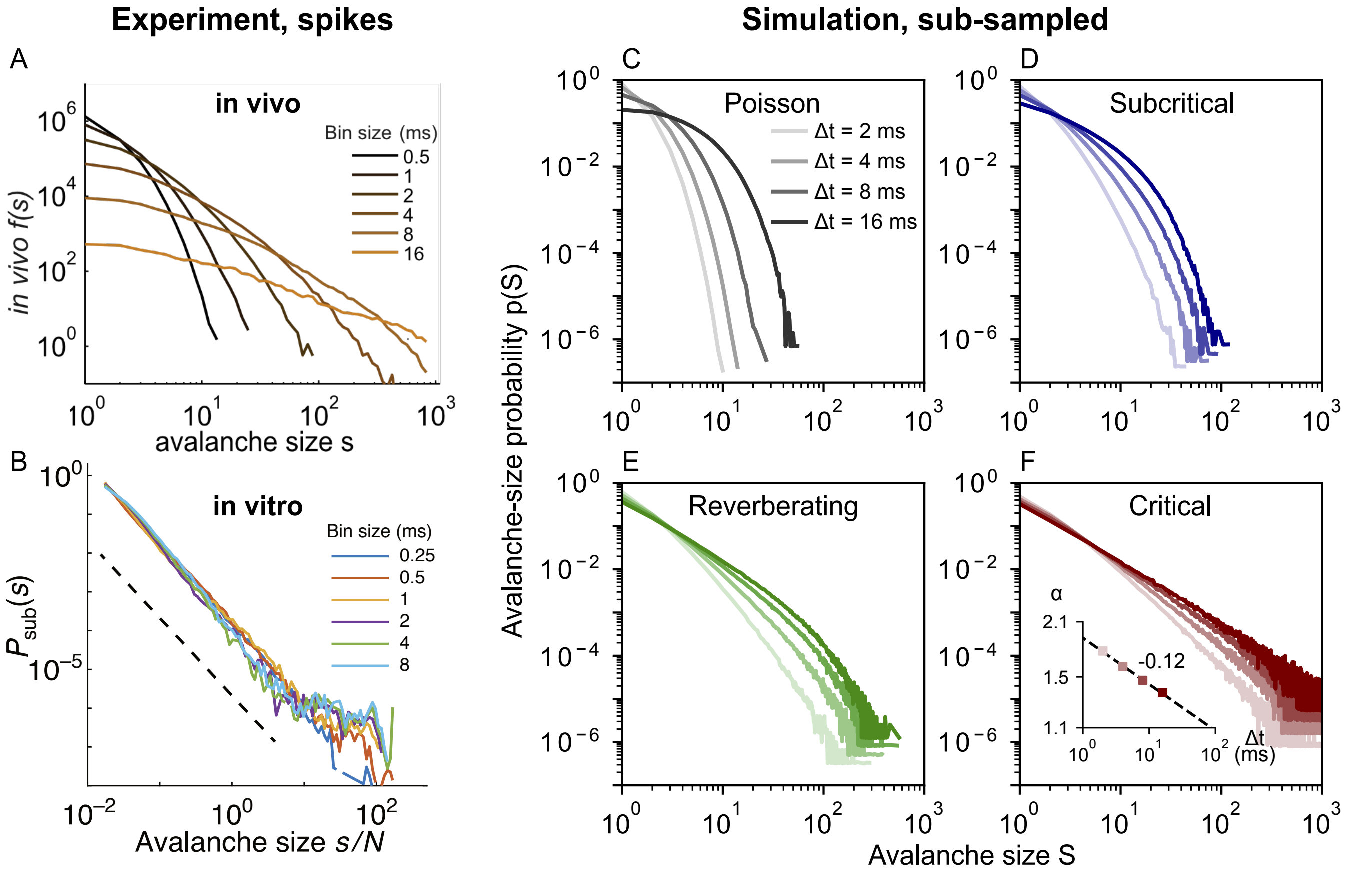

Figure 4.6: ***In vivo* avalanche-size distributions $p(S)$ from spikes depend on time-bin size Δt. *In vivo* results from spikes are reproduced by sub-sampled simulations of subcritical to reverberating dynamics.** Neither spike experiments nor sub-sampled simulations show the cut-off that is characteristic under coarse-sampling. **A:** Experimental *in vivo* results (spikes, awake monkey) from an array of 16 electrodes, adapted from [179]. The pronounced decay and the dependence on bin size indicate subcritical dynamics. **B:** Experimental *in vitro* results (spikes, culture DIV 34) from an array with 59 electrodes, adapted from [22]. Avalanche-size distributions are independent of time-bin size and produce a power law over four orders of magnitude. In combination, this indicates critical dynamics with a separation of timescales. **C–F:** Simulation for sub-sampling, analogous to Fig. 4.5. Subcritical dynamics do not produce power-law distributions and are clearly distinguishable from critical dynamics. **F:** Only the (close-to) critical simulation produces power-law distributions. Note the dependence on time-bin size: In contrast to the *in vitro* culture, the simulation does not feature a separation of time scales (due to external drive and stationary activity) which causes a bin-size dependence.

repeatedly in quick succession — whereas such double-events are circumvented when thresholding at the population level. For more details see Fig. 4.9.

A further signature of criticality is obtained by estimating the branching parameter. This is traditionally done at the avalanche level: The *estimated branching parameter* of the neuronal avalanches, m_{av}, is defined as the average ratio of events between subsequent time bins in an avalanche, i.e. during non-zero activity [1, 133]. Note that, due to coalescence and drive effects, m_{av} can differ from m proper [111, 179].

Obtaining m_{av} for different electrode distances results in a picture consistent with the one from avalanche-size distributions (Fig. 4.4B). In general, the dependence on the electrode distance is stronger than the dependence on the underlying state. At the particular value of the inter-electrode distance where $m_{av} = 1$, the distributions appear critical. If $m_{av} < 1$ ($m_{av} > 1$), the distributions appear subcritical (supercritical). Because the probability distributions and the estimated branching parameter share this dependence, a wide range of dynamic states would be consistently misclassified — solely as a function of the inter-electrode distance.

4.3.6 *Temporal binning determines scaling exponents*

Apart from the inter-electrode distance, the choice of temporal discretization that underlies the analysis may alter avalanche-size distributions. This *time-bin size* Δt varies from study to study and it can severely impact the observed distributions [1, 22, 137, 179]. With smaller bin sizes, avalanches tend to be separated into small clusters, whereas larger bin sizes tend to "glue" subsequent avalanches together [179]. Interestingly, this not only leads to larger avalanches, but specifically to $p(S) \sim S^{-\alpha}$, where the exponent α increases systematically with bin size [1, 137]. Such a changing exponent is not expected for conventional systems that self-organize to criticality: Avalanches would be *separated in time*, and α should be fairly bin-size invariant for a large range of Δt [22, 81, 179].

Our coarse-sampled model reproduces these characteristic experimental results (Fig. 4.5). It also reproduces the previously reported scaling [1] of the exponent with bin size $\alpha \sim \Delta t^{-\beta}$ (Fig. 4.5, insets). Except for the Poisson dynamics, all the model distributions show power laws. Moreover the distributions are strikingly similar, not just to the experimental results, but also to each other. This emphasizes how sensitive signs of criticality are to analysis parameters: All the shown dynamic states are consistent with the ubiquitous avalanche-size distributions that are observed in coarse-sampled experiments.

When spikes are used instead, power-law distributions only arise from critical dynamics. For comparison with the coarse-sampled results in Fig. 4.5, we show avalanche-size distributions from experimental spike recordings and subsampled simulations in Fig. 4.6. In this case, power laws are produced only by in vitro cultures and the simulations that are (close-to) critical. In vivo spike recordings on awake subjects and simulations of subcritical dynamics produce distributions that feature a pronounced decay instead of power laws. In contrast to coarse-sampling, the avalanche distributions that stem from sub-sampled measures (spikes) allow us to clearly tell apart the underlying dynamic states from one another.

Overall, as our results on coarse-sampling have shown, different sources of bias — here the measurement overlap and the bin size — can perfectly outweigh each other. For instance, smaller electrode distances (that increase correlations) can be compensated by making the time-bin size smaller (which again decreases correlations). This was particularly evident in Fig. 4.4B, where increasing d_E could be outweighed by increasing Δt in order to obtain a particular value for the branching parameter m_{av}. The same relationship was again visible in Fig. 4.5C-F: For the shown $d_\mathrm{E} = 400\,\mu\mathrm{m}$ (see also Fig. 4.12 for $d_\mathrm{E} = 200\,\mu\mathrm{m}$), only $\Delta t = 8\,\mathrm{ms}$ results in $\alpha = 1.5$ — the correct exponent for the underlying dynamics. Since the electrode distance cannot be varied in most experiments, selecting anything but the one "lucky" Δt will cause a bias.

4.3.7 *Scaling laws fail under coarse-sampling*

The most used indication of criticality in neuronal dynamics is the avalanche-size distribution $p(S)$. However, at criticality, the *avalanche duration distribution* $p(D)$ and the *average avalanche size* for a given duration, $\langle S\rangle(D)$, should also follow power-laws, each with a respective *critical exponent* [51]:

$$p(S) \sim S^{-\alpha} \tag{4.2}$$

$$p(D) \sim D^{-\beta} \tag{4.3}$$

$$\langle S\rangle(D) \sim D^{\gamma} \tag{4.4}$$

The exponents are related to one another by the scaling relationship

$$\frac{\beta - 1}{\alpha - 1} = \gamma\,. \tag{4.5}$$

For a pure branching process — or any process in the mean-field directed percolation universality class [13, 232] — they take the values $\alpha = 3/2$, $\beta = 2$ and $\gamma = 2$.

Lastly, at criticality, avalanches of vastly different duration still have the same *average shape*: The activity $s(t, D)$ at any given time t (within the avalanche's lifetime D) is described by a universal scaling function $\mathscr{F}$, so that

$$s(t, D) \sim D^{\gamma-1}\mathscr{F}(t/D)\,. \tag{4.6}$$

In other words, changing $s(t, D) \to s(t, D)/D^{\gamma-1}$ and $t \to t/D$ should result in a data collapse for the average avalanche shapes of all durations.

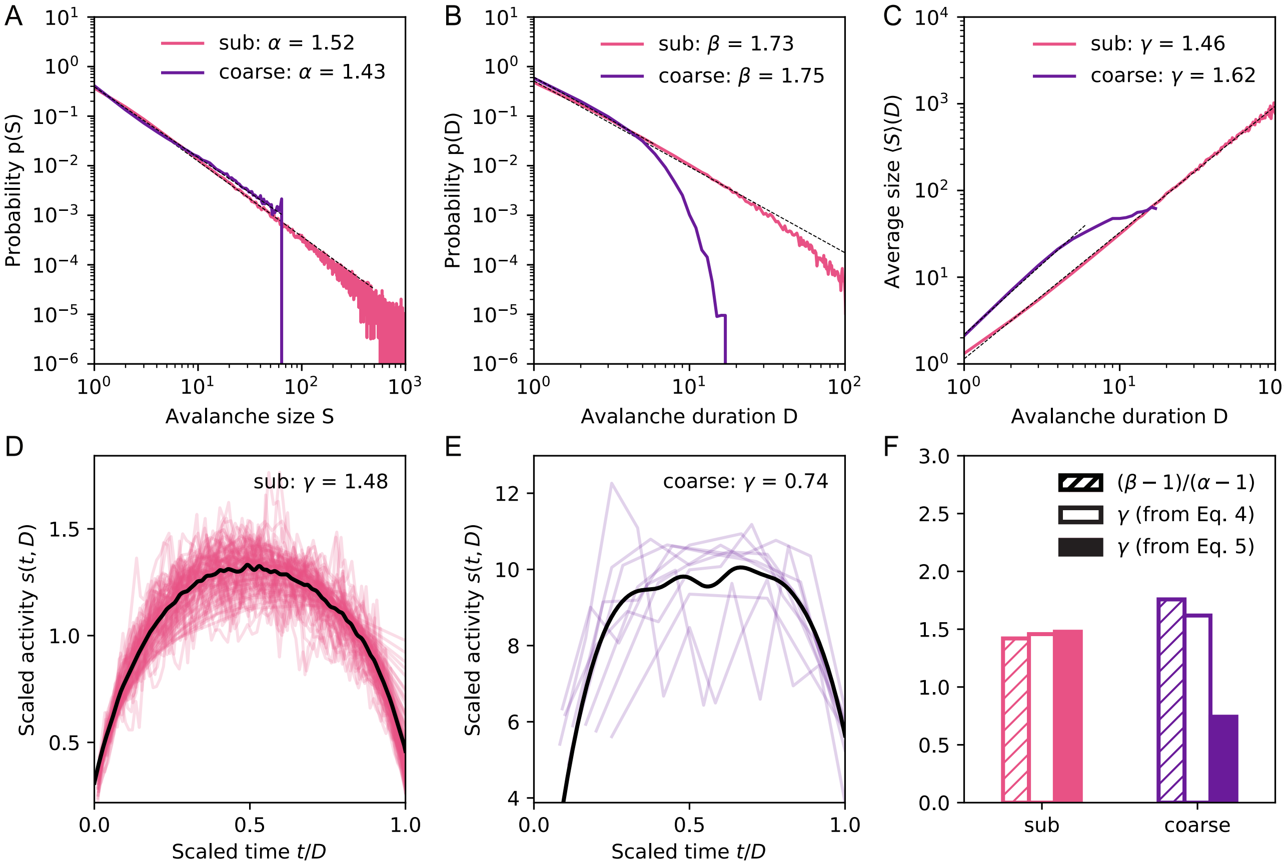

Figure 4.7: **Scaling laws of a system with critical dynamics under coarse- and sub-sampling. A–C:** Avalanche-size distribution $p(S) \sim S^{-\alpha}$, avalanche-duration distribution $p(D) \sim D^{-\beta}$, and average size for a given duration $\langle S\rangle(D) \sim D^{\gamma}$, respectively, for sub-sampled ("sub") and coarse-sampled ("coarse") simulations. Distributions under sub-sampling easily span more than one order of magnitude, while coarse-sampled distributions suffer from an early cut-off (which hinders power-law fits). **D, E:** Shape collapse of $s(t, D) \sim D^{\gamma-1}\mathscr{F}(t/D)$ for sub-sampled and coarse-sampled data, respectively. Under coarse-sampling, the early duration cut-off results in few unique shapes for the collapse (corresponding to unique D-values). **F:** Comparison of the critical exponents obtained independently from Eqs. (4.4)–(4.6). Exponents are consistent only under sub-sampling. **Parameters:** $d_E = 400\,\mu\text{m}$ and $\Delta t = 8\,\text{ms}$.

From Eqs. (4.4)–(4.6), we have three independent ways to determine the exponent γ. Consistency between the three is a further test of criticality. However, to the best of our knowledge, experimental evidence with the full set of scaling laws was only observed under sub-sampling: from spikes of in vitro recordings [134, 150].

The absence of scaling laws in coarse-sampled data can be explained by how coarse-sampling biases the average shape: the cut-off in $p(S)$ near the number of electrodes $S = N_\mathrm{E}$ implies that $\langle S\rangle(D) < N_\mathrm{E}$. From Eq. (4.4) we have $D < N_\mathrm{E}^{1/\gamma}$. If $\gamma > 1$ the cut-off in $p(S)$ causes a much earlier cut-off in both $p(D)$ and $\langle S\rangle(D)$.

Given that experiments typically have $N_\mathrm{E} \sim 10^2$ electrodes, $p(D)$ of a pure branching process (with $\gamma = 2$) would span a power-law for less than one order of magnitude. However, the typical standard to reliably fit a power-law is at least two orders of magnitude [27]. While this is problematic under coarse-sampling (Fig. 4.5), we have shown that the hard cut-off is not present under sub-sampling (Fig. 4.6).

Again comparing the two ways of sampling, we now apply the independent measurements of γ to our model with critical dynamics (Fig. 4.7). We find consistent exponents under sub-sampling.

In this case, although they differ from those expected for a pure branching process ($\gamma = 2$), the exponents we find are compatible with the experimental values of $\gamma_{exp} = 1.3 \pm 0.05$ reported in [134] and $1.3 \leq \gamma_{exp} \leq 1.5$ reported in [150].

Under coarse-sampling, however, the exponent obtained from the shape collapse ($\gamma \approx 0.74$) greatly differs from the other two ($\gamma \approx 1.74, \gamma \approx 1.62$), Fig. 4.7F. Moreover, the extremely short range available to fit $p(D)$ and $\langle S\rangle(D)$ with power-laws ($1 \leq D \leq 6$) makes the estimated exponents unreliable.

To conclude, the full set of critical exponents revealed criticality only under sub-sampling. Only in this case we observed both, a match between all the measurements of the exponent γ, and a power-law behavior extending over a range large enough to reliably fit them.

4.4 ALTERNATIVE MODELS

4.4.1 *Sampling bias remains under alternative topologies*

The network topology used in the main paper is local: on average, each neuron is connected to its nearest $K = 10^3$ neighbors. It is of interest to check if alternative topologies can impact the distinguishability of the underlying dynamic state under coarse-sampling.

For that, we select two additional topologies. The first ("Orlandi") mimics the growth process of a neuronal culture. In short, axons grow outward on a semi-flexible path of limited length and have a given probability to form a synapse when they intersect the (circular) dendritic tree of another neuron. Thereby, this topology is local without requiring distance-dependent synaptic weights (refer to [233] for more details). The second ("Random") implements a purely random connectivity, with each neuron being connected to $K = 10^3$ neurons. Note that this is an unrealistic setup as this topology is completely non-local.

We find that, under coarse-sampling, reverberating and critical dynamics remain indistinguishable with the alternative topologies (Fig. 4.8, left). Mean-

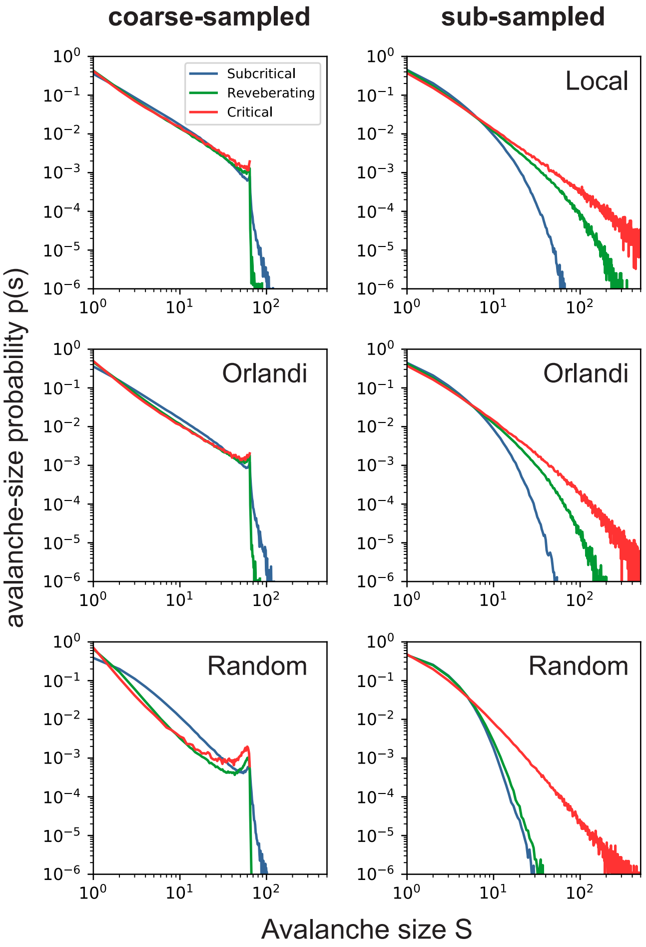

Figure 4.8: **Effect of alternative network topologies.** Avalanche-size probability $p(S)$ from coarse-sampled activity (**left**) and sub-sampled activity (**right**) for subcritical, reverberating and critical dynamics. **Top**: results for the topology used in the main paper (”Local”). **Middle**: results for a topology that mimics culture growth [233] (”Orlandi”). **Bottom**: results for a random topology. Under coarse-sampling, reverberating and critical dynamics are indistinguishable with all topologies. Parameters: $d_E = 400$ μm and $\Delta t = 8$ ms.

while, under sub-sampling, all dynamic states are clearly distinguishable for all topologies (Fig. 4.8, right).

4.4.2 *Influence of the electrode field-of-view*

In the main paper we considered that the contribution of a spiking neuron to the electrode signal decays with distance d as $\sim 1/d$. The precise way neuronal activity is recorded by extracellular electrodes depends on factors such as neuronal morphology and the level of correlation between synapses [203, 204]. Nevertheless, we can study the impact of a varying electrode field-of-view by changing

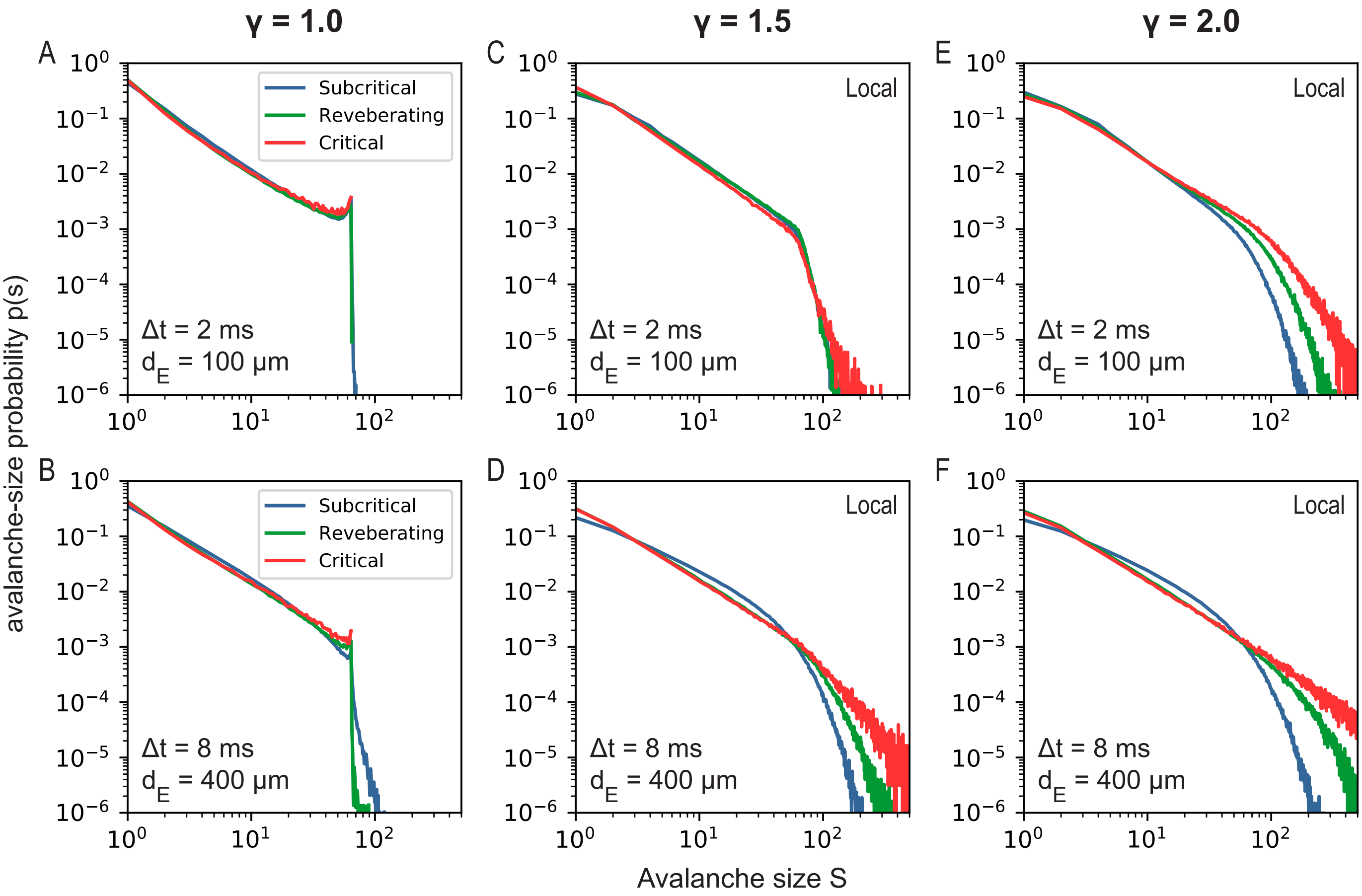

Figure 4.9: **Effect of changing the electrode contribution** $\sim 1/d^{-\gamma}$ **of a spiking neuron at distance** d**. A**: Avalanche-size probability $p(S)$ with $\gamma = 1.0$ for $\Delta t = 2\,\text{ms}$ and $d_{\text{E}} = 100\,\mu\text{m}$. **B**: Avalanche-size probability $p(S)$ with $\gamma = 1.0$ for $\Delta t = 8\,\text{ms}$ and $d_{\text{E}} = 400\,\mu\text{m}$. **C**: Same as A for $\gamma = 1.5$. **D**: Same as B for $\gamma = 1.5$. **E**: Same as A for $\gamma = 2.0$. **F**: Same as B for $\gamma = 2.0$. Increasing γ results in a smaller electrode field-of-view, and removes the cut-off for $S \sim N_{\text{E}}$.

the electrode contribution of a spike to $\sim 1/d^{\gamma}$ with $1 \leq \gamma \leq 2$. Note that $\gamma = 1$ corresponds to an electric monopole, while $\gamma = 2$ corresponds to an electric dipole — which has a considerably smaller spatial reach.

As γ increases, the relative contribution of the closest neurons to the electrode increases, and coarse-sampling becomes more similar to sub-sampling. The cut-off at $S \sim N_{\text{E}}$ vanishes for large γ, and the different dynamic states become distinguishable (Fig. 4.9D-F). For completeness, in Fig. 4.10 and Fig. 4.11 we show the effect of the varying electrode field-of-view for the alternative network topologies discussed previously ("Orlandi" and "Random"), with $d_{\text{E}} = 400\,\mu\text{m}$ and $d_{\text{E}} = 200\,\mu\text{m}$ respectively. In all cases, $\gamma \geq 1.5$ results in a vanishing of the cut-off in $p(S)$. Note, however, that this requires a sufficiently large d_{E}: for $d_{\text{E}} = 100\,\mu\text{m}$ and $\Delta t = 2\,\text{ms}$, an electrode field-of-view of $\gamma = 1.5$ displays the cut-off, and the dynamic states are not distinguishable (Fig. 4.9C).

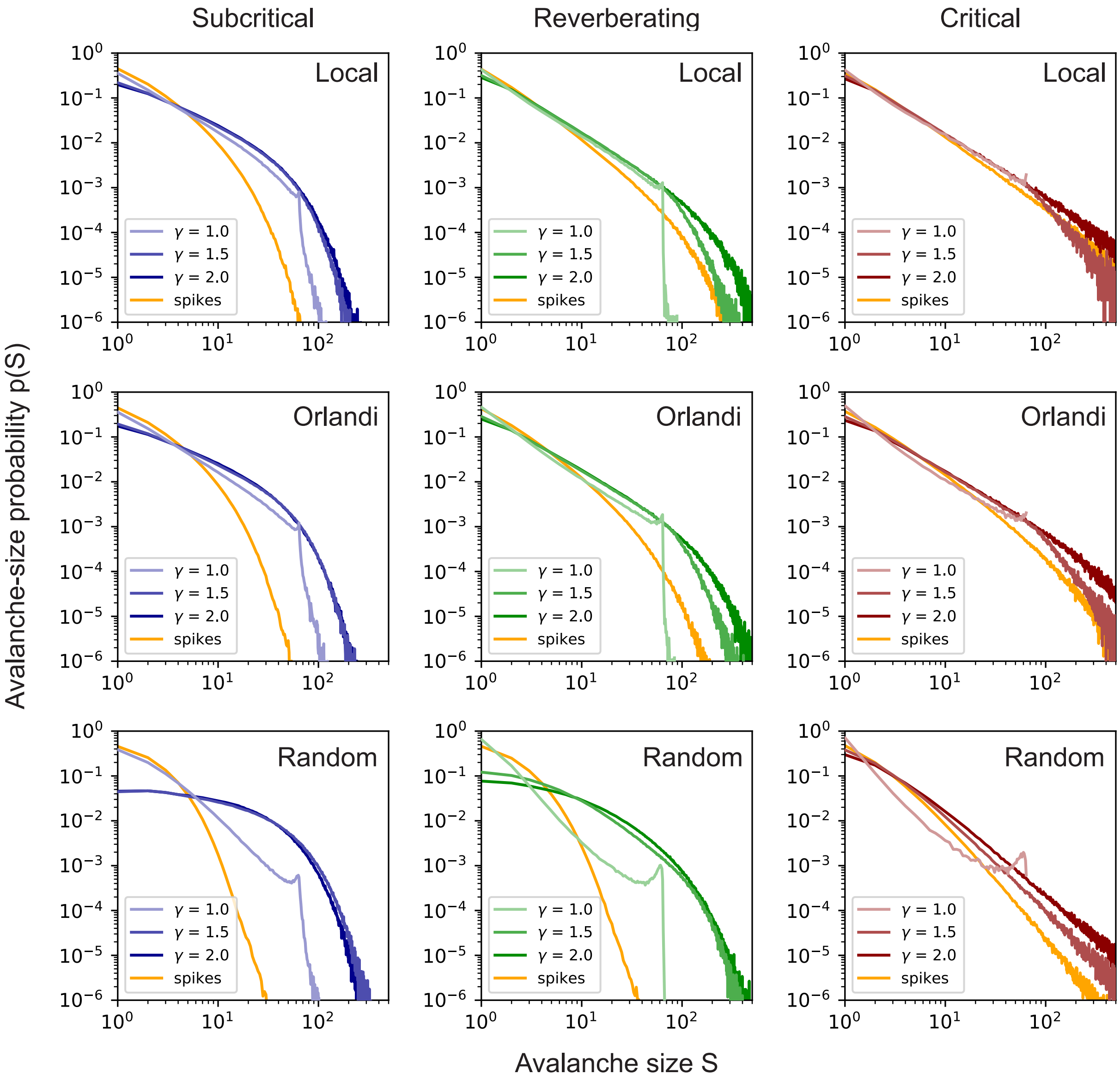

Figure 4.10: **Effect of changing the electrode contribution $\sim 1/d^{-\gamma}$ of a spiking neuron at distance d, for different network topologies and $d_\mathrm{E} = 200\,\mu\mathrm{m}$.** Dynamic states are Subcritical (**left**), Reverberating (**center**) and Critical (**right**). Topologies are Local (**top**), Orlandi (**middle**) and Random (**bottom**). Local corresponds to the topology used in the main paper, Orlandi corresponds to the model described in [233], and Random corresponds to a completely random topology. Increasing γ (decreasing electrode FOV) results in a loss of the cut-off for $p(S) \sim N_\mathrm{E}$ as the coarse-sampling becomes more spike-like. Bin-size for all distributions is $\Delta t = 4\,\mathrm{ms}$.

Thus, in order to determine criticality under coarse-sampling, the experimental set-up must combine i) a large d_E, ii) a narrow electrode field-of-view (large γ) and iii) systems with different dynamic states. This can potentially then be used to qualitatively compare the distance to criticality between the systems. Not only is this much more limited than what is possible with sub-sampled data [22, 177, 178], but the lack of the cut-off is not observed in experimental data of coarse-sampled recordings — which indicate that electrodes typically have a large field-of-view, and that our assumption of $\gamma = 1$ is adequate.

4.5 CONCLUSION

When inferring collective network dynamics from partially sampled systems, it is crucial to understand how the sampling biases the measured observables. Without this understanding, an elaborate analysis procedure — such as the one needed to study neuronal avalanches from coarse-sampled data — can result in a misclassification of the underlying dynamics.

We have shown that the analysis of neuronal avalanches based on (LFP-like) coarse-sampled data can produce indistinguishable results for systems with vastly different spatio-temporal signatures. These signatures derive from underlying dynamic states that, in this work, range from subcritical to critical — a range over which the intrinsic timescale undergoes a hundred-fold increase. And yet, the resulting avalanche-size distributions can be uninformative and ambiguous (Fig. 4.1).

The ambiguity of neuronal avalanches partially originates from spurious correlations. We have demonstrated the generation of spurious correlations from two sampling and processing mechanisms: measurement overlap (due to volume conduction) and temporal binning. Other studies found further mechanisms that can generate apparent power-law distributions by (purposely or accidentally) introducing correlations into the *observed* system. For instance, correlated input introduces temporal correlations already into the *underlying* system [7, 234]. Along with thresholding and low-pass frequency filtering — which add temporal correlations to the *observed* system [8, 9] — this creates a large space of variables that either depend on the system, sampling and processing, or a combination of both.

As our results focus on sampling and processing, we believe that the observed impact on avalanche-size distributions is general and model independent. We deliberately chose a simple model and confirmed that our results are robust to parameter changes: employing a more realistic topology causes no qualitative difference (Fig. 4.8).

With our results on sampling effects, we can revisit the previous literature on neuronal avalanches. In the model, we found that coarse-sampling clouds the differences between subcritical, reverberating, and critical dynamics: The avalanche distributions always resemble power laws (Fig. 4.1). Because of this ambiguity, the power-law distributions obtained ubiquitously from LFP, EEG, MEG and BOLD activity should be taken as evidence of neuronal activity with

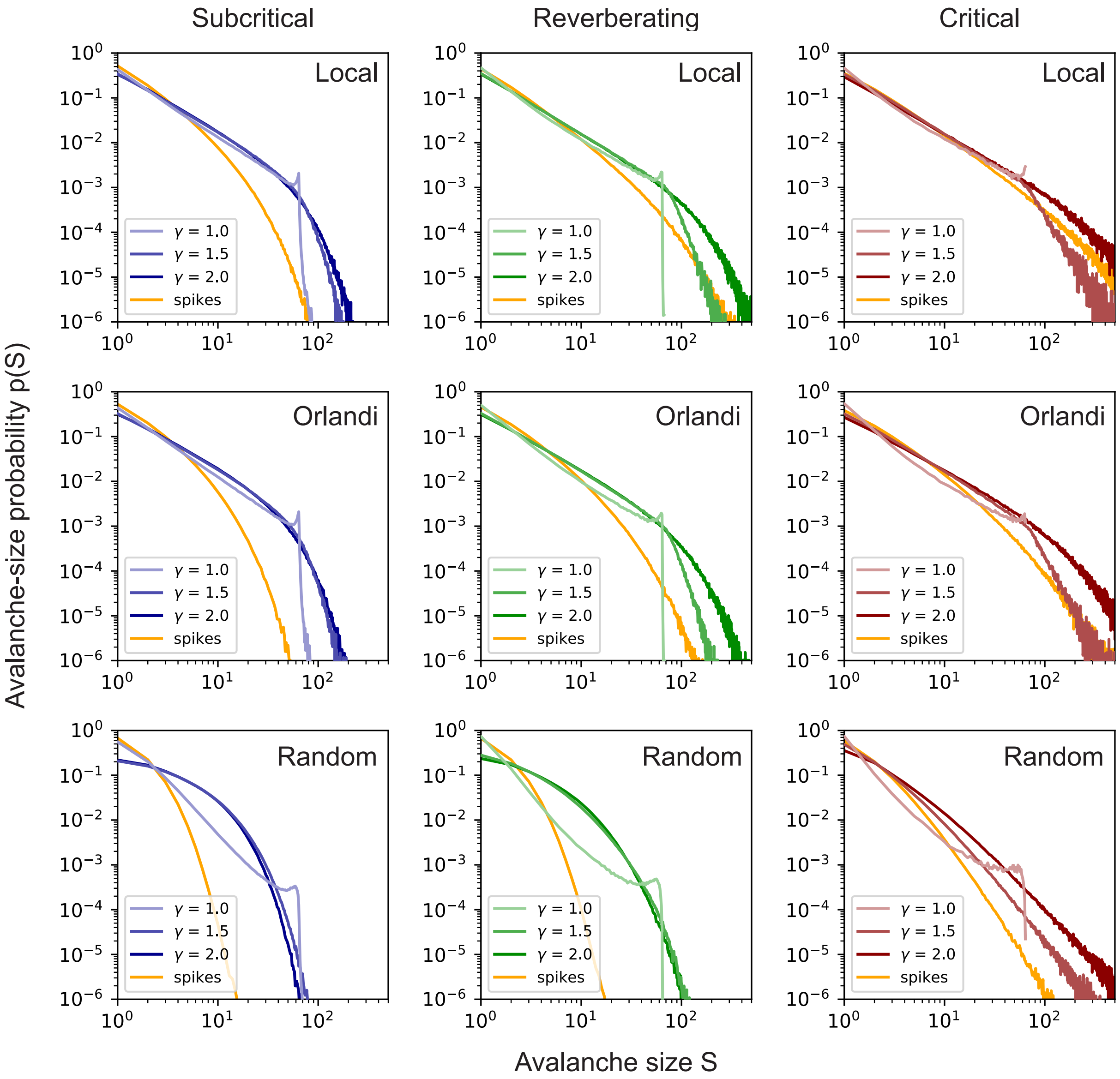

Figure 4.11: **Effect of changing the electrode contribution $\sim 1/d^{-\gamma}$ of a spiking neuron at distance d, for different network topologies and $d_E = 400\,\mu m$.** Dynamic states are Subcritical (**left**), Reverberating (**center**) and Critical (**right**). Topologies are Local (**top**), Orlandi (**middle**) and Random (**bottom**). Local corresponds to the topology used in the main paper, Orlandi corresponds to the model described in [233], and Random corresponds to a completely random topology. Increasing γ (decreasing electrode FOV) results in a loss of the cut-off for $p(S) \sim N_E$ as the coarse-sampling becomes more spike-like. Bin-size for all distributions is $\Delta t = 8\,\text{ms}$.

spatio-temporal correlations — but not necessarily of criticality proper; the coarse-sampling hinders such a precise classification.

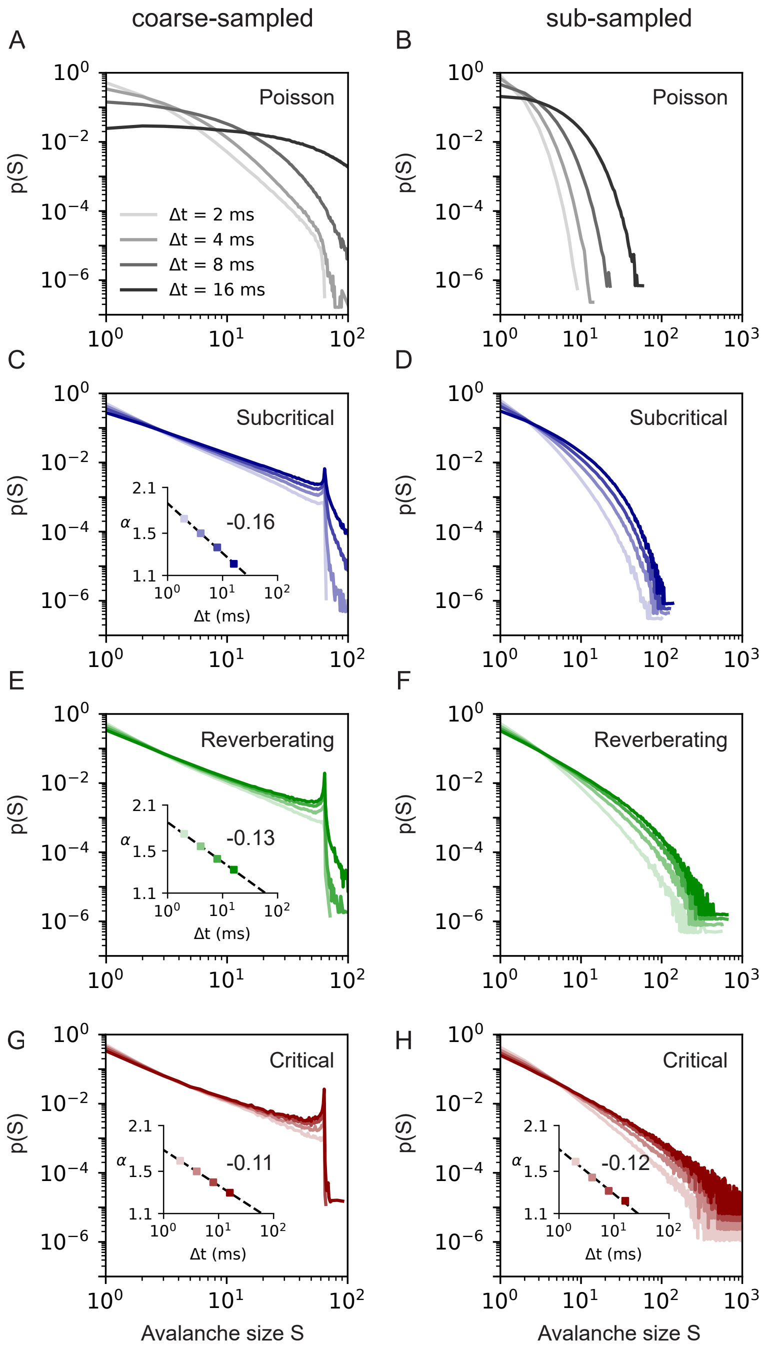

Figure 4.12: **Avalanche-size distributions** $p(S)$ **dependence on time-bin size** Δt **for** $d_\mathrm{E} = 200\,\mu\mathrm{m}$**.** Coarse-sampled (**left**) and sub-sampled (**right**) results from an array of 64 virtual electrodes with time bin sizes between $2\,\mathrm{ms} \leq \Delta t \leq 16\,\mathrm{ms}$. Dynamics states are Poisson (**A-B**), Subcritical (**C-D**), Reverberating (**E-F**) and Critical (**G-H**). Distributions are fitted to $p(S) \sim S^{-\alpha}$. **Insets:** Dependence of α on Δt, fitted as $\alpha \sim \Delta t^{-\beta}$. Fit values are shown in Table. 4.2.

In contrast, a more precise classification is possible under sub-sampling. If power-law distributions are observed from (sub-sampled) spiking activity, they do point to critical dynamics. For spiking activity, we even have mathematical tools to infer the precise underlying state in a sub-sampling-invariant manner that does not rely on avalanche distributions [177, 178]. Having said so, not all spike recordings point to critical dynamics: While in vitro recordings typically do produce power-law distributions [22, 101, 134, 174], recordings from awake animals do not [156, 179, 226, 235]. Together, these results suggest that in vitro systems self-organize towards criticality, whereas the cortex of awake animals (and humans) operates *near criticality* — in a slightly subcritical, reverberating *regime*.

The reverberating regime harnesses benefits associated with criticality, and it unifies both types of in vivo results: For experiments on awake animals, spike-based studies indicate subcritical dynamics. While coarse measures produce power laws that indicate criticality, with this study we showed that they cannot distinguish critical from subcritical dynamics. Consistent with both, a brain that operates in a regime — as opposed to a fixed dynamic state — can flexibly tune response properties. In particular, the reverberating regime covers a specific range of dynamics in the vicinity of the critical point, where small changes in effective synaptic strength cause major changes in response properties. Hence, the reverberating regime is an ideal baseline [178] from which brain areas or neural circuits can adapt to meet task demands [122, 137, 144, 146, 236–239].

In conclusion, our results methodically separate sampling effects from the underlying dynamic state. They overcome the discrepancy between the coarse-sampled and sub-sampled results of neuronal avalanches from awake animals. By offering a solution to a long-standing (critical) point of conflict, we hope to move beyond just describing a system as critical or not, and explore the richness of dynamic states around criticality.

5 DISCUSSION AND OUTLOOK

> *"But nature is always more subtle, more intricate, more elegant than what we are able to imagine."* - Carl Sagan

In this Thesis we examined the topic of criticality in the brain from both the theoretical (Physics) and experimental (Neuroscience) sides. Our focus was on rigor: to which extent can it be claimed that brain dynamics is approximated by a phase transition? How can sampling bias affect this claim?

5.1 CRITICAL CONSIDERATIONS

We first explored the theory of phase transitions, and the models that are used to represent neuronal activity in the context of criticality. We saw that criticality optimizes many properties in different models, such as correlations. This makes the concept enticing, as it means many algorithms (i.e. models) could implement computation with similar properties[1]. Thus, criticality in the brain goes beyond the specific (mostly branching) models used to study neuronal avalanches.

However, we also saw that the theory of phase transitions is far from finished, and that details do matter. In particular, we saw that i) seemingly small changes (such as adding a drive or external field) can drastically change the dynamics, and ii) topological details can change all aspects of the phase transition, from its existence (e.g. 1D vs 2D Ising model) to its critical point (e.g. value of the percolation threshold). In all but the simplest models analytical solutions are not known, and simulations must be handled with care[2].

Whether careful consideration is needed depends on the desired level of analysis. If only the most coarse properties are of interest (i.e. if there are power-laws), then simple arguments of universality may suffice. Other situations may demand knowledge of an explicit model — for instance, if we aim to manipulate the dynamics of the system.

In particular, if activity is sampled at a coarse level, and we assume it reflects (coarse grains) the underlying activity, then we must understand the model in intricate detail. This assumption is equivalent to assuming that the sampling effectively renormalizes the dynamics: as we have seen, not only is renormaliza-

---

[1] This ties to David Marr's levels of description [240], which argues that computation is divided in i) a computational task, ii) the algorithm used to solve the task and iii) the hardware (e.g. neuronal circuit) used to implement the algorithm.

[2] See e.g. coalescence in branching networks (Sec. 2.4.3).

tion only possible at criticality, but it requires very specific steps in order to be done correctly.

In the second part of this thesis we focused on experimental evidence of criticality in neuronal avalanches, and on the role of sampling effects. From that a clear picture emerges: evidence for criticality is still generally ambiguous, mostly due to experimental limitations. As phase transitions are collective phenomena, the observables used to ascertain criticality are affected by sampling bias. Strong evidence for criticality in systems displaying neuronal avalanches comes mainly in the form of a small number of papers [134, 148, 150] that measure the full set of scaling laws.

The more observables that are measured, the smaller the number of models that can generate all the required properties. This is particularly important in the case of neuronal avalanches, as many processes can generate the apparent power-laws used to identify critical phenomena. Yet we are unaware of any non-critical model capable of reproducing the full set of observables and scaling laws observed in the papers mentioned above, and they thus constitute important evidence that criticality may emerge in neuronal systems.

Our analyses on the effects of sampling in critical phenomena made clear that sampling can deeply impact assessment of neuronal activity, and must always[3] be explicitly taken into account. We've shown that sampling can both generate a wide range of spectral properties (Sec. 3.3) and generate power-laws for a wide range of subcritical states (Chapter 4). From this last result, we were able to unify the literature of neuronal avalanches with results from continuous (branching parameter) observables: they are all compatible with a baseline sightly subcritical, reverberating dynamics in vivo.

5.2 THE USEFULNESS OF SIMPLE MODELS

A common criticism of models such as the branching process is that they are too simple to be useful to understand the brain. Indeed, the branching process in particular does not include a number of mechanisms though to be key in real neurons. Namely, it has no inhibition, no membrane dynamics (which accounts for signal integration) and cannot generate oscillations. Yet, it reproduces a number of experimental features. Is that a good model?

Here, we apply the philosophy of "all models are wrong, some are useful". In particular, we measure the strength of a model based on how much we get out of it compared to how much was put into it. In other words, sophisticated models with large amounts of parameters should offer considerably more precise predictions than simple toy models, in order to be considered "better". More sophisticated models are not only more difficult to understand, but they are more

---

[3] In the case of collective properties.

prone to overfitting. As the saying goes: with four parameters you can fit an elephant, and with five you can make it wiggle its trunk[4].

In that, the branching process is a successful simple model: it is a analytically-treatable 1-parameter model that can describe and reproduce some involved properties of neuronal activity (correlation length and avalanche dynamics). The fact that it can reproduce those properties while lacking basic mechanisms suggests that perhaps these mechanisms are not very important for the properties studied, at the scale they were studied.

In the case of inhibition, this is perfectly consistent: inhibition is known to be mostly local, while we've seen (Table 2.1) that most evidence for criticality is on large scales. Thus, inhibition can be thought of as a field effect, homogeneously dampening activity and making the system subcritical. If that homogeneity is not present, such as when considering microscopic circuits, then models with explicit inhibition are better-suited.

With that in mind, it is not surprising that activity spreading in neuronal networks can be approximated to some extent with simple models. A better question is what kind of insight can be obtained from such models. We argue that the criticality hypothesis — and its phase transition models — is promising in that regard: it offers for instance the insight that many important observables of neuronal activity (e.g. correlation measures) can be created by simple and locally-controllable mechanisms, and thus open a window for the understanding of e.g. pharmacological manipulation of neuronal networks.

An important last point is that simple models are well-understood, and thus controllable. It is often said that model validation requires intervention: models must predict the result of experimental manipulation of the system. Being well-understood, models such as the branching parameter can offer clear predictions on the result of interventions.

5.3 WHERE DO WE GO FROM HERE?

Despite being a topic of research for more than 20 years, the extent to which brain dynamics can be approximated as a critical phase transition remains unknown. As we discussed above, solving this requires both analytical and experimental efforts. In this last part we comment on current and future developments that may help resolve this ambiguity.

On the analytical side, more realistic models are being developed that aim to correct the shortcomings of our phase transition models. For instance, models that explicitly add neuronal oscillations on top of a criticality framework [242, 243]. In particular, the CROS (CRitical OScillations) model does it by balancing inhibition and excitation, while still presenting a phase transition [211, 242]. In terms of sampling, efforts are underway to understand how to link neuronal

---

[4] This is a quote attributed to mathematician and pioneer computer scientist John von Neumann [241].

activity at different scales, and effectively understand how to perform coarse-graining of neuronal recordings [244–246].

The need for better analytical tools in Neuroscience is not confined to the study of criticality. In a paper called ″Could a Neuroscientist Understand a Microprocessor?″, Jonas & Kording [247] applied a number of often used analyses (such as correlation and causality measures) to a fully-simulated CPU from the 1970's. There was no experimental limitation, as every detail was known, and the CPU's deterministic dynamics could be followed with millisecond precision. Yet they showed that little insight was obtained from such analyses, and argued for the need of better tools.

On the experimental side, state-of-the-art and upcoming techniques have the potential to revolutionize the study of criticality in neuronal networks. In terms of electrophysiological recordings, Neuropixel probes [248] increase the number of recording sites to $\sim 10^3$ per shank, which can result in considerably less subsampling of spiking activity.

Perhaps more importantly, optical imaging techniques hold the promise of full sampling of neuronal activity [154, 249, 250]. This could completely bypass the current issues with sampling, and offer a definitive view to which extend brain activity is at a phase transition. This was already seen in Ponce-Alvarez *et al.* [148], in which zebrafish larvae was imaged with near-neuronal resolution. Due to the extremely large amount of recording sites (ROIs), avalanche analysis of the data yielded power-laws with orders-of-magnitude more statistics (longer distributions) than previous results.

One caveat is that those imaging techniques are based on calcium dynamics, which have slow (~ 1s) timescales. This results in a temporal resolution that is 2 orders of magnitude slower than spiking activity (~ 4 ms). Thus, for now it cannot be said results from imaging techniques present unequivocal evidence for criticality at the lowest levels of neuronal processing. Nevertheless, optical imaging remains the best bet for rigorous assessment of criticality in the brain.

Inevitably, as more detailed properties of neuronal activity are measured, and its large heterogeneity better understood, the concept of a critical phase transition becomes less useful. However we believe that, before it happens, criticality still has the potential to contribute plenty more to the understanding of the brain.

BIBLIOGRAPHY

[1] John M Beggs and Dietmar Plenz. “Neuronal avalanches in neocortical circuits.” In: *J. Neurosci.* 23.35 (Dec. 2003), pp. 11167–77. ISSN: 1529-2401.

[2] S Dunkelmann and G Radons. “Neural Networsk and Abelian Sandpile Models of Self-Organized Criticality.” In: *Proc. Int. Conf. Artif. Neural Networks*. Ed. by M. Marinaro and P. G. Morasso. Springer-Verlag, 1994, pp. 867–870.

[3] John M Beggs. “The criticality hypothesis: how local cortical networks might optimize information processing.” In: *Philos. Trans. R. Soc. A Math. Phys. Eng. Sci.* 366.1864 (2008), pp. 329–343. ISSN: 1364-503X, 1471-2962. DOI: `10.1098/rsta.2007.2092`.

[4] Dietmar Plenz and Ernst Niebur, eds. *Criticality in Neural Systems*. Vol. 9783527411. Weinheim, Germany: Wiley-VCH Verlag GmbH & Co. KGaA, Apr. 2014, pp. 1–566. ISBN: 9783527651009. DOI: `10.1002/9783527651009`.

[5] Miguel A. Muñoz. “Colloquium : Criticality and dynamical scaling in living systems.” In: *Rev. Mod. Phys.* 90.3 (July 2018), p. 031001. ISSN: 0034-6861. DOI: `10.1103/RevModPhys.90.031001`.

[6] Luca Cocchi et al. “Criticality in the brain: A synthesis of neurobiology, models and cognition.” In: *Prog. Neurobiol.* 158 (2017), pp. 132–152. ISSN: 18735118. DOI: `10.1016/j.pneurobio.2017.07.002`. arXiv: `1707.05952`.

[7] Viola Priesemann and Oren Shriki. “Can a time varying external drive give rise to apparent criticality in neural systems?” In: *PLOS Comput. Biol.* 14.5 (May 2018). Ed. by Francesco P. Battaglia, e1006081. ISSN: 1553-7358. DOI: `10.1371/journal.pcbi.1006081`.

[8] C. Bédard et al. “Does the 1/f Frequency Scaling of Brain Signals Reflect Self-Organized Critical States?” In: *Phys. Rev. Lett.* 97.11 (Sept. 2006), p. 118102. ISSN: 0031-9007. DOI: `10.1103/PhysRevLett.97.118102`.

[9] Jonathan Touboul and Alain Destexhe. “Can power-law scaling and neuronal avalanches arise from stochastic dynamics?” In: *PLoS One* 5.2 (2010). ISSN: 19326203. DOI: `10.1371/journal.pone.0008982`. arXiv: `0910.0805`.

[10] Suzana Herculano-Houzel. “The human brain in numbers: a linearly scaled-up primate brain.” In: *Front. Hum. Neurosci.* 3.NOV (2009), pp. 1–11. ISSN: 16625161. DOI: `10.3389/neuro.09.031.2009`.

[11] Hermann Cuntz et al. “One Rule to Grow Them All: A General Theory of Neuronal Branching and Its Practical Application.” In: *PLoS Comput. Biol.* 6.8 (Aug. 2010). Ed. by Abigail Morrison, e1000877. ISSN: 1553-7358. DOI: `10.1371/journal.pcbi.1000877`.

[12] H E Stanley. “Scaling, universality, and renormalization: Three pillars of modern critical phenomena.” In: *Rev Mod Phys* 71.2 (1999), S358–S366. ISSN: 0034-6861. DOI: 10.1103/RevModPhys.71.S358.

[13] James P. Sethna. *Statistical Mechanics: Entropy, Order Parameters, and Complexity*. 1st. New York: Oxford University Press, June 2006. ISBN: 9780198566779.

[14] Haye Hinrichsen. “Non-equilibrium critical phenomena and phase transitions into absorbing states.” In: *Adv. Phys.* 49.7 (2000), pp. 815–958. ISSN: 14606976. DOI: 10.1080/00018730050198152. arXiv: 0001070 [cond-mat].

[15] Jonas Dehning et al. “Inferring change points in the spread of COVID-19 reveals the effectiveness of interventions.” In: *Science (80-.)*. 369.6500 (July 2020), eabb9789. ISSN: 0036-8075. DOI: 10.1126/science.abb9789. arXiv: 2004.01105.

[16] Zhou Jiang et al. “MBene (MnB): a new type of 2D metallic ferromagnet with high Curie temperature.” In: *Nanoscale Horizons* 3.3 (2018), pp. 335–341. ISSN: 2055-6756. DOI: 10.1039/C7NH00197E.

[17] LEO P. KADANOFF et al. “Static Phenomena Near Critical Points: Theory and Experiment.” In: *Rev. Mod. Phys.* 39.2 (Apr. 1967), pp. 395–431. ISSN: 0034-6861. DOI: 10.1103/RevModPhys.39.395.

[18] M E Fisher. “The theory of equilibrium critical phenomena.” In: *Reports Prog. Phys.* 30.2 (July 1967), p. 306. ISSN: 00344885. DOI: 10.1088/0034-4885/30/2/306.

[19] Tatjana Tchumatchenko et al. “Spike correlations - What can they tell about synchrony?” In: *Front. Neurosci.* 5.MAY (2011), pp. 1–9. ISSN: 16624548. DOI: 10.3389/fnins.2011.00068.

[20] György Buzsáki and Kenji Mizuseki. “The log-dynamic brain: how skewed distributions affect network operations.” In: *Nat. Rev. Neurosci.* 15.4 (2014), pp. 264–78. ISSN: 1471-0048. DOI: 10.1038/nrn3687.

[21] Stefano Fusi et al. “Cascade models of synaptically stored memories.” In: *Neuron* 45.4 (2005), pp. 599–611. ISSN: 08966273. DOI: 10.1016/j.neuron.2005.02.001.

[22] A. Levina and V. Priesemann. “Subsampling scaling.” In: *Nat. Commun.* 8.1 (Aug. 2017), p. 15140. ISSN: 2041-1723. DOI: 10.1038/ncomms15140.

[23] Aaron Clauset et al. “Power-law distributions in empirical data.” In: (June 2007), p. 43. DOI: 10.1137/070710111. arXiv: 0706.1062.

[24] Anna Deluca and Álvaro Corral. “Fitting and goodness-of-fit test of non-truncated and truncated power-law distributions.” In: *Acta Geophys.* 61.6 (2013), pp. 1351–1394. ISSN: 1895-6572. DOI: 10.2478/s11600-013-0154-9. arXiv: arXiv:1212.5828v2.

[25] Rudolf Hanel et al. "Fitting power-laws in empirical data with estimators that work for all exponents." In: *PLoS One* 12.2 (2017), pp. 1–15. ISSN: 19326203. DOI: 10.1371/journal.pone.0170920. arXiv: 1609.05357.

[26] M. L. Goldstein et al. "Problems with fitting to the power-law distribution." In: *Eur. Phys. J. B* 41.2 (2004), pp. 255–258. ISSN: 14346028. DOI: 10.1140/epjb/e2004-00316-5. arXiv: 0402322 [cond-mat].

[27] Michael P.H. H. Stumpf and Mason A. Porter. "Critical Truths About Power Laws." In: *Science (80-.).* 335.6069 (2012), pp. 665–666. ISSN: 0036-8075. DOI: 10.1126/science.1216142.

[28] Osame Kinouchi and Mauro Copelli. "Optimal dynamical range of excitable networks at criticality." In: *Nat. Phys.* 2.5 (May 2006), pp. 348–351. ISSN: 1745-2473. DOI: 10.1038/nphys289.

[29] Johannes Zierenberg et al. "Tailored ensembles of neural networks optimize sensitivity to stimulus statistics." In: *Phys. Rev. Res.* 2.1 (Feb. 2020), p. 013115. ISSN: 2643-1564. DOI: 10.1103/PhysRevResearch.2.013115. arXiv: 1905.10401.

[30] Clayton Haldeman and John M Beggs. "Critical Branching Captures Activity in Living Neural Networks and Maximizes the Number of Metastable States." In: *Phys. Rev. Lett.* 94.5 (Feb. 2005), p. 058101. ISSN: 0031-9007. DOI: 10.1103/PhysRevLett.94.058101.

[31] Peter Krawitz and Ilya Shmulevich. "Basin entropy in Boolean network ensembles." In: *Phys. Rev. Lett.* 98.15 (2007), pp. 1–4. ISSN: 00319007. DOI: 10.1103/PhysRevLett.98.158701.

[32] Lucilla De Arcangelis and Hans J. Herrmann. "Learning as a phenomenon occurring in a critical state." In: *Proc. Natl. Acad. Sci. U. S. A.* 107.9 (2010), pp. 3977–3981. ISSN: 00278424. DOI: 10.1073/pnas.0912289107. arXiv: 1003.1200.

[33] Ariel Haimovici et al. "Brain Organization into Resting State Networks Emerges at Criticality on a Model of the Human Connectome." In: *Phys. Rev. Lett.* 110.17 (Apr. 2013), p. 178101. ISSN: 0031-9007. DOI: 10.1103/PhysRevLett.110.178101.

[34] G. Deco and V. K. Jirsa. "Ongoing Cortical Activity at Rest: Criticality, Multistability, and Ghost Attractors." In: *J. Neurosci.* 32.10 (2012), pp. 3366–3375. ISSN: 0270-6474. DOI: 10.1523/JNEUROSCI.2523-11.2012.

[35] A. M. Turing. "I.—COMPUTING MACHINERY AND INTELLIGENCE." In: *Mind* LIX.236 (Oct. 1950), pp. 433–460. ISSN: 1460-2113. DOI: 10.1093/mind/LIX.236.433.

[36] Chris G. Langton. "Computation at the edge of chaos: Phase transitions and emergent computation." In: *Phys. D Nonlinear Phenom.* 42.1-3 (June 1990), pp. 12–37. ISSN: 01672789. DOI: 10.1016/0167-2789(90)90064-V.

[37] Stephen Wolfram. "Universality and complexity in cellular automata." In: *Phys. D Nonlinear Phenom.* 10.1-2 (Jan. 1984), pp. 1–35. ISSN: 01672789. DOI: 10.1016/0167-2789(84)90245-8.

[38] James P. Crutchfield and Karl Young. "Inferring statistical complexity." In: *Phys. Rev. Lett.* 63.2 (July 1989), pp. 105–108. ISSN: 00319007. DOI: 10.1103/PhysRevLett.63.105.

[39] Nils Bertschinger and Thomas Natschläger. "Real-Time Computation at the Edge of Chaos in Recurrent Neural Networks." In: *Neural Comput.* 16.7 (July 2004), pp. 1413–1436. ISSN: 0899-7667. DOI: 10.1162/089976604323057443.

[40] T. Toyoizumi and L. F. Abbott. "Beyond the edge of chaos: Amplification and temporal integration by recurrent networks in the chaotic regime." In: *Phys. Rev. E - Stat. Nonlinear, Soft Matter Phys.* 84.5 (2011), pp. 1–8. ISSN: 15393755. DOI: 10.1103/PhysRevE.84.051908.

[41] Lars Büsing et al. "Connectivity, dynamics, and memory in reservoir computing with binary and analog neurons." In: *Neural Comput.* 22.5 (2010), pp. 1272–1311. ISSN: 08997667. DOI: 10.1162/neco.2009.01-09-947.

[42] Thomas M. Cover and Joy A. Thomas. *Elements of Information Theory*. 2005, pp. 1–748. ISBN: 9780471241959. DOI: 10.1002/047174882X. arXiv: ISBN0-471-06259-6.

[43] Michael Wibral et al. "Bits from Brains for Biologically Inspired Computing." In: *Front. Robot. AI* 2.March (Mar. 2015), pp. 1–25. ISSN: 2296-9144. DOI: 10.3389/frobt.2015.00005. arXiv: 1412.0291.

[44] Andre Ribeiro et al. "Mutual information in random Boolean models of regulatory networks." In: *Phys. Rev. E* 77.1 (Jan. 2008), p. 11901. ISSN: 1539-3755. DOI: 10.1103/PhysRevE.77.011901.

[45] Lionel Barnett et al. "Information flow in a kinetic ising model peaks in the disordered phase." In: *Phys. Rev. Lett.* 111.17 (2013), pp. 1–4. ISSN: 00319007. DOI: 10.1103/PhysRevLett.111.177203.

[46] Joschka Boedecker et al. "Information processing in echo state networks at the edge of chaos." In: *Theory Biosci.* 131.3 (Sept. 2012), pp. 205–213. ISSN: 14317613. DOI: 10.1007/s12064-011-0146-8.

[47] Joseph T. Lizier et al. "The information dynamics of phase transitions in random boolean networks." In: *Artif. Life XI Proc. 11th Int. Conf. Simul. Synth. Living Syst. ALIFE 2008* (2008), pp. 374–381.

[48] Melanie Mitchell et al. "Dynamics, Computation, and the "Edge of Chaos": A Re-Examination." In: May (June 1993). arXiv: 9306003 [adap-org].

[49] James P. Crutchfield. "Between order and chaos." In: *Nat. Phys.* 8.1 (Jan. 2012), pp. 17–24. ISSN: 17452473. DOI: 10.1038/nphys2190.

[50] Per Bak. *How Nature Works*. Springer New York, 1996. DOI: 10.1007/978-1-4757-5426-1.

[51] James P. Sethna et al. “Crackling noise.” In: *Nature* 410.6825 (Mar. 2001), pp. 242–250. ISSN: 0028-0836. DOI: 10.1038/35065675.

[52] R. K. Pathria and Paul D. Beale. *Statistical Mechanics*. 3rd. Academic Press, 2011. ISBN: 9780123821881. DOI: 10.1016/C2009-0-62310-2. arXiv: arXiv:1011.1669v3.

[53] Álvaro Corral et al. “Phase transition , scaling of moments , and order-parameter distributions in Brownian particles and branching processes with finite-size effects.” In: *Phys. Rev. E* 062156.97 (2018), pp. 1–11. DOI: 10.1103/PhysRevE.97.062156. arXiv: 1804.02300.

[54] Leo P. Kadanoff. “Scaling laws for ising models near Tc.” In: *Phys. Phys. Fiz.* 2.6 (June 1966), pp. 263–272. ISSN: 0554-128X. DOI: 10.1103/PhysicsPhysiqueFizika.2.263.

[55] M. E. J. Newman and G. T. Barkema. *Monte Carlo Methods in Statistical Physics*. 1st. New York: Oxford University Press, 1999, p. 490. ISBN: 9783540773405.

[56] Grégoire Lemoult et al. “Directed percolation phase transition to sustained turbulence in Couette flow.” In: *Nat. Phys.* 12.3 (Mar. 2016), pp. 254–258. ISSN: 1745-2473. DOI: 10.1038/nphys3675.

[57] Moritz Lang and Mikhail Shkolnikov. “Harmonic dynamics of the abelian sandpile.” In: *Proc. Natl. Acad. Sci.* 116.8 (Feb. 2019), pp. 2821–2830. ISSN: 0027-8424. DOI: 10.1073/pnas.1812015116.

[58] Haye Hinrichsen. “Non-equilibrium phase transitions.” In: *Phys. A Stat. Mech. its Appl.* 369.1 (Sept. 2006), pp. 1–28. ISSN: 03784371. DOI: 10.1016/j.physa.2006.04.007.

[59] David A. Levin et al. “Glauber dynamics for the mean-field Ising Model: Cut-off, critical power law, and metastability.” In: *Probab. Theory Relat. Fields* 146.1 (Oct. 2009), pp. 223–265. ISSN: 01788051. DOI: 10.1007/s00440-008-0189-z. arXiv: 0712.0790.

[60] Barry A. Cipra. “An Introduction to the Ising Model.” In: *Am. Math. Mon.* 94.10 (1987), p. 937. ISSN: 00029890. DOI: 10.2307/2322600.

[61] D. Stauffer. “Social applications of two-dimensional Ising models.” In: (2007), pp. 1–10. ISSN: 00029505. DOI: 10.1119/1.2779882. arXiv: 0706.3983.

[62] W.-X. Zhou and D. Sornette. “Self-organizing Ising model of financial markets.” In: *Eur. Phys. J. B* 55.2 (Jan. 2007), pp. 175–181. ISSN: 1434-6028. DOI: 10.1140/epjb/e2006-00391-6.

[63] Lars Onsager. “Crystal Statistics. I. A Two-Dimensional Model with an Order-Disorder Transition.” In: *Phys. Rev.* 65.3-4 (Feb. 1944), pp. 117–149. ISSN: 0031-899X. DOI: 10.1103/PhysRev.65.117.

[64] S. R. Broadbent and J. M. Hammersley. “Percolation processes.” In: *Math. Proc. Cambridge Philos. Soc.* 53.3 (July 1957), pp. 629–641. ISSN: 0305-0041. DOI: `10.1017/S0305004100032680`.

[65] Kazumasa A. Takeuchi et al. “Directed percolation criticality in turbulent liquid crystals.” In: *Phys. Rev. Lett.* 99.23 (2007), pp. 1–4. ISSN: 00319007. DOI: `10.1103/PhysRevLett.99.234503`.

[66] Dietrich Aharony et al. *Introduction to percolation theory*. 2nd ed. Taylor & Francis, Dec. 1992. ISBN: 0748400273,9780748400270. DOI: `10.1201/9781315274386`.

[67] Peter Grassberger and Yi-Cheng Zhang. ““Self-organized” formulation of standard percolation phenomena.” In: *Phys. A Stat. Mech. its Appl.* 224.1-2 (Feb. 1996), pp. 169–179. ISSN: 03784371. DOI: `10.1016/0378-4371(95)00321-5`.

[68] S.A. A Kauffman. “Metabolic stability and epigenesis in randomly constructed genetic nets.” In: *J. Theor. Biol.* 22.3 (Mar. 1969), pp. 437–467. ISSN: 00225193. DOI: `10.1016/0022-5193(69)90015-0`.

[69] J. Socolar and S. Kauffman. “Scaling in Ordered and Critical Random Boolean Networks.” In: *Phys. Rev. Lett.* 90.6 (Feb. 2003), p. 68702. ISSN: 0031-9007. DOI: `10.1103/PhysRevLett.90.068702`.

[70] Maria Davidich and Stefan Bornholdt. “The transition from differential equations to Boolean networks: a case study in simplifying a regulatory network model.” In: *J. Theor. Biol.* 255.3 (Dec. 2008), pp. 269–277. ISSN: 1095-8541. DOI: `10.1016/j.jtbi.2008.07.020`.

[71] Fangting Li et al. “The yeast cell-cycle network is robustly designed.” In: *Proc. Natl. Acad. Sci. U. S. A.* 101.14 (Apr. 2004), pp. 4781–4786. ISSN: 0027-8424. DOI: `10.1073/pnas.0305937101`.

[72] Jorge G. T. Zañudo et al. “Boolean Threshold Networks: Virtues and Limitations for Biological Modeling.” In: *Inf. Process. Biol. Syst.* Ed. by Samuli Niiranen and Andre Ribeiro. Vol. 11. Intelligent Systems Reference Library. Berlin, Heidelberg: Springer Berlin Heidelberg, 2011, pp. 113–135. ISBN: 978-3-642-19620-1. DOI: `10.1007/978-3-642-19621-8`.

[73] Thimo Rohlf and Stefan Bornholdt. “Criticality in random threshold networks: annealed approximation and beyond.” In: *Phys. A Stat. Mech. its Appl.* 310.1-2 (July 2002), pp. 245–259. ISSN: 03784371. DOI: `10.1016/S0378-4371(02)00798-7`.

[74] Agnes Szejka et al. “The phase diagram of random threshold networks.” In: *New J. Phys.* 10.6 (June 2008), p. 063009. ISSN: 1367-2630. DOI: `10.1088/1367-2630/10/6/063009`. arXiv: `0807.0429`.

[75] M Andrecut et al. “Maximal information transfer and behavior diversity in Random Threshold Networks.” In: *J. Comput. Biol.* 16.7 (July 2009), pp. 909–916. ISSN: 1557-8666. DOI: `10.1089/cmb.2009.0007`.

[76] Thimo Rohlf. "Critical line in random-threshold networks with inhomogeneous thresholds." In: *Phys. Rev. E* 78.6 (Dec. 2008), p. 66118. ISSN: 1539-3755. DOI: 10.1103/PhysRevE.78.066118. arXiv: 0707.3621.

[77] Joao Pinheiro Neto et al. "Inhibition as a determinant of activity and criticality in dynamical networks." In: *arXiv* 2.2 (2017), pp. 1–10. arXiv: 1712.08816v1.

[78] Daniel B. Larremore et al. "Inhibition Causes Ceaseless Dynamics in Networks of Excitable Nodes." In: *Phys. Rev. Lett.* 112.13 (Apr. 2014), p. 138103. ISSN: 0031-9007. DOI: 10.1103/PhysRevLett.112.138103. arXiv: 1307.7658.

[79] Rui-Sheng Wang and Réka Albert. "Effects of community structure on the dynamics of random threshold networks." In: *Phys. Rev. E* 87.1 (Jan. 2013), p. 012810. ISSN: 1539-3755. DOI: 10.1103/PhysRevE.87.012810.

[80] Rodrigo Poblanno-Balp and Carlos Gershenson. "Modular random Boolean networks." In: *Artif. Life* 17.4 (Jan. 2011), pp. 331–351. ISSN: 1064-5462. DOI: 10.1162/artl_a_00042. arXiv: 1101.1893.

[81] Per Bak et al. "Self-organized criticality: An explanation of the 1/f noise." In: *Phys. Rev. Lett.* 59.4 (July 1987), pp. 381–384. ISSN: 0031-9007. DOI: 10.1103/PhysRevLett.59.381.

[82] S. Lübeck and K. D. Usadel. "Numerical determination of the avalanche exponents of the Bak-Tang-Wiesenfeld model." In: *Phys. Rev. E - Stat. Physics, Plasmas, Fluids, Relat. Interdiscip. Top.* 55.4 (1997), pp. 4095–4099. ISSN: 1063651X. DOI: 10.1103/PhysRevE.55.4095. arXiv: 9702059 [cond-mat].

[83] Paolo Moretti and Miguel a Muñoz. "Griffiths phases and the stretching of criticality in brain networks." In: *Nat. Commun.* 4 (Jan. 2013), p. 2521. ISSN: 2041-1723. DOI: 10.1038/ncomms3521.

[84] Ronald Dickman et al. "Paths to self-organized criticality." In: *Brazilian J. Phys.* 30.1 (Mar. 2000), pp. 27–41. ISSN: 0103-9733. DOI: 10.1590/S0103-97332000000100004.

[85] Roman Frigg. "Self-organised criticality - What it is and what it isn't." In: *Stud. Hist. Philos. Sci. Part C Stud. Hist. Philos. Biol. Biomed. Sci.* 34 (2003), pp. 613–632. ISSN: 13698486. DOI: 10.1016/S0039-3681(03)00046-3.

[86] Nicholas W. Watkins et al. "25 Years of Self-organized Criticality: Concepts and Controversies." In: *Space Sci. Rev.* 198.1-4 (Jan. 2016), pp. 3–44. ISSN: 0038-6308. DOI: 10.1007/s11214-015-0155-x. arXiv: 1504.04991.

[87] Gunnar Pruessner. *Self-Organised Criticality*. Cambridge: Cambridge University Press, 2012, pp. 1–494. ISBN: 9780511977671. DOI: 10.1017/CBO9780511977671.

[88] S. S. Manna. "Two-state model of self-organized criticality." In: *J. Phys. A. Math. Gen.* 24.7 (Apr. 1991), pp. L363–L369. ISSN: 0305-4470. DOI: 10.1088/0305-4470/24/7/009.

[89] A. M. Alencar et al. “Self-organized percolation.” In: *Phys. Rev. E - Stat. Physics, Plasmas, Fluids, Relat. Interdiscip. Top.* 56.3 (1997), R2379–R2382. ISSN: 1063651X. DOI: `10.1103/PhysRevE.56.R2379`.

[90] Bartolo Luque et al. “Self-organized critical random Boolean networks.” In: *Phys. Rev. E* 63.5 (Apr. 2001), p. 51913. ISSN: 1063-651X. DOI: `10.1103/PhysRevE.63.051913`.

[91] Stefan Bornholdt and Torsten Röhl. “Self-organized critical neural networks.” In: *Phys. Rev. E* 67.6 (June 2003), p. 66118. ISSN: 1063-651X. DOI: `10.1103/PhysRevE.67.066118`.

[92] Matthias Rybarsch and Stefan Bornholdt. “Avalanches in self-organized critical neural networks: a minimal model for the neural SOC universality class.” In: *PLoS One* 9.4 (Jan. 2014), e93090. ISSN: 1932-6203. DOI: `10.1371/journal.pone.0093090`.

[93] Kim Christensen et al. “Unified scaling law for earthquakes.” In: *Proc. Natl. Acad. Sci.* 99.Supplement 1 (Feb. 2002), pp. 2509–2513. ISSN: 0027-8424. DOI: `10.1073/pnas.012581099`.

[94] H. E. Stanley et al. “Self-organized complexity in economics and finance.” In: *Proc. Natl. Acad. Sci.* 99.Supplement 1 (Feb. 2002), pp. 2561–2565. ISSN: 0027-8424. DOI: `10.1073/pnas.022582899`.

[95] Dante R. Chialvo. “Emergent complex neural dynamics.” In: *Nat. Phys.* 6.10 (Oct. 2010), pp. 744–750. ISSN: 1745-2473. DOI: `10.1038/nphys1803`. arXiv: `1010.2530`.

[96] a. Levina et al. “Dynamical synapses causing self-organized criticality in neural networks.” In: *Nat. Phys.* 3.12 (Nov. 2007), pp. 857–860. ISSN: 1745-2473. DOI: `10.1038/nphys758`.

[97] Janina Hesse and Thilo Gross. “Self-organized criticality as a fundamental property of neural systems.” In: *Front. Syst. Neurosci.* 8.September (Sept. 2014), pp. 1–14. ISSN: 1662-5137. DOI: `10.3389/fnsys.2014.00166`.

[98] Sheng-Jun Wang et al. “Sustained activity in hierarchical modular neural networks: self-organized criticality and oscillations.” In: *Front. Comput. Neurosci.* 5.June (Jan. 2011), p. 30. ISSN: 1662-5188. DOI: `10.3389/fncom.2011.00030`.

[99] Mikail Rubinov et al. “Neurobiologically realistic determinants of Self-Organized criticality in networks of spiking neurons.” In: *PLoS Comput. Biol.* 7.6 (2011). ISSN: 1553734X. DOI: `10.1371/journal.pcbi.1002038`.

[100] Jens Wilting et al. “Operating in a Reverberating Regime Enables Rapid Tuning of Network States to Task Requirements.” In: *Front. Syst. Neurosci.* 12.November (Nov. 2018). ISSN: 1662-5137. DOI: `10.3389/fnsys.2018.00055`.

[101] Christian Tetzlaff et al. “Self-Organized Criticality in Developing Neuronal Networks.” In: *PLoS Comput. Biol.* 6.12 (Dec. 2010). Ed. by Karl J. Friston, e1001013. ISSN: 1553-7358. DOI: `10.1371/journal.pcbi.1001013`.

[102] Thomas Vojta. “Rare region effects at classical, quantum and nonequilibrium phase transitions.” In: *J. Phys. A. Math. Gen.* 39.22 (June 2006), R143–R205. ISSN: 0305-4470. DOI: `10.1088/0305-4470/39/22/R01`. arXiv: `0602312 [cond-mat]`.

[103] Pablo Villegas et al. “Intrinsic noise and deviations from criticality in Boolean gene-regulatory networks.” In: *Sci. Rep.* 6.1 (Dec. 2016), p. 34743. ISSN: 2045-2322. DOI: `10.1038/srep34743`. arXiv: `1606.03235`.

[104] Adriana G. Moreira and Ronald Dickman. “Critical dynamics of the contact process with quenched disorder.” In: *Phys. Rev. E - Stat. Physics, Plasmas, Fluids, Relat. Interdiscip. Top.* 54.4 (Oct. 1996), R3090–R3093. ISSN: 1063651X. DOI: `10.1103/PhysRevE.54.R3090`. arXiv: `9604148 [cond-mat]`.

[105] A. J. Bray. “Nature of the Griffiths phase.” In: *Phys. Rev. Lett.* 59.5 (Aug. 1987), pp. 586–589. ISSN: 0031-9007. DOI: `10.1103/PhysRevLett.59.586`.

[106] Miguel a. Muñoz et al. “Griffiths Phases on Complex Networks.” In: *Phys. Rev. Lett.* 105.12 (Sept. 2010), p. 128701. ISSN: 0031-9007. DOI: `10.1103/PhysRevLett.105.128701`.

[107] Paolo Moretti and Miguel a Muñoz. “Griffiths phases and the stretching of criticality in brain networks.” In: *Nat. Commun.* 4 (Jan. 2013), p. 2521. ISSN: 2041-1723. DOI: `10.1038/ncomms3521`.

[108] Olaf Sporns. “The human connectome: A complex network.” In: *Ann. N. Y. Acad. Sci.* 1224 (2011), pp. 109–125. ISSN: 00778923. DOI: `10.1111/j.1749-6632.2010.05888.x`.

[109] Olaf Sporns. *Networks of the Brain*. Cambridge: MIT Press, 2010. ISBN: 978-0262014694.

[110] T. E. Harris. *The Theory of Branching Processes*. Berlin: Springer-Verlag, Feb. 1963, p. 119. ISBN: 978-3-642-51868-3.

[111] Johannes Zierenberg et al. “Description of spreading dynamics by microscopic network models and macroscopic branching processes can differ due to coalescence.” In: *Phys. Rev. E* 101.2 (Feb. 2020), p. 022301. ISSN: 2470-0045. DOI: `10.1103/PhysRevE.101.022301`. arXiv: `1905.10402`.

[112] C. R. Heathcote. “A Branching Process Allowing Immigration.” In: *J. R. Stat. Soc. Ser. B* 27.1 (1965), pp. 138–143. DOI: `10.1111/j.2517-6161.1965.tb00596.x`.

[113] Lasse Laurson et al. “The effect of thresholding on temporal avalanche statistics.” In: *J. Stat. Mech. Theory Exp.* 2009.01 (Jan. 2009), P01019. ISSN: 1742-5468. DOI: `10.1088/1742-5468/2009/01/P01019`.

[114] Francesc Font-Clos et al. “The perils of thresholding.” In: *New J. Phys.* 17.4 (Apr. 2015), p. 043066. ISSN: 1367-2630. DOI: 10.1088/1367-2630/17/4/043066.

[115] Pablo Villegas et al. “Time-series thresholding and the definition of avalanche size.” In: *Phys. Rev. E* 100.1 (July 2019), p. 012133. ISSN: 2470-0045. DOI: 10.1103/PhysRevE.100.012133.

[116] Serena di Santo et al. “Simple unified view of branching process statistics: Random walks in balanced logarithmic potentials.” In: *Phys. Rev. E* 95.3 (Mar. 2017), p. 032115. ISSN: 2470-0045. DOI: 10.1103/PhysRevE.95.032115. arXiv: 1612.07183.

[117] Heiko J. Luhmann et al. “Spontaneous neuronal activity in developing neocortical networks: From single cells to large-scale interactions.” In: *Front. Neural Circuits* 10.MAY (2016), pp. 1–14. ISSN: 16625110. DOI: 10.3389/fncir.2016.00040.

[118] Yang-Yu Liu et al. “Controllability of complex networks.” In: *Nature* 473.7346 (May 2011), pp. 167–173. ISSN: 1476-4687. DOI: 10.1038/nature10011.

[119] Adilson E. Motter. “Networkcontrology.” In: *Chaos* 25.9 (2015). ISSN: 10541500. DOI: 10.1063/1.4931570.

[120] M.E. E J. Newman. *Networks*. Oxford University Press, Mar. 2010, p. 720. ISBN: 9780199206650. DOI: 10.1093/acprof:oso/9780199206650.001.0001.

[121] P. J. Hellyer et al. “The Control of Global Brain Dynamics: Opposing Actions of Frontoparietal Control and Default Mode Networks on Attention.” In: *J. Neurosci.* 34.2 (2014), pp. 451–461. ISSN: 0270-6474. DOI: 10.1523/JNEUROSCI.1853-13.2014.

[122] Peter J. Hellyer et al. “Local inhibitory plasticity tunes macroscopic brain dynamics and allows the emergence of functional brain networks.” In: *Neuroimage* 124 (Jan. 2016), pp. 85–95. ISSN: 10538119. DOI: 10.1016/j.neuroimage.2015.08.069.

[123] Rui Li et al. “Controllability and observability of Boolean networks arising from biology.” In: *Chaos* 25.2 (2015), p. 23104. ISSN: 1054-1500. DOI: 10.1063/1.4907708.

[124] Jason Z Kim et al. “Role of graph architecture in controlling dynamical networks with applications to neural systems.” In: *Nat. Phys.* September (Sept. 2017). ISSN: 1745-2473. DOI: 10.1038/nphys4268.

[125] Gang Yan et al. “Network control principles predict neuron function in the Caenorhabditis elegans connectome.” In: *Nature* 550.7677 (Oct. 2017), pp. 519–523. ISSN: 0028-0836. DOI: 10.1038/nature24056.

[126] Lin Wu et al. *Controllability and Its Applications to Biological Networks*. Jan. 2019. DOI: 10.1007/s11390-019-1896-x.

[127] Richard Otter. “The Multiplicative Process.” In: *Ann. Math. Stat.* 20.2 (1949), pp. 206–224. ISSN: 0003-4851. DOI: `10.1214/aoms/1177730031`.

[128] Najja Marshall et al. “Analysis of Power Laws, Shape Collapses, and Neural Complexity: New Techniques and MATLAB Support via the NCC Toolbox.” In: *Front. Physiol.* 7.June (2016), pp. 1–18. ISSN: 1664-042X. DOI: `10.3389/fphys.2016.00250`.

[129] Stefanos Papanikolaou et al. “Universality beyond power laws and the average avalanche shape.” In: *Nat. Phys.* 7.4 (2011), pp. 316–320. ISSN: 17452481. DOI: `10.1038/nphys1884`.

[130] Andrea Baldassarri et al. “Average Shape of a Fluctuation: Universality in Excursions of Stochastic Processes.” In: *Phys. Rev. Lett.* 90.6 (2003), p. 060601. ISSN: 0031-9007. DOI: `10.1103/PhysRevLett.90.060601`. arXiv: `0301068 [cond-mat]`.

[131] E. D. Gireesh and D. Plenz. “Neuronal avalanches organize as nested theta- and beta/gamma-oscillations during development of cortical layer 2/3.” In: *Proc. Natl. Acad. Sci.* 105.21 (May 2008), pp. 7576–7581. ISSN: 0027-8424. DOI: `10.1073/pnas.0800537105`.

[132] Thomas Petermann et al. “Spontaneous cortical activity in awake monkeys composed of neuronal avalanches.” In: *Proc. Natl. Acad. Sci.* 106.37 (Sept. 2009), pp. 15921–15926. ISSN: 0027-8424. DOI: `10.1073/pnas.0904089106`.

[133] Andreas Klaus et al. “Statistical analyses support power law distributions found in neuronal avalanches.” In: *PLoS One* 6.5 (2011). ISSN: 19326203. DOI: `10.1371/journal.pone.0019779`.

[134] Nir Friedman et al. “Universal critical dynamics in high resolution neuronal avalanche data.” In: *Phys. Rev. Lett.* 108.20 (2012), pp. 1–5. ISSN: 00319007. DOI: `10.1103/PhysRevLett.108.208102`.

[135] C. Meisel et al. “Fading Signatures of Critical Brain Dynamics during Sustained Wakefulness in Humans.” In: *J. Neurosci.* 33.44 (2013), pp. 17363–17372. ISSN: 0270-6474. DOI: `10.1523/JNEUROSCI.1516-13.2013`.

[136] J. Matias Palva et al. “Neuronal long-range temporal correlations and avalanche dynamics are correlated with behavioral scaling laws.” In: *Proc. Natl. Acad. Sci.* 110.9 (Feb. 2013), pp. 3585–3590. ISSN: 0027-8424. DOI: `10.1073/pnas.1216855110`.

[137] Viola Priesemann et al. “Neuronal Avalanches Differ from Wakefulness to Deep Sleep – Evidence from Intracranial Depth Recordings in Humans.” In: *PLoS Comput. Biol.* 9.3 (Mar. 2013), e1002985. ISSN: 1553-7358. DOI: `10.1371/journal.pcbi.1002985`.

[138] O. Shriki et al. “Neuronal Avalanches in the Resting MEG of the Human Brain.” In: *J. Neurosci.* 33.16 (Apr. 2013), pp. 7079–7090. ISSN: 0270-6474. DOI: `10.1523/JNEUROSCI.4286-12.2013`.

[139] G. Scott et al. "Voltage Imaging of Waking Mouse Cortex Reveals Emergence of Critical Neuronal Dynamics." In: *J. Neurosci.* 34.50 (2014), pp. 16611–16620. ISSN: 0270-6474. DOI: `10.1523/JNEUROSCI.3474-14.2014`.

[140] O. Arviv et al. "Near-Critical Dynamics in Stimulus-Evoked Activity of the Human Brain and Its Relation to Spontaneous Resting-State Activity." In: *J. Neurosci.* 35.41 (Oct. 2015), pp. 13927–13942. ISSN: 0270-6474. DOI: `10.1523/JNEUROSCI.0477-15.2015`.

[141] Timothy Bellay et al. "Irregular spiking of pyramidal neurons organizes as scale-invariant neuronal avalanches in the awake state." In: *Elife* 4.JULY 2015 (2015), pp. 1–25. ISSN: 2050084X. DOI: `10.7554/eLife.07224`.

[142] E. D. Fagerholm et al. "Cascades and Cognitive State: Focused Attention Incurs Subcritical Dynamics." In: *J. Neurosci.* 35.11 (2015), pp. 4626–4634. ISSN: 0270-6474. DOI: `10.1523/JNEUROSCI.3694-14.2015`.

[143] Paolo Massobrio et al. "Self-organized criticality in cortical assemblies occurs in concurrent scale-free and small-world networks." In: *Sci. Rep.* 5.June (2015), pp. 1–16. ISSN: 20452322. DOI: `10.1038/srep10578`.

[144] Woodrow L. Shew et al. "Adaptation to sensory input tunes visual cortex to criticality." In: *Nat. Phys.* 11.8 (Aug. 2015), pp. 659–663. ISSN: 1745-2473. DOI: `10.1038/nphys3370`.

[145] Wesley P. Clawson et al. "Adaptation towards scale-free dynamics improves cortical stimulus discrimination at the cost of reduced detection." In: *PLOS Comput. Biol.* 13.5 (May 2017), e1005574. ISSN: 1553-7358. DOI: `10.1371/journal.pcbi.1005574`.

[146] Gerald Hahn et al. "Spontaneous cortical activity is transiently poised close to criticality." In: *PLOS Comput. Biol.* 13.5 (May 2017). Ed. by Claus C. Hilgetag, e1005543. ISSN: 1553-7358. DOI: `10.1371/journal.pcbi.1005543`.

[147] Mohammad Yaghoubi et al. "Neuronal avalanche dynamics indicates different universality classes in neuronal cultures." In: *Sci. Rep.* 8.1 (Dec. 2018), p. 3417. ISSN: 2045-2322. DOI: `10.1038/s41598-018-21730-1`.

[148] Adrián Ponce-Alvarez et al. "Whole-Brain Neuronal Activity Displays Crackling Noise Dynamics." In: *Neuron* 100.6 (Dec. 2018), 1446–1459.e6. ISSN: 08966273. DOI: `10.1016/j.neuron.2018.10.045`.

[149] H. Bocaccio et al. "The avalanche-like behaviour of large-scale haemodynamic activity from wakefulness to deep sleep." In: *J. R. Soc. Interface* 16.158 (2019). ISSN: 17425662. DOI: `10.1098/rsif.2019.0262`.

[150] Karlis Kanders et al. "Fingerprints of a second order critical line in developing neural networks." In: *Commun. Phys.* 3.1 (Dec. 2020), p. 13. ISSN: 2399-3650. DOI: `10.1038/s42005-019-0276-8`.

[151] György Buzsáki et al. "The origin of extracellular fields and currents — EEG, ECoG, LFP and spikes." In: *Nat. Rev. Neurosci.* 13.6 (June 2012), pp. 407–420. ISSN: 1471-003X. DOI: `10.1038/nrn3241`.

[152] Philipp J. Keller et al. "Fast, high-contrast imaging of animal development with scanned light sheet-based structured-illumination microscopy." In: *Nat. Methods* 7.8 (Aug. 2010), pp. 637–642. ISSN: 15487091. DOI: `10.1038/nmeth.1476`.

[153] Weijian Yang et al. "Simultaneous Multi-plane Imaging of Neural Circuits." In: *Neuron* 89.2 (Jan. 2016), p. 269. ISSN: 10974199. DOI: `10.1016/j.neuron.2015.12.012`.

[154] Masashi Kondo et al. "Two-Photon calcium imaging of the medial prefrontal cortex and hippocampus without cortical invasion." In: *Elife* 6 (Sept. 2017). ISSN: 2050084X. DOI: `10.7554/eLife.26839`.

[155] Shan Yu et al. "Scale-Invariant Neuronal Avalanche Dynamics and the Cut-Off in Size Distributions." In: *PLoS One* 9.6 (June 2014), e99761. ISSN: 1932-6203. DOI: `10.1371/journal.pone.0099761`.

[156] Tiago L. Ribeiro et al. "Spike avalanches exhibit universal dynamics across the sleep-wake cycle." In: *PLoS One* 5.11 (2010). ISSN: 19326203. DOI: `10.1371/journal.pone.0014129`. arXiv: `1101.2434`.

[157] Enzo Tagliazucchi et al. "Large-scale signatures of unconsciousness are consistent with a departure from critical dynamics." In: *J. R. Soc. Interface* 13.114 (Jan. 2016), p. 20151027. ISSN: 1742-5689. DOI: `10.1098/rsif.2015.1027`.

[158] Takahiro Ezaki et al. "Closer to critical resting-state neural dynamics in individuals with higher fluid intelligence." In: *Commun. Biol.* 3.1 (Dec. 2020), p. 52. ISSN: 2399-3642. DOI: `10.1038/s42003-020-0774-y`.

[159] Mark M. Churchland et al. "Stimulus onset quenches neural variability: A widespread cortical phenomenon." In: *Nat. Neurosci.* 13.3 (Mar. 2010), pp. 369–378. ISSN: 10976256. DOI: `10.1038/nn.2501`.

[160] Adrián Ponce-Alvarez et al. "Task-Driven Activity Reduces the Cortical Activity Space of the Brain: Experiment and Whole-Brain Modeling." In: *PLoS Comput. Biol.* 11.8 (Aug. 2015), e1004445. ISSN: 15537358. DOI: `10.1371/journal.pcbi.1004445`.

[161] Christian Meisel et al. "Failure of adaptive self-organized criticality during epileptic seizure attacks." In: *PLoS Comput. Biol.* 8.1 (2012). ISSN: 1553734X. DOI: `10.1371/journal.pcbi.1002312`. arXiv: `1105.4786`.

[162] Gregory A Worrell et al. "Evidence for self-organized criticality in human epileptic hippocampus." In: *Neuroreport* 13.16 (Nov. 2002), pp. 2017–2021. ISSN: 0959-4965. DOI: `10.1097/00001756-200211150-00005`.

[163] M. Breakspear et al. “A unifying explanation of primary generalized seizures through nonlinear brain modeling and bifurcation analysis.” In: *Cereb. Cortex* 16.9 (2006), pp. 1296–1313. ISSN: 10473211. DOI: `10.1093/cercor/bhj072`.

[164] Viktor K. Jirsa et al. “On the nature of seizure dynamics.” In: *Brain* 137.8 (2014), pp. 2210–2230. ISSN: 14602156. DOI: `10.1093/brain/awu133`.

[165] P. Suffczynski et al. “Dynamics of non-convulsive epileptic phenomena modeled by a bistable neuronal network.” In: *Neuroscience* 126.2 (2004), pp. 467–484. ISSN: 03064522. DOI: `10.1016/j.neuroscience.2004.03.014`.

[166] Orrin Devinsky et al. “Epilepsy.” In: *Nat. Rev. Dis. Prim.* 4.May (2018). ISSN: 2056676X. DOI: `10.1038/nrdp.2018.24`.

[167] Christian Meisel. “Antiepileptic drugs induce subcritical dynamics in human cortical networks.” In: *Proc. Natl. Acad. Sci.* 117.20 (May 2020), pp. 11118–11125. ISSN: 0027-8424. DOI: `10.1073/pnas.1911461117`. arXiv: `1904.13026`.

[168] Piotr Milanowski and Piotr Suffczynski. “Seizures Start without Common Signatures of Critical Transition.” In: *Int. J. Neural Syst.* 26.8 (2016), pp. 1–15. ISSN: 17936462. DOI: `10.1142/S0129065716500532`.

[169] Theresa Wilkat et al. “No evidence for critical slowing down prior to human epileptic seizures.” In: *Chaos* 29.9 (2019), pp. 2–7. ISSN: 10541500. DOI: `10.1063/1.5122759`. arXiv: `1908.08973`.

[170] Annika Hagemann et al. “No evidence that epilepsy impacts criticality in pre-seizure single-neuron activity of human cortex.” In: (2020), pp. 1–19. arXiv: `2004.10642`.

[171] Jiangbo Pu et al. “Developing neuronal networks: self-organized criticality predicts the future.” In: *Sci. Rep.* 3 (Jan. 2013), p. 1081. ISSN: 2045-2322. DOI: `10.1038/srep01081`.

[172] Felipe Yaroslav Kalle Kossio et al. “Growing Critical: Self-Organized Criticality in a Developing Neural System.” In: *Phys. Rev. Lett.* 121.5 (2018), p. 58301. ISSN: 10797114. DOI: `10.1103/PhysRevLett.121.058301`. arXiv: `1811.02861`.

[173] Johannes Zierenberg et al. “Homeostatic Plasticity and External Input Shape Neural Network Dynamics.” In: *Phys. Rev. X* 8.3 (2018), p. 31018. ISSN: 21603308. DOI: `10.1103/PhysRevX.8.031018`. arXiv: `1807.01479`.

[174] V. Pasquale et al. “Self-organization and neuronal avalanches in networks of dissociated cortical neurons.” In: *Neuroscience* 153.4 (June 2008), pp. 1354–1369. ISSN: 03064522. DOI: `10.1016/j.neuroscience.2008.03.050`.

[175] Emilia Biffi et al. "The influence of neuronal density and maturation on network activity of hippocampal cell cultures: A methodological study." In: *PLoS One* 8.12 (2013). ISSN: 19326203. DOI: 10.1371/journal.pone.0083899.

[176] M. Ivenshitz and M. Segal. "Neuronal Density Determines Network Connectivity and Spontaneous Activity in Cultured Hippocampus." In: *J. Neurophysiol.* 104.2 (2010), pp. 1052–1060. ISSN: 0022-3077. DOI: 10.1152/jn.00914.2009.

[177] Jens Wilting and Viola Priesemann. "Between Perfectly Critical and Fully Irregular: A Reverberating Model Captures and Predicts Cortical Spike Propagation." In: *Cereb. Cortex* 29.6 (June 2019), pp. 2759–2770. ISSN: 1047-3211. DOI: 10.1093/cercor/bhz049.

[178] Jens Wilting and Viola Priesemann. "Inferring collective dynamical states from widely unobserved systems." In: *Nat. Commun.* 9.1 (Aug. 2018), p. 2325. ISSN: 2041-1723. DOI: 10.1038/s41467-018-04725-4.

[179] V. Priesemann et al. "Spike avalanches in vivo suggest a driven, slightly subcritical brain state." In: *Front. Syst. Neurosci.* 8.June (2014), p. 108. ISSN: 16625137. DOI: 10.3389/fnsys.2014.00108.

[180] Adiel Statman et al. "Synaptic Size Dynamics as an Effectively Stochastic Process." In: *PLoS Comput. Biol.* 10.10 (2014). ISSN: 15537358. DOI: 10.1371/journal.pcbi.1003846.

[181] Jin-Feng Feng Wang et al. "A review of spatial sampling." In: *Spat. Stat.* 2.1 (Dec. 2012), pp. 1–14. ISSN: 22116753. DOI: 10.1016/j.spasta.2012.08.001.

[182] Sharon L. Lohr. *Sampling*. Vol. 42. 2. Chapman and Hall/CRC, Apr. 2019, p. 223. ISBN: 9780429296284. DOI: 10.1201/9780429296284.

[183] Albert-László Barabási and Réka Albert. "Emergence of Scaling in Random Networks." In: *Science (80-.).* 286.5439 (Oct. 1999), pp. 509–512. ISSN: 00368075. DOI: 10.1126/science.286.5439.509.

[184] Michael P H Stumpf et al. "Subnets of scale-free networks are not scale-free: sampling properties of networks." In: *Proc. Natl. Acad. Sci. U. S. A.* 102.12 (2005), pp. 4221–4. ISSN: 0027-8424. DOI: 10.1073/pnas.0501179102.

[185] Shy Shoham et al. "How silent is the brain: Is there a "dark matter" problem in neuroscience?" In: *J. Comp. Physiol. A Neuroethol. Sensory, Neural, Behav. Physiol.* 192.8 (2006), pp. 777–784. ISSN: 03407594. DOI: 10.1007/s00359-006-0117-6.

[186] Johannes Zierenberg et al. "Scaling properties of a parallel implementation of the multicanonical algorithm." In: *Comput. Phys. Commun.* 184.4 (2013), pp. 1155–1160. ISSN: 00104655. DOI: 10.1016/j.cpc.2012.12.006.

[187] Jonathan Gross et al. "Massively parallel multicanonical simulations." In: *Comput. Phys. Commun.* 224 (Mar. 2018), pp. 387–395. ISSN: 00104655. DOI: 10.1016/j.cpc.2017.10.018.

[188] Edoardo Milotti. "1/F Noise: a Pedagogical Review." In: *arXiv Prepr. physics/0204033* (Apr. 2002), p. 26. DOI: 10.1016/j.jep.2010.11.024. arXiv: 0204033 [physics].

[189] F. N. Hooge. "1/F Noise." In: *Phys. B+C* 83.1 (1976), pp. 14–23. ISSN: 03784363. DOI: 10.1016/0378-4363(76)90089-9.

[190] Toshimitsu Musha and Mitsuaki Yamamoto. "1/f fluctuations in biological systems." In: *Proc. 19th Annu. Int. Conf. IEEE Eng. Med. Biol. Soc. 'Magnificent Milestones Emerg. Oppor. Med. Eng. (Cat. No.97CH36136)*. Vol. 6. IEEE, 1997, pp. 2692–2697. ISBN: 0-7803-4262-3. DOI: 10.1109/IEMBS.1997.756890.

[191] Per Bak et al. "Unified Scaling Law for Earthquakes." In: *Phys. Rev. Lett.* 88.17 (Apr. 2002), p. 4. ISSN: 10797114. DOI: 10.1103/PhysRevLett.88.178501. arXiv: 0112342 [cond-mat].

[192] V Gontis and B Kaulakys. "Multiplicative point process as a model of trading activity." In: *Phys. A Stat. Mech. its Appl.* 343 (Nov. 2004), pp. 505–514. ISSN: 03784371. DOI: 10.1016/j.physa.2004.05.080.

[193] Masanori Kobayashi and Toshimitsu Musha. "1/f Fluctuation of Heartbeat Period." In: *IEEE Trans. Biomed. Eng.* BME-29.6 (June 1982), pp. 456–457. ISSN: 0018-9294. DOI: 10.1109/TBME.1982.324972.

[194] Matthew Pitkin et al. *Gravitational wave detection by Interferometry (Ground and Space)*. July 2011. DOI: 10.12942/lrr-2011-5. arXiv: 1102.3355.

[195] Ella Podvalny et al. "A unifying principle underlying the extracellular field potential spectral responses in the human cortex." In: *J. Neurophysiol.* 114.1 (2015), pp. 505–519. ISSN: 0022-3077. DOI: 10.1152/jn.00943.2014.

[196] Richard Gao et al. "Inferring synaptic excitation/inhibition balance from field potentials." In: *Neuroimage* 158.March (2017), pp. 70–78. ISSN: 10959572. DOI: 10.1016/j.neuroimage.2017.06.078. arXiv: /dx.doi.org/10.1101/081125 [http:].

[197] F. Lombardi et al. "Balance of excitation and inhibition determines 1/f power spectrum in neuronal networks." In: *Chaos* 27.4 (2017), pp. 1–18. ISSN: 10541500. DOI: 10.1063/1.4979043. arXiv: 1708.09042.

[198] K. Diba et al. "Intrinsic Noise in Cultured Hippocampal Neurons: Experiment and Modeling." In: *J. Neurosci.* 24.43 (Oct. 2004), pp. 9723–9733. ISSN: 0270-6474. DOI: 10.1523/JNEUROSCI.1721-04.2004.

[199] B. Voytek et al. "Age-Related Changes in 1/f Neural Electrophysiological Noise." In: *J. Neurosci.* 35.38 (2015), pp. 13257–13265. ISSN: 0270-6474. DOI: 10.1523/JNEUROSCI.2332-14.2015.

[200] Joshua Milstein et al. "Neuronal shot noise and Brownian 1/f2 behavior in the local field potential." In: *PLoS One* 4.2 (2009), e4338. ISSN: 1932-6203. DOI: `10.1371/journal.pone.0004338`. arXiv: `0807.2893`.

[201] Claude Bédard et al. "Modeling extracellular field potentials and the frequency-filtering properties of extracellular space." In: *Biophys. J.* 86.3 (2004), pp. 1829–1842. ISSN: 0006-3495. DOI: `10.1016/S0006-3495(04)74250-2`. arXiv: `0303057 [physics]`.

[202] S Gabriel et al. "The dielectric properties of biological tissues: \uppercase{II}. Measurements in the frequency range 10\uppercase{H}z to 20\uppercase{GH}z." In: *Phys. Med. Biol.* 41.11 (1996), pp. 2251–2269.

[203] Gaute T. Einevoll et al. "Modelling and analysis of local field potentials for studying the function of cortical circuits." In: *Nat. Rev. Neurosci.* 14.11 (Nov. 2013), pp. 770–785. ISSN: 1471-003X. DOI: `10.1038/nrn3599`.

[204] Henrik Linden et al. "Modeling the spatial reach of the LFP." In: *Neuron* 72.5 (2011), pp. 859–872. ISSN: 08966273. DOI: `10.1016/j.neuron.2011.11.006`.

[205] Nikos K. Logothetis et al. "In Vivo Measurement of Cortical Impedance Spectrum in Monkeys: Implications for Signal Propagation." In: *Neuron* 55.5 (2007), pp. 809–823. ISSN: 08966273. DOI: `10.1016/j.neuron.2007.07.027`.

[206] Claude Bédard and Alain Destexhe. "Macroscopic models of local field potentials and the apparent 1/f noise in brain activity." In: *Biophys. J.* 96.7 (2009), pp. 2589–2603. ISSN: 00063495. DOI: `10.1016/j.bpj.2008.12.3951`. arXiv: `arXiv:0808.3853v2`.

[207] Szymon Łęski et al. "Frequency Dependence of Signal Power and Spatial Reach of the Local Field Potential." In: *PLoS Comput. Biol.* 9.7 (July 2013), e1003137. ISSN: 1553-7358. DOI: `10.1371/journal.pcbi.1003137`. arXiv: `arXiv:1302.4559v1`.

[208] Alberto Mazzoni et al. "Computing the Local Field Potential (LFP) from Integrate-and-Fire Network Models." In: *PLoS Comput. Biol.* 11.12 (2015), pp. 1–38. ISSN: 15537358. DOI: `10.1371/journal.pcbi.1004584`.

[209] Oscar Herreras. "Local Field Potentials: Myths and Misunderstandings." In: *Front. Neural Circuits* 10.December (2016), pp. 1–16. ISSN: 1662-5110. DOI: `10.3389/fncir.2016.00101`.

[210] S.B. Lowen and M.C. Teich. "Power-law shot noise." In: *IEEE Trans. Inf. Theory* 36.6 (1990), pp. 1302–1318. ISSN: 00189448. DOI: `10.1109/18.59930`.

[211] Leonardo Dalla Porta and Mauro Copelli. "Modeling neuronal avalanches and long-range temporal correlations at the emergence of collective oscillations: Continuously varying exponents mimic M/EEG results." In: *PLOS Comput. Biol.* 15.4 (Apr. 2019). Ed. by Daniele Marinazzo, e1006924. ISSN: 1553-7358. DOI: `10.1371/journal.pcbi.1006924`.

[212] C . G. Bénar et al. "Differences in MEG and EEG power-law scaling explained by a coupling between spatial coherence and frequency: a simulation study." In: *J. Comput. Neurosci.* 47.1 (Aug. 2019), pp. 31–41. ISSN: 0929-5313. DOI: `10.1007/s10827-019-00721-9`.

[213] Alex H. Williams et al. "Unsupervised Discovery of Demixed, Low-Dimensional Neural Dynamics across Multiple Timescales through Tensor Component Analysis." In: *Neuron* 98.6 (June 2018), 1099–1115.e8. ISSN: 08966273. DOI: `10.1016/j.neuron.2018.05.015`.

[214] J. Wilting and V. Priesemann. "25 years of criticality in neuroscience — established results, open controversies, novel concepts." In: *Curr. Opin. Neurobiol.* 58 (Oct. 2019), pp. 105–111. ISSN: 09594388. DOI: `10.1016/j.conb.2019.08.002`. arXiv: `1903.05129`.

[215] F. P. Spitzner et al. "MR. Estimator, a toolbox to determine intrinsic timescales from subsampled spiking activity." In: (July 2020). arXiv: `2007.03367`.

[216] Kai J. Miller et al. "Power-law scaling in the brain surface electric potential." In: *PLoS Comput. Biol.* 5.12 (2009). ISSN: 1553734X. DOI: `10.1371/journal.pcbi.1000609`. arXiv: `0712.0846`.

[217] Kenji Mizuseki et al. "Multiple single unit recordings from different rat hippocampal and entorhinal regions while the animals were performing multiple behavioral tasks." In: *CRCNS org* (2013).

[218] Rishidev Chaudhuri et al. "Random Recurrent Networks Near Criticality Capture the Broadband Power Distribution of Human ECoG Dynamics." In: *Cereb. Cortex* 062349.October (2017), pp. 1–13. ISSN: 1047-3211. DOI: `10.1093/cercor/bhx233`.

[219] Biyu J. He et al. "The temporal structures and functional significance of scale-free brain activity." In: *Neuron* 66.3 (2010), pp. 353–369. ISSN: 08966273. DOI: `10.1016/j.neuron.2010.04.020`. arXiv: `NIHMS150003`.

[220] Nicholas M. Dotson et al. "A Large-Scale Semi-Chronic Microdrive Recording System for Non-Human Primates." In: *Neuron* 96.4 (2017), 769–782.e2. ISSN: 10974199. DOI: `10.1016/j.neuron.2017.09.050`.

[221] Elizabeth L. Johnson et al. "Spectral Imprints of Working Memory for Everyday Associations in the Frontoparietal Network." In: *Front. Syst. Neurosci.* 12.January (Jan. 2019), pp. 1–12. ISSN: 1662-5137. DOI: `10.3389/fnsys.2018.00065`.

[222] Kenji Mizuseki et al. "Neurosharing: large-scale data sets (spike, {LFP}) recorded from the hippocampal-entorhinal system in behaving rats." In: *F1000Research* (Apr. 2014). DOI: 10.12688/f1000research.3895.1.

[223] Joshua N. Milstein and Christof Koch. "Dynamic Moment Analysis of the Extracellular Electric Field of a Biologically Realistic Spiking Neuron." In: *Neural Comput.* 20.8 (Aug. 2008), pp. 2070–2084. ISSN: 0899-7667. DOI: 10.1162/neco.2008.06-07-537. arXiv: 0711.0409.

[224] Joao Pinheiro Neto et al. "A unified picture of neuronal avalanches arises from the understanding of sampling effects." In: (Oct. 2019), pp. 33–35. DOI: 10.1101/759613. arXiv: 1910.09984.

[225] Gašper Tkačik et al. "Thermodynamics and signatures of criticality in a network of neurons." In: *Proc. Natl. Acad. Sci.* 112.37 (Sept. 2015), pp. 11508–11513. ISSN: 0027-8424. DOI: 10.1073/pnas.1514188112.

[226] Nima Dehghani et al. "Avalanche Analysis from Multielectrode Ensemble Recordings in Cat, Monkey, and Human Cerebral Cortex during Wakefulness and Sleep." In: *Front. Physiol.* 3.August (2012), pp. 1–18. ISSN: 1664-042X. DOI: 10.3389/fphys.2012.00302.

[227] Enzo Tagliazucchi et al. "Criticality in Large-Scale Brain fMRI Dynamics Unveiled by a Novel Point Process Analysis." In: *Front. Physiol.* 3.February (2012), pp. 1–12. ISSN: 1664-042X. DOI: 10.3389/fphys.2012.00015.

[228] Tiago L. Ribeiro et al. "Undersampled critical branching processes on small-world and random networks fail to reproduce the statistics of spike avalanches." In: *PLoS One* 9.4 (2014). ISSN: 19326203. DOI: 10.1371/journal.pone.0094992.

[229] B. L. Sabatini and W. G. Regehr. "Timing of Synaptic Transmission." In: *Annu. Rev. Physiol.* 61.1 (2002), pp. 521–542. ISSN: 0066-4278. DOI: 10.1146/annurev.physiol.61.1.521.

[230] Jeff Alstott et al. "powerlaw: A Python Package for Analysis of Heavy-Tailed Distributions." In: *PLoS One* 9.1 (Jan. 2014). Ed. by Fabio Rapallo, e85777. ISSN: 1932-6203. DOI: 10.1371/journal.pone.0085777. arXiv: 1305.0215.

[231] Pauli Virtanen et al. "SciPy 1.0: fundamental algorithms for scientific computing in Python." In: *Nat. Methods* (2020). ISSN: 1548-7105. DOI: 10.1038/s41592-019-0686-2.

[232] Hans Karl Janssen and Uwe C. Täuber. "The field theory approach to percolation processes." In: *Ann. Phys. (N. Y).* 315.1 (2005), pp. 147–192. ISSN: 00034916. DOI: 10.1016/j.aop.2004.09.011. arXiv: 0409670 [cond-mat].

[233] Javier G. Orlandi et al. "Noise focusing and the emergence of coherent activity in neuronal cultures." In: *Nat. Phys.* 9.9 (Sept. 2013), pp. 582–590. ISSN: 1745-2473. DOI: 10.1038/nphys2686.

[234] Jonathan Touboul and Alain Destexhe. "Power-law statistics and universal scaling in the absence of criticality." In: *Phys. Rev. E* 95.1 (Jan. 2015), pp. 2–6. ISSN: 2470-0045. DOI: `10.1103/PhysRevE.95.012413`.

[235] Gerald Hahn et al. "Neuronal avalanches in spontaneous activity in vivo." In: *J. Neurophysiol.* 104.6 (Dec. 2010), pp. 3312–3322. ISSN: 0022-3077. DOI: `10.1152/jn.00953.2009`.

[236] M. D. Fox et al. "The human brain is intrinsically organized into dynamic, anticorrelated functional networks." In: *Proc. Natl. Acad. Sci.* 102.27 (July 2005), pp. 9673–9678. ISSN: 0027-8424. DOI: `10.1073/pnas.0504136102`.

[237] Jaana Simola et al. "Critical dynamics of endogenous fluctuations predict cognitive flexibility in the Go/NoGo task." In: *Sci. Rep.* 7.1 (Dec. 2017), p. 2909. ISSN: 2045-2322. DOI: `10.1038/s41598-017-02750-9`.

[238] Gustavo Deco et al. "Emerging concepts for the dynamical organization of resting-state activity in the brain." In: *Nat. Rev. Neurosci.* 12.1 (Jan. 2011), pp. 43–56. ISSN: 1471-003X. DOI: `10.1038/nrn2961`.

[239] Nergis Tomen et al. "Marginally subcritical dynamics explain enhanced stimulus discriminability under attention." In: *Front. Syst. Neurosci.* 8.August (2014), pp. 1–15. ISSN: 1662-5137. DOI: `10.3389/fnsys.2014.00151`.

[240] D. Marr. "Vision: a computational investigation into the human representation and processing of visual information." In: *Vis. a Comput. Investig. into Hum. Represent. Process. Vis. information.* (1982). ISSN: 00222496. DOI: `10.1016/0022-2496(83)90030-5`.

[241] Freeman Dyson. "A meeting with Enrico Fermi." In: *Nature* 427.6972 (Jan. 2004), pp. 297–297. ISSN: 0028-0836. DOI: `10.1038/427297a`.

[242] S.-S. Poil et al. *Critical-State Dynamics of Avalanches and Oscillations Jointly Emerge from Balanced Excitation/Inhibition in Neuronal Networks*. 2012. DOI: `10.1523/JNEUROSCI.5990-11.2012`.

[243] Johannes Pausch et al. "Time-dependent branching processes: a model of oscillating neuronal avalanches." In: *Sci. Rep.* 10.1 (Dec. 2020), p. 13678. ISSN: 2045-2322. DOI: `10.1038/s41598-020-69705-5`.

[244] Vidit Agrawal et al. "Scale-Change Symmetry in the Rules Governing Neural Systems." In: *iScience* 12 (2019), pp. 121–131. ISSN: 25890042. DOI: `10.1016/j.isci.2019.01.009`.

[245] Leenoy Meshulam et al. "Coarse Graining, Fixed Points, and Scaling in a Large Population of Neurons." In: *Phys. Rev. Lett.* 123.17 (Oct. 2019), p. 178103. ISSN: 0031-9007. DOI: `10.1103/PhysRevLett.123.178103`. arXiv: `1812.11904`.

[246] Giorgio Nicoletti et al. "Scaling and criticality in a phenomenological renormalization group." In: *Phys. Rev. Res.* 2.2 (May 2020), p. 023144. ISSN: 2643-1564. DOI: `10.1103/PhysRevResearch.2.023144`.

[247] Eric Jonas and Konrad Paul Kording. "Could a neuroscientist understand a microprocessor ?" In: XXI.1 (2016), pp. 1–5. DOI: `10.1101/055624`.

[248] Nicholas A. Steinmetz et al. *Challenges and opportunities for large-scale electrophysiology with Neuropixels probes*. June 2018. DOI: `10.1016/j.conb.2018.01.009`.

[249] Hod Dana et al. "Sensitive red protein calcium indicators for imaging neural activity." In: *Elife* 5.MARCH2016 (Mar. 2016). ISSN: 2050-084X. DOI: `10.7554/eLife.12727`.

[250] Philipp J. Keller and Misha B. Ahrens. *Visualizing whole-brain activity and development at the single-cell level using light-sheet microscopy*. Feb. 2015. DOI: `10.1016/j.neuron.2014.12.039`.

INDEX